

Study of nitrogen doped reduced graphene oxide (rGO) for its potential application as super-capacitor and photo-detector.

A thesis submitted towards partial fulfilment of the requirements for the degree of:

Master of Technology in Nano Science and Technology

Submitted by:

Manas Thakur

Roll no. : M4NST22022

Registration no. : 154591 of 2021-22

Under the guidance of

Prof.(Dr.) Sourav Sarkar

School of Materials Science and Nanotechnology

Jadavpur University

Kolkata - 700032

Course Affiliated to:

**Faculty of Interdisciplinary Studies,
Law and Management**

Jadavpur University

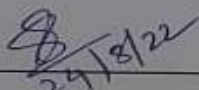
Kolkata, India

2022

M.Tech (Nano Science and Technology)
Course affiliated to:
Faculty of Interdisciplinary Studies,
Law and Management
Jadavpur University
Kolkata, India

CERTIFICATE OF RECOMMENDATION

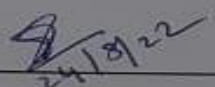
This is in order to certify that the thesis entitled "Study of nitrogen doped reduced graphene oxide (rGO) for its potential application as super-capacitor and photo-detector." is a legitimate work done by Manas Thakur under our supervision and guidance for the purposes of fulfilling the requirement for the degree of Master of Technology in Nano Science and Nanotechnology in the School of Materials Science and Nanotechnology from the academic session 2020-2022.


24/8/22

Thesis advisor

Dr Sourav Sarkar
School of Materials Science and Nanotechnology
Jadavpur University,
Kolkata-700 032

Dr. Sourav Sarkar
Director
Associate Professor
School of Materials Science & Nanotechnology
Jadavpur University
Kolkata - 700032


24/8/22

Director

School of Materials Science and Nanotechnology
Jadavpur University
Kolkata-700 032

Dr. Sourav Sarkar
Director
Associate Professor
School of Materials Science & Nanotechnology
Jadavpur University
Kolkata - 700032


24.08.2022

Dean

Faculty Council of Interdisciplinary Studies, Law and Management
Jadavpur University,
Kolkata-700 032

Dean
Faculty of Interdisciplinary Studies
Law & Management
Jadavpur University, Kolkata-700032

M.Tech (Nano Science and Technology)
Course affiliated to:
Faculty of Interdisciplinary Studies,
Law and Management
Jadavpur University
Kolkata, India

CERTIFICATE OF APPROVAL

I hereby endorse the foregoing thesis as an engineering study, conducted and presented in a manner satisfactory enough to justify its acceptance as an engineering study, in order to obtain the degree for which it has been submitted. This approval does not endorse or approve any statement made, opinion expressed or conclusion drawn therein, but merely approves the thesis for the purpose for which it has been submitted.

**Committee of the final examination
for evaluation of the Thesis**

** Only in case the thesis is approved.

DECLARATION OF ORIGINALITY AND COMPLIANCE OF ACADEMIC ETHICS

I hereby declare that this thesis contains a literature survey and original research work by the undersigned candidate for the Master of Technology (Nano Science and Technology) program during the academic year 2020-2022.

The information in this document has been gathered and presented according to academic standards and ethical conduct.

I also declare that I have cited and referred to all materials and results that are not original to this work as required by these rules and conduct.

Name: MANAS THAKUR

Roll Number: M4NST22022

Registration Number: 154591 of 2021-22

Thesis Title: Study of nitrogen doped reduced graphene oxide (rGO) for its potential application as super-capacitor and photo-detector.

SIGNATURE

DATE

**Dedicated to my
parents**

ACKNOWLEDGEMENT

I am grateful to **Dr. Sourav Sarkar** my adviser, for his consistent encouragement, passion, and wide knowledge throughout my Master's studies and research. He was there for me every step of the way as I worked on my thesis. Your informative comments inspired my entire research project, and I am grateful. In addition, I'd want to express my gratitude to **Prof. Kalyan Kumar Chattopadhyay** and the Thin Film and Nano Science Lab, as well as the Nanoscience and Nanotechnology Lab, for establishing a friendly work environment for me.

Mr. Dipayan Roy, my mentor, deserves my gratitude for his direction and assistance with all of my project-related issues, as well as for cooperating with me to make it what it is now.

I gratefully thank **Prof. Kalayan Kumar Chattopadhyaya, Dr. Sourav Sarkar, Dr. Mahua Ghosh, and Dr. Chandan Kumar Ghosh** for their assistance, support, recommendations, and guidance. They offered a helpful and constructive learning environment, and their excitement inspired me to pursue the research topic with zeal.

I want to thank Diptangshu Modak, who assisted in the schematic sketching of this thesis, and Soumalya Bhowmick, PhD, IIT Guwahati, for their support and assistance.

Sk Najes Riaz, Ankita Chandra, Dimitra Das, Antika Das, Karamjyoti Panigrahi, Nabanita Sen, Suvankar Mondal, Ratna Sarkar, Bikram Kumar Das, Anibrata Banerjee, Suvankar Poddar, Suvra Pal, and Arnab Das, my seniors, deserve my heartfelt gratitude for making my project such a memorable experience. I truly thank Tanay Toppo, Md Imran Ansari, Dipabala Sarkar and my classmates for their assistance and support throughout this course. I could not have completed my project without their assistance. In light of their tremendous aid, my words of gratitude are insufficient.

Finally, I want to express my heartfelt gratitude to my parents and all of my supporters for their love and support.

Abstract

In this study, hydrothermal synthesis was used to produce porous nitrogen doped reduced graphene oxide (N-rGO). Prior to that, the modified Hummer's method was used to prepare graphene oxide (GO). Using an XRD instrument, the crystallinity and phase have been confirmed. FESEM and HRTEM pictures have been used for morphological examination, which supports decreased graphene oxide's flake-like structure and porous nature (rGO). The degree of nitrogen doping and reduction of other functional groups of rGO have been validated by XPS using the results of the spectrometric study. Raman spectroscopy, on the other hand, evaluates the material's vibrational frequency and confirms the reduction procedure. Comparisons of the band gaps between silicon nanowire and rGO have been made from UV-vis, which ultimately aids in determining the optimum sample to create a photodetector. It is proven by the cyclic voltametric analysis that NORG-24h has the best gravimetric capacitance and areal capacitance at 5 mV/s, measuring 1113.4 F g⁻¹ and 309.27 mF cm⁻², respectively. A coplanar interdigitate supercapacitor device with gravimetric and areal capacitance of 302.44 F g⁻¹ and 79.84 mF cm⁻², respectively, at a scan rate of 50 mV/s has been created with an eye toward industrial application. N-rGO has emerged from this research as a promising component for use as a photodetector material. Under IR conditions, it demonstrated reliable ON-OFF switching characteristics in reverse bias. Maximum stability and less noise is attained at lower reverse bias such as -0.05V and -0.25V. This material exhibits current even at 0V which is still under investigation. In summary, it can be clearly and significantly stated that nitrogen-doped reduced graphene oxide is an excellent nanomaterial that can be used in supercapacitor applications to achieve promising energy density, power density, and long cycles as well as being able to be used as an IR photodetector, which implies as IR sensors as well.

Table of Contents

1. Chapter 1: Introduction

- Introduction
- Reduced Graphene Oxide
- Properties of Reduced Graphene Oxide
- Supercapacitor
 - Classification of Supercapacitor
 - Electrochemical double-layer capacitors (EDLC)
 - Pseudo-capacitors
 - Hybrid-capacitor
 - Application of Supercapacitor
 - Automobile
 - Mobile devices
 - Micro-Grid
- Nanowires
 - Semiconducting nanowires
 - Properties of nanowires
 - Application of nanowires
 - Photodetector
 - Application of Photodetector

2. Chapter 2: Instrumentation

- Characterization techniques
 - Morphological Characterizations
 - Scanning Electron Microscope (SEM)
 - ❖ Sample preparation of FESEM
 - ❖ Components of FESEM
 - Transmission Electron Microscope (TEM)
 - ❖ Components of HRTEM
 - Phase or Crystallographic characterization
 - X-Ray Diffraction (XRD)
 - Spectroscopic Characterization
 - UV-vis near infrared spectroscopy
 - Fourier Transform Infrared Spectroscopy (FT-IR)
 - Raman Spectroscopy
 - X-Ray Photoelectron Spectroscopy (XPS)
 - Cyclic Voltammetry (CV)
 - I-V Characterization

3. Chapter 3: Different Synthesis Techniques

- GO Synthesis Techniques
 - Staudenmaier's (ST) method
 - Hummer's method
 - Hydrothermal process
 - Advantage of Hydrothermal process
 - Disadvantage of Hydrothermal process
- Reduction of GO to rGO
- Metal assisted Chemical etching method
 - Deposition of noble metal
 - Reactions
 - The overall etching process.
- Catalyst assisted VLS growth process
 - Vapor-Liquid-Solid (VLS) mechanism
 - Fundamentals of homogeneous nucleation and growth

4. Chapter 4: Literature Review

5. Chapter 5: Experiments: Synthesis of samples

- Synthesis of Graphene Oxide using modified Hummer's method
 - Materials
 - Sample preparation
- Synthesis of N-doped reduced Graphene Oxide using Hydrothermal method
- Synthesis of N-type silicon nanowires

6. Chapter 6: Device Fabrication: Part-I (Supercapacitors)

- Preparation of Electrodes for supercapacitor
- Preparation of coplanar interdigital supercapacitor over flexible substrate
 - Design of CI supercapacitor
 - Preparation of the final CI device
 - Flexible Electrolyte preparation
 - Replication of Electrode design over flexible electrolyte gel

7. Chapter 7: Device fabrication: Part-II (Photodetector)

- Fabrication process of SiNWs/NrGO Photodetector

8. Chapter 8: Results and discussions

- Morphological Characterizations & analysis
 - Field Emission Scanning Electron Microscopy (FESEM) of N-doped rGO
 - FESEM of Silicon nanowires
 - HR-TEM of N-doped rGO
- Crystallographic characterization & analysis
 - X-Ray Diffraction (XRD) analysis
- Spectroscopic Characterization & analysis
 - UV-vis Spectroscopic analysis
 - Fourier Transform Infrared Spectroscopy of NrGO
 - X-Ray Photoelectron Spectroscopy (XPS) of NrGO
 - Raman Spectroscopy of NrGO

9. Chapter 9: Device Performance (Supercapacitor)

- Electrochemical study
 - Details of three electrode setup
 - CV performance of rGO coated Ni electrode
 - NORG- 6h electrode performance and different capacitance
 - NORG-12h electrode performance and different capacitance
 - NORG-18h electrode performance and different capacitance
 - NORG-24h electrode performance and different capacitance
 - Charge-Discharge Characteristics
- Charge-Discharge curve of NORG- 6h electrode

- Charge-Discharge curve of NORG- 24h electrode
- CV performance of coplanar interdigitate Supercapacitor

Chapter10: Device Performance (Photodetector)

- I-V analysis
- On-Off switching performance of NN type SiNW/rGO device

Chapter11: Conclusion & Future scope

- Conclusion
- Future scope

Chapter-1

Introduction



Introduction:

From the dawn of human civilization, we, human beings are very much curious about energy. Starting from fire to electricity, we thrive for energy to survive in this beautiful world since our inception. Later from the law of conservation of energy we come to know that energy can not be created or destroyed, it only can be converted to one form to another, unknowingly our predecessors did the same. Unfortunately, they faced the biggest issue regarding the same – energy storage. Our ancestors could convert one form of energy to another for using it in their needs and daily life but they were unable to store it for later purposes. With time human race is evolved and broaden its technological arms towards some charismatic inventions. At this level somehow energy can be stored but in a sloppy and less efficient manner- electrochemical energy storage. Scientists had managed to store electrical energy while having chemical reactions which causes flow of electrons. However foremost type of electrochemical energy storage systems was non-rechargeable. In the next step this energy storage system became rechargeable and thus divided into two parts based on their energy and power density i.e., battery and capacitor. With time our concern regarding energy storage has been shifted from store to recharge and now it comes to how fast we can charge. Thus, nanotechnology has gifted us the **supercapacitors**. Now a days for our modern age electronics and electrical devices we need a robust and impactful energy storage system which can have huge capacity to store energy, fast charging time and lower operating voltage limits. All of these issues can be resolved with these supercapacitors. In fact, as we are moving towards electrical vehicles by abandoning fossil fuelled vehicles it will be very important to have speed charging for less power consumptions. Even in recent cell phones, hybrid supercapacitor-battery is being used to have fast charging facilities. The emerging field of nanoscience and technology is trying to provide best solutions to the issues and helps us to invent more efficient supercapacitors. Nanostructures such as layers of 2D materials, porous materials with different defect states and functional groups are being observed and used to form best of supercapacitors. It gives huge motivation to scientists all over the world to dig in more into these materials and structures. Maybe we can charge our EVs and cell phones instantly in near future!

In practically every aspect of our life, nanoelectronics technology has had a significant impact, owing to the sophisticated disciplines employed by the semiconductor industry. All of those electronic devices are being made smaller and with better performance these days. Transistors,

diodes, and other modern integrated circuit components are built using both a top-down and bottom-up technique. As Moore predicted in 1965, the cost and size of the fundamental transistor continue to decrease by half every two years. In 2014–2015, the production technology alone is predicted to have improved, resulting in a reduction in transistor size from the current 28 nm to 14 nm. According to predictions, this manufacturing method will eventually be unable to produce smaller sizes due to fundamental physical constraints. For complementing opto-electrical purposes, a bottom-up method of circuit assembly using atomic, single-molecule, carbon nanotube, quantum dot, or **nanowire** building blocks can be useful. However, the same physical restrictions will apply. Another illustration is when the surface of a smaller object differs electrically from the interior. The increased surface-to-volume ratio also makes the nanostructure more sensitive to its environment, which may be advantageous (for sensors) or harmful (for other purposes) (electronic or photonic transport, light generation). They are potential not just for computation but also for connecting structures and chemical, biological, and medical detection. Nanostructures' properties can be incredibly sensitive to changes at their surface due to their large surface-to-volume ratio. It is obvious that the domains of nanoscience and technology are closely intertwined, and that frequently there is no way to tell them apart. Challenges have so far also emerged because future device shrinking calls for even superior precision technology, which will constrict traditional planar manufacturing technology. Materials with one-dimensional (1D) nanostructures have made it possible to find solutions to the problems. Excitement has been generated in numerous research labs across the world because of its potential for use in the electrical sector.

• **Reduced Graphene Oxide:**

Reduced Graphene oxide is part of 2D materials family and a hot topic of nanoscience and technology because of its unique properties and efficient applications in various fields of our daily life. Since of its high conductivity and large surface area, single layer graphene is the carbonous substance that researchers are most interested in studying because it may be used to create any type of sensing device. Graphite restacks easily, making the chemical production of large-scale single-layer graphene sheets from raw graphite extremely difficult. To address this issue, graphite sheets are first chemically oxidized to create layered graphene oxide (GO), which is then reduced to create reduced graphene oxide (rGO), which has nearly identical properties to graphene but a larger surface area due to its porous structure. To date, different

reducing agents have been employed to create rGO from GO, including hydrazine, hydroxylamine, urea, dimethyl ketoxime, pyrrole, ammonia, and pyrrolidine. In addition, several oxygen-containing groups have been added, including ascorbic acid, gallic acid, hydroquinone, and metal particles like Fe powder and Zn/HCL. In particular, groups that contain oxygen and nitrogen have been chosen above other chemicals for reduction purposes because these functionalities on the carbon moiety can start the production of sp³ carbon and defect density, which ostensibly opens the door for various electrochemical features. By adjusting the reaction's temperature and duration, optimised rGO with the best electrochemical properties and surface area can be produced. Although forming doped (nitrogen, oxygen, sulphur, etc.) and undoped or pure rGO in room temperature hydrothermally, which implies a 4-electron transfer pathway, is possible utilising non-toxic biological as a reducing agent, it is of great interest. The appropriate reduction of GO to rGO is thought to induce porosity in the rGO that increases the material's surface area. Good surface area results in a material's good and effective super-capacitive nature.

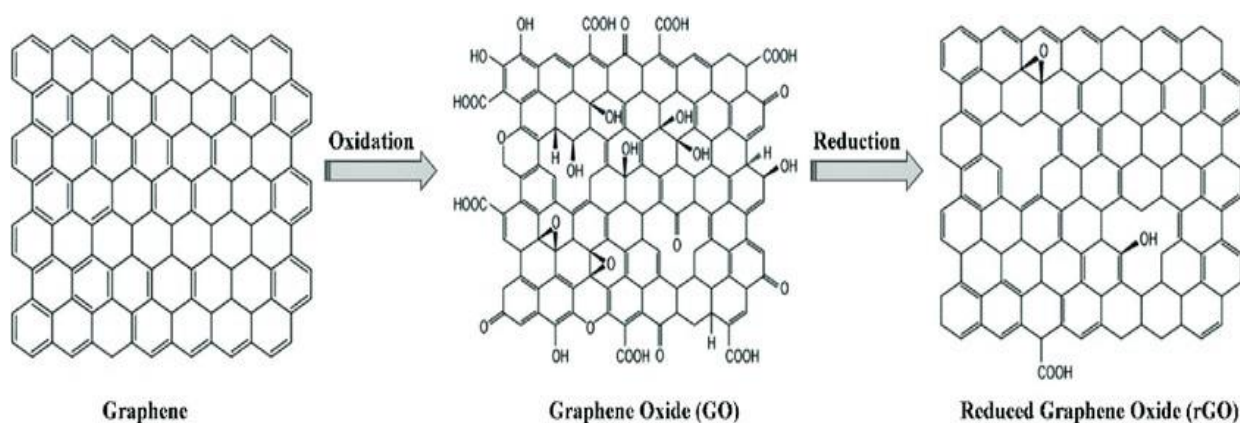


Fig 1.1. Reduction of Graphene oxide into reduced graphene oxide using oxidation
(collected from web page)

• **Properties of Reduced Graphene Oxide(rGO):**

Reduced graphene oxide or rGO has lots of interesting properties those are not available in case of 3D materials or bulk materials. This type of 2D material is having a layered like structure, porous nature and great specific surface area. Due to these reasons, it offers various tuneable properties which can be used for various type of applications such as supercapacitors (energy storage system), photodetectors, bio-sensors, temperature sensors etc. Carbonaceous materials

usually have high conductive nature and stability but having less energy density. Thus, these types of materials are not in that much industrial use with compared to metal oxides/hydroxides and conducting polymers in terms of supercapacitance. Significantly, due to different defect states, functionalized groups and different dopants such as nitrogen, oxygen, boron etc., reduced graphene oxide overcomes most of its difficulties in order to become a good supercapacitor and photodetector materials. Due to well-engineered pores and great surface area of rGO, it is easy to get more contact with electrolytes which facilitates easier diffusion of ions throughout the system.

The porous nature and different defect states of reduced graphene oxide layer brings indirect band gap of lower range which causes easier transportation of electrons through the bands (conduction band and valance band). Thus, it has a low work function which leads to a great photo-electric effect. Due to this it has a wide range of opto-electronic applications, such as photodetector, photodiode etc. The band gap of pure rGO can be tuned using different dopants which will cause multiple applications in different fields.

• **Supercapacitor:**

In today's energy-dependent world, electrochemical devices for energy storage and conversion such as batteries, fuel cells and electrochemical supercapacitors (ESs) have been recognized as the most important inventions among all energy storage and conversion technologies. The electrochemical supercapacitor, also known as a supercapacitor, ultracapacitor or electrochemical double-layer capacitor is a special type of capacitor that can store relatively high energy density compared to storage capabilities of conventional capacitors. ES devices posses several high impact characteristics such as fast charging capabilities, long charge-discharge cycles and broad operating temperature ranges. As a result, their use in hybrid and electrical vehicles, electronics, aircraft and smart grids is widespread. Although ES systems still face some challenges, such as relatively low energy density and high cost, further development will allow ES to work as power devices in tandem with batteries and fuel cells and also function as stand-alone high energy storage devices. For energy storage devices, energy density and power density are very important parameters for characterizing the performance of the devices. Energy density defines the amount of energy that can be stored in a given volume of weight of the material. Power density defines the total energy per unit time which can be stored into the device. So, the ideal storage device should have both high energy density and high-power density. To compare the energy and power capabilities a representation

known as the Ragone plot or diagram has been developed has been shown in the figure. Batteries have high energy density, but poor power density. Fuel cells have the highest energy density and lowest power density. By contrast with them, supercapacitors could possess high power density and notable increased high energy density. Supercapacitor is also known as electric double-layer capacitor (EDLC), super condenser, pseudo capacitor or ultracapacitor. Compared to conventional electrolytic capacitors the energy density is typically in the order of hundreds of times greater in supercapacitors. In comparison with conventional batteries or fuel cells, EDLCs also have much higher power density. The present energy crisis has created a growing demand for efficient, portable and high-power energy storage devices. Supercapacitors are fast emerging as a promising potential solution to this problem.

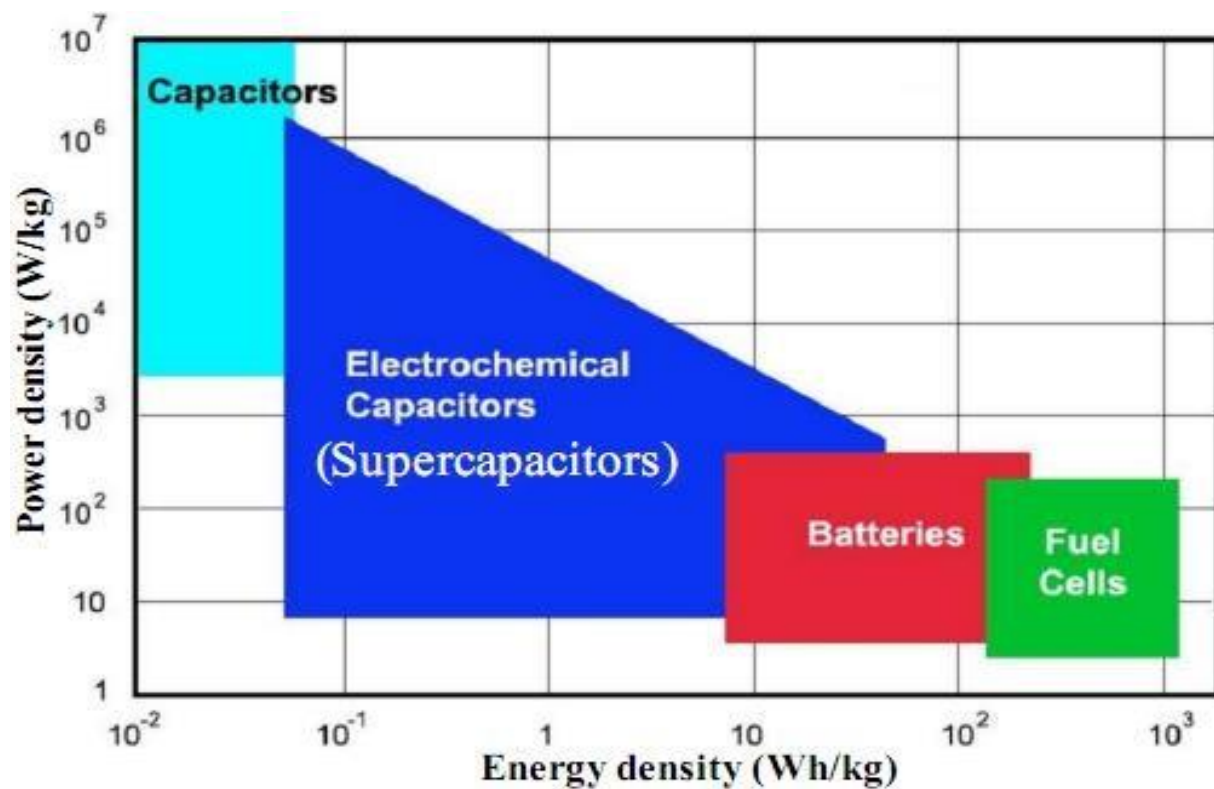


Fig1.2. Ragone plot of various energy storage devices (adopted from webpage)

➤ **Classification of Supercapacitors:**

Based upon present scenarios, supercapacitors can be divided into three general classes: electrochemical double-layer capacitors, pseudo capacitors and hybrid capacitors. Each class is characterized by its unique mechanism for storing charge. These are

respectively, non-Faradaic, Faradaic and a combination of the two. Faradaic processes, such as oxidation-reduction reactions, involve the transfer of charge between electrode and electrolyte. A non-Faradaic mechanism, by contrast, does not use a chemical mechanism. Rather charges are distributed on surfaces by physical processes that do not involve the making or breaking of chemical bonds. A graphical taxonomy of the different classes and subclasses of supercapacitors is presented in the below figure.

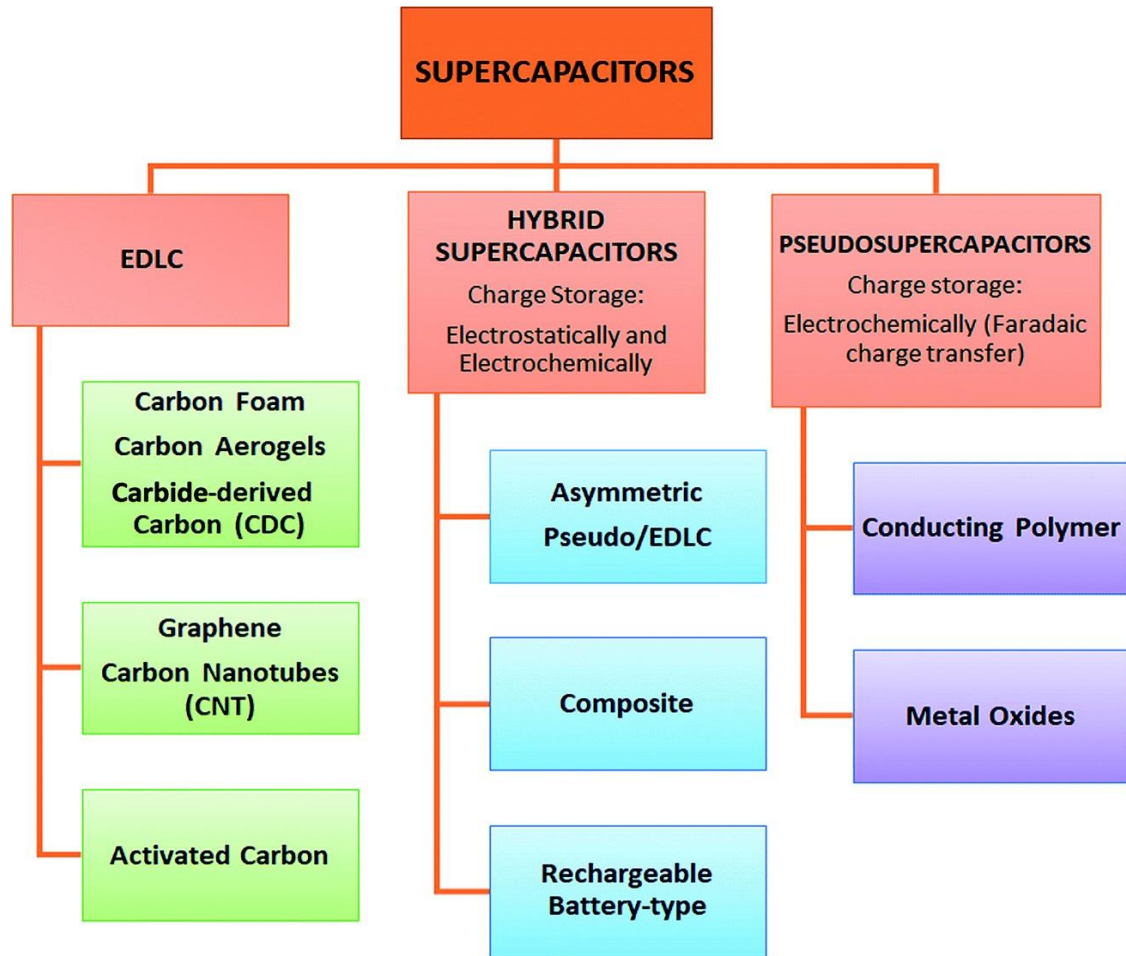


Fig 1.3. Classification of supercapacitors (adopted from webpage)

Electrochemical double-layer capacitors (EDLC):

Electrochemical double-layer capacitors are constructed from two electrodes. An electrolyte and a separator. Below figure provides a schematic of a typical EDLC. Like conventional capacitors, EDLCs store charge electrostatically or non-faradaically and there is no transfer of charge in between electrode and electrolyte. EDLCs utilize an electrochemical double-layer of charge to store energy. As voltage is applied charge accumulates on the electrode surface. Following the natural attraction of unlike charges,

ions in the electrolyte solution diffuse across the separator into the pores of electrode of opposite charge. However, the electrodes are engineered to prevent the recombination of the ions. Thus, a double layer of charge is produced at each electrode. These double layers allow EDLCs to achieve higher energy densities than conventional capacitors. Because there is no transfer of charge between electrolyte and electrode, there are no chemical or compositional changes associated with non-Faradaic process. For this reason, charge storage in EDLCs is highly reversible, which allows them to achieve very high cycling stabilities. EDLCs generally operate with stable performance characteristics for a great many charge-discharge cycles, sometimes as many as 100000 cycles. On the other hand, electrochemical batteries are generally limited to only about 103 cycles. Because of their cycling stability, EDLCs are well suited for application that involves non-user serviceable locations such as deep sea or mountain environments and automobiles.

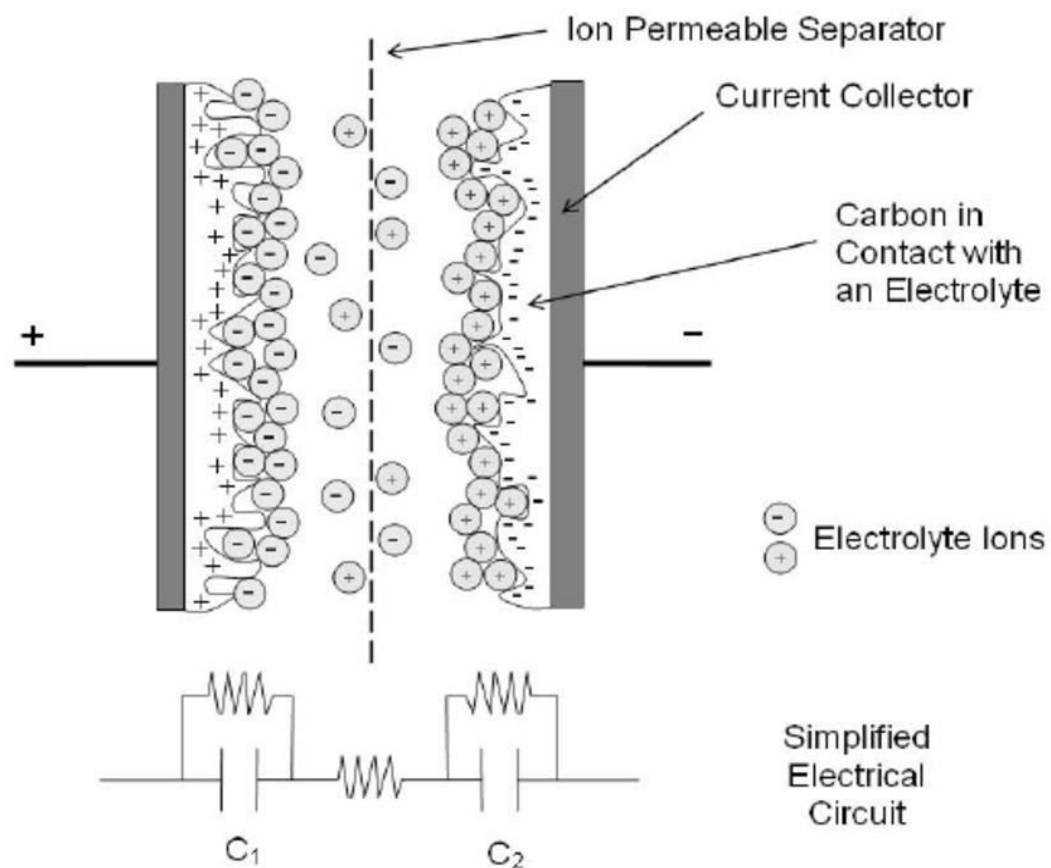


Fig 1.4. Schematic diagram of EDLC (adopted from webpage)

✚ Pseudo-capacitor:

Pseudocapacitors store charge faradaically by transferring charge between the electrode and the electrolyte, in contrast to EDLCs, which do it electrostatically. This is accomplished through electrosorption, oxidation-reduction reactions and intercalation processes. These faradaic processes may allow pseudocapacitors to achieve greater capacitance and energy density than EDLCs.

There are many electrode materials those are wont to store charge in pseudocapacitors like conducting polymers, metal oxides, chalcogenides nitrides etc. The charge transfer that takes place in these reactions is voltage dependent, so a capacitive phenomenon occurs. There are two styles of reactions that may involve a charge transfer that's voltage dependent. One is redox reaction and another is adsorption of ions.

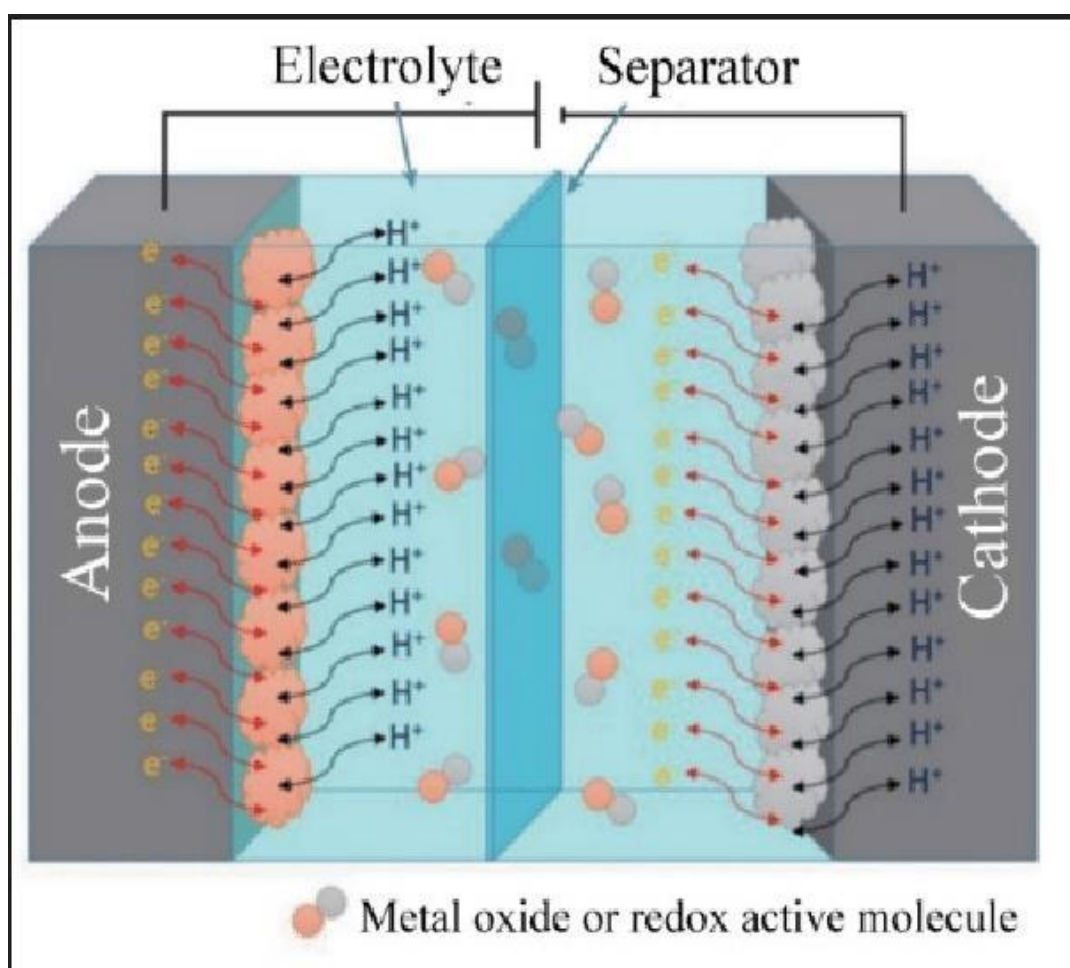


Fig 1.5. Schematic diagram of pseudocapacitors (collected from web page)

Hybrid Capacitors:

Hybrid capacitors attempt to exploit the relative advantages and mitigate the relative disadvantages of EDLCs and pseudocapacitors to realize better performance of the devices. Utilizing both Faradaic and non-Faradaic processes to store charge, hybrid capacitors have achieved energy and power densities greater than EDLCs without sacrificing the cycling stability and affordability that have limited the success of pseudocapacitors. Research has been focused on three different types of hybrid capacitors, distinguished by their electrode configuration: composite, asymmetric and battery-type respectively.

• **Application of Supercapacitor:**

➤ **Automobile:**

One of the most important and widely industry-based application of supercapacitor is automobile vehicles. Due to the crisis of fossil fuel, the world is now directing towards electrical vehicles (EVs). Hybrid electric vehicles (HEV) and pure electrical vehicles (PEV) have become popular and near main stream automobile industry in recent years. Both of these vehicles contain an electrical machine for propulsion purpose. When the vehicle starts to move off, some initial power is required by the motor can be several times of average power demand. Because of this impulsive power, both input and output power capability should be higher. High powered Li-ion batteries are having great energy density but has limited output power capability. Supercapacitors come into the scene as a solution due to its good input and output power density or capability. Therefore, supercapacitors play a huge and important role in automobile industry.

➤ **Mobile Devices:**

Supercapacitors can take on different physical forms so that it can be used in a smaller and thinner version of it. Some new generation mobile phones or devices use xenon flash which is inbuilt into the phone camera to enable good quality photo when light is dim. This flash requires huge power in an instant. If the mobile should be capable of dealing with this power consumption it would have to be unnecessarily bulk and heavy, failing to which leads to short battery life. To resolve this issue some of the brand in mobile industry use supercapacitors to supply the surged power using voltage from the existing battery which decrease the load of main battery and maintain the over all load

same as previous. For example, during the flash on situation, overall battery current can be suppressed at 0.2A while the flash may have current up to 4A.

As a result, the battery does not have to be large to cater to temporal high-power demands.

➤ **Micro-Grid:**

The micro-grid is called as a possible next generation energy network. It consists of electrical power generation units as well as electrical energy storage components. Popular electrical power generator includes photovoltaic cell, wind turbine, fuel cell and micro turbine while commonly used electrical energy storage units would be the supercapacitor and batteries. As the micro-grids can be inter-connected to the power grid, it is able to supply or demand power from the power grid. At times this configuration is known as the smart grid. The micro-grid has the capability of reducing carbon emission through green energy harnessing as well as having the capability of providing self-sustainable energy. Thus, it is regarded as a contender for the next generation energy network.

● **Nanowires:**

One dimension of the order of a nanometer characterizes a nanowire (10⁻⁹ meters). Alternatively, structures with a lateral size limited to tens of nanometers or less and a limited to longitudinal size might be referred to as nanowires. Because of these scales, quantum

The impacts of mechanics are crucial. Nanowires come in a variety of forms, including metallic (such as Ni, Pt, and Au), semiconducting (such as InP, Si, and GaN), insulating (such as SiO₂, and TiO₂), and molecular. Repeating molecules, either biological (like DNA) or inorganic (like atoms), make up molecular NW (e.g., MoS₂-xIx). Typically, nanowires have an aspect ratio of 100 or higher. They are hence frequently referred to as 1-D materials. The interesting characteristics of NWs are not present in bulk or 3-D materials. Because they are quantum confined, electrons in NWs have energy levels that are distinct from the traditional continuum of energy levels or bands present in bulk materials. The NWs can be used as active devices or linkages in the construction of

fundamental components for upcoming nanoelectronics devices, and they have a great deal of potential to improve the functionality of the electronics. Due to its compact size and minimal power usage, it is currently the industry leader.

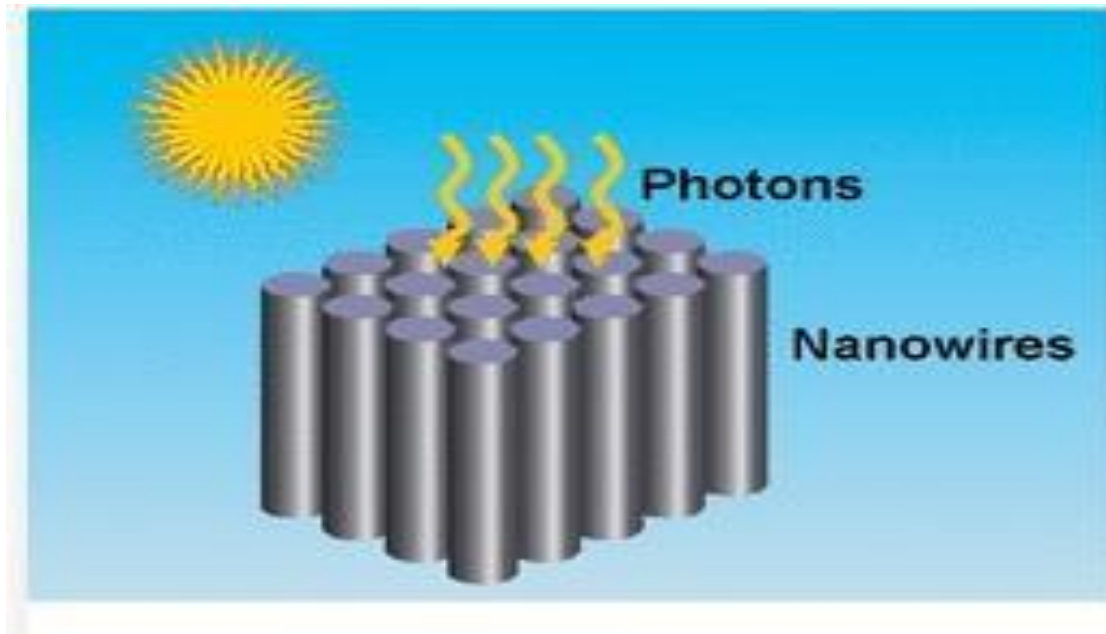


***Fig1.6: Schematic diagram of photoelectric effect of nanowires.
(Collected from web page)***

- **Semiconducting nanowires:**

The most adaptable building blocks for optical and (opto-) electronic circuits at the nanoscale are likely semiconductor nanowires. In contrast to atoms, single molecules, and nanoparticles, nanowires are easily joined using standard tools and have been demonstrated to work with silicon- or germanium-based technology. Electronic properties of semiconductor nanowires can be altered by varying the semiconductor, doping, or diameter. The main obstacles to the practical use of semiconducting nanowires in (Opto-) electronic circuits are the handling, positioning, and processing of many semiconducting nanowires as well as precise control over the diameter and impurity doping level. It would be necessary to develop cost-effective and dependable methods of individually contacting enormous nanowires in order to take advantage of the lower size. There are numerous ways to create semiconductor nanowires, which can be divided into two categories: bottom-up and top-down approaches. Bottom-up procedures include chemical vapour deposition (CVD), molecular beam epitaxy

(MBE), the vapor-liquid-solid (VLS) process, the solution-liquid-solid (SLS) process, and others that build structures additively from their constituent parts. A larger piece of material is chopped into smaller pieces using sculpting or chemical etching in top-down manufacturing processes including lithography, electrophoresis, and others.

using a subtractive method. These are quite simple to use, and the next chapter will explain them. Electronics (logic devices, diodes), photonics (lasers, photodetectors), biological (sensors, drug delivery), energy (batteries, solar cells, thermoelectric generators), and magnetic (spintronic, memory) devices.

• **Properties of Nanowires:**

Numerous intriguing characteristics of nanowires can be observed that are uncommon in bulk or 3-D materials. Due to their quantum confinement, electrons in nanowires inhabit energy levels that differ from the traditional energy spectrum or bands seen in bulk materials. Certain NWs show unusual quantum confinement characteristics, which manifest in discrete electrical conductance values. These discrete values result from a quantum mechanical restriction on how many electrons can pass through the NWs at once. These discrete values, which are integer multiples of the quantum of conductance and are typically referred to as

$$\frac{2e^2}{h} \approx 77.41 \mu\text{S}$$

This is the opposite of the well-known resistance unit, known as the von-Klitzing constant R_K , which is approximately equivalent to 25.81 K Ω .

A nanowire's conductivity is predicted to be significantly lower than that of the analogous bulk material for a number of physical reasons. There is significant scattering from the wire boundaries when the wire width is less than the bulk material's free-electron mean free path. For instance, copper has a mean free path of 40 nanometers. The mean free path will be shorter for copper nanowires with a wire width smaller than

40 nm. As a result, conductivity is defined as the sum of the transmission of various quantized energy levels through distinct channels. The number of channels accessible for the passage of electrons decreases as the wire becomes thinner. Due to their lower electron density and lower effective mass, semiconductors like Si or GaAs exhibit more dramatic conductivity quantization than metals. It causes a rise in threshold voltage and can be seen in silicon fins with a width of 25 nm. Practically speaking, this implies that a MOSFET with silicon fins of such nanoscale size will require a greater gate (control) voltage to turn on the transistor when employed in digital applications.

Nanowires have additional unusual electrical characteristics as a result of their small size. Nanowire conductivity is heavily impacted by edge effects, unlike carbon nanotubes, where electron mobility can fall into the ballistic transport regime. The edge effects are caused by atoms that are not completely bound to nearby atoms at the nanowire surface, as opposed to atoms in the majority of the nanowire. Unbonded atoms are a common source of nanowire defects, and they may cause the nanowire to conduct electricity less well than the bulk material. Edge effects become more important when a nanowire reduces in size because the surface atoms become more abundant than the atoms within the nanowire.

• **Applications of Nanowires:**

Silicon (Si) nanostructures have a wide range of uses and are well-documented as promising building blocks for devices in the fields of nanoelectronics, optoelectronics, energy conversion, and energy storage, as well as bio- and chemical sensors. Silicon (Si) is still the most important material for the current semiconductor industry.

In order to apply nanowire technology in commercial settings, researchers created a technique for joining nanowires in 2008: a sacrificial metal nanowire is placed next to the ends of the components to be joined (using a SEM's manipulators), and then an electric current is applied, melting the wire ends. The process combines wires as tiny as 10 nm. Ballistic photon waveguide applications for nanowires in interconnects and

logic arrays are being researched. While electrons move along the outer shell of the tube, photons move inside the tube. In a molecular computer, connecting molecules-scale entities is made possible by conducting nanowires. Transparent electrodes for flexible flat-screen displays are being researched as conducting nanowire dispersions in a variety of polymers. Due to their high Young's modulus, their use in composite materials that improve mechanical properties is being investigated. Since they are available in bundles, nanowires can be used as tribological additions to enhance the friction properties and dependability of electronic transducers and actuators.

Due to their high aspect ratio, nanowires are especially well suited to dielectrophoretic manipulation.

➤ **Photodetector:**

As an optical receiver, photo detectors are typically employed to convert light into electricity. Photo detectors utilise the idea of the photoelectric effect, which is brought on by light and affects a circuit. When light signals contact a junction, a photodetector converts those signals into a voltage or current. In the depletion area, electron-hole pairs are produced as a result of photon absorption. Photodiodes and phototransistors are a few of examples of photodetectors. Solar cells, which also collect light and transform it into electricity, are other optical components that function similarly to photodetectors. The LED, which functions as the opposite of a photodiode and transforms voltage or current into light instead of light into a voltage or current, is a comparable but distinct optical device. The photodetectors have an illumination window, which allows the light as an external input.

For use in high-speed optical communications, photodetectors with a quick enough response time, repeatability, and affordability that produces a detectable output for a small amount of light are worth looking into. The spectrum response, photosensitivity, quantum efficiency, dark current, temporal response (rising time and fall time), and other important factors help define photodetectors. The photocurrent ratio is used to define photosensitivity.

to the amount of light energy that strikes the object (in watts). The ratio of incident photons to produced electron-hole pairs is known as the quantum efficiency. The quantum efficiency (η) and responsivity (R) are defined as follows:

$$R = \frac{\text{Output current (I)}}{\text{Input optical power (P}_{opt})} \quad \text{and} \quad \eta = \frac{\text{number of output electrons}}{\text{number of Input photons}}$$

R and η are related through the relationship, $R = \frac{e\eta}{h\nu}$

e is electron charge, η is the efficiency, h is Plank's constant and P is light frequency.

Application of Photodetector:

- i) Photodetectors are utilized in a wide range of applications, including radiation detection, smoke detection, and flame detection, as well as to turn on street lighting relays.
- ii) Photodiodes are also used in modern oil-burning furnaces as a safety feature.
- iii) Street lights are another popular use. When the photodiode in the circuit fails to conduct, switch-on relays turn on the street lights, and when there is enough light, the lights are turned off.
- iv) AFM (Atomic Force Microscope) is another application in which a laser beam is directed from a laser diode onto the rear of the cantilever and then reflected by a photodiode. As the probes of the cantilever scrape over the surface of the material, the light beam on the diode yields the (x, y, z) location of the material. This gives a three-dimensional representation of the surface being scanned.
- v) Photodiodes are also used with lasers to form a security system. When the light projected by a laser to the photodiode is broken, a security alarm is tripped.

Semiconducting nanowires photodetectors have various optical properties. Optical polarization anisotropy is particularly important for fundamental studies of polarization-sensitive electronic states and potential applications in polarization-sensitive photodetectors. The main source of this process of anisotropy is the variation in the dielectric constant between the nanowire (ϵ) and its environment (ϵ_e). As a result, tuning of ϵ and ϵ_e directly controls the

optical polarization anisotropy. It has been predicted by theory and observed experimentally that there is a polarization memory effect present in ensembles of randomly oriented nanowires. Due to weighted ensemble averaging, the observed optical polarization anisotropy (which depends on both absorption and luminescence anisotropy) does not vanish in nanowire ensembles, but rather reduces when compared to the single nanowire value.

References:

1. S. Priya, D.J. Inman, Energy Harvesting Technologies, 2009, pp. 1e517, <https://doi.org/10.1007/978-0-387-76464-1>.
2. J.H. Jung, M. Lee, J. Hong, Y. Ding, C. Chen, L. Chou, Z.L. Wang, Lead-free NaNbO₃ Nanowires for a High Output Piezoelectric, 2011, pp. 10041e10046, <https://doi.org/10.1021/nn2039033>
3. Monroy, E.; Calle, F.; Pau, J.L.; Munoz, E.; Omnes, F.; Beaumont, B.; Gibart, P. AlGaIn-Based UV Photodetectors. J. Cryst. Growth 2001, 230, 537-543.
4. Brubaker DG, Fuller ML (1945) J Appl Phys 16:128
5. Klingshirn C, Hauschild R, Priller H, Zeller J, Decker M, Kalt H (2006) Adv Spectrosc Lasers Sens 231:277
6. Özgür, Ü.; Alivov, Y.A.; Liu, C.; Teke, A.; Reshchikov, M.A.; Doğan, S.; Avrutin, V.; Cho, S.J.; Morkoç, H. A Comprehensive Review of ZnO Materials and Devices. J. Appl. Phys. 2005, 98, 041301.
7. Look, D.C. Recent Advances in ZnO Materials and Devices. Mater. Sci. Eng. B 2001, 80, 383-387.
8. K. Batra, N. Sinha, S. Goel, H. Yadav, A.J. Joseph, B. Kumar, Enhanced dielectric, ferroelectric and piezoelectric performance of Nd-ZnO nanorods and their application in flexible piezoelectric nanogenerator, J. Alloy. Compd. 767 (2018) 1003e1011, <https://doi.org/10.1016/j.jallcom.2018.07.187>
9. S. Goel, N. Sinha, H. Yadav, S. Godara, A.J. Joseph, B. Kumar, Ferroelectric Gddoped ZnO nanostructures: enhanced dielectric, ferroelectric and piezoelectric properties, Mater. Chem. Phys. 202 (2017) 56e64, <https://doi.org/10.1016/j.matchemphys.2017.08.067>
10. Angshuman Deka and Karuna Kar Nanda, A comparison of ZnO films deposited on indium tin oxide and soda lime glass under identical conditions, AIP ADVANCES 3, 062104 (2013), <http://dx.doi.org/10.1063/1.4811091>.
11. D. Nunes, A. Pimentel, A. Gonçalves, S. Pereira, R. Branquinho, P. Barquinha, E Fortunato and R Martins, Metal oxide nanostructures for sensor applications, Semiconductor Science and Technology 34[4] 043001 (2019), <https://doi.org/10.1088/1361-6641/ab011e>
12. Jayanta Kumar Behera. Synthesis and Characterization of Nano-particles. M.Tech Thesis, NIT Rourkela.

13. V. Musat, A. Filip, N. Tigau, R. Dinica, E. Herbei, C. Romanitan, I. Mihalache, Munizer Purica, 1D Nanostructured ZnO Layers by Microwave-Assisted Hydrothermal Synthesis, *Revista de chimie* 69[10] (2018), 2788-2793.
14. D. E. Aspnes, "Optical properties of thin films," *Thin Solid Films*, vol. 89, no. 3, pp. 249–262, 1982.
15. G. Eda and M. Chhowala, "Chemically derived graphene oxide: towards large-area thin-film electronics and optoelectronics," *Advanced Materials*, vol. 22, no. 22, pp. 2392–2415, 2010.
16. M. S. Boon, W. P. S. Saw, and M. Mariatti, "Magnetic, dielectric and thermal stability of NiZn ferrite-epoxy composite thin films for electronic applications," *Journal of Magnetism and Magnetic Materials*, vol. 324, no. 5, pp. 755–760, 2012.
17. G. Sberveglieri, "Recent developments in semiconducting thin film gas sensors," *Sensors and Actuators B*, vol. 23, no. 2-3, pp. 103–109, 1995.
18. Nickel N H and Terukov E (ed) 2005 *Zinc Oxide—A Material for Micro- and Optoelectronic Applications* (Netherlands: Springer)
19. Mang A, Reimann K and Rubenacke St 1995 "Solid State Commun. 94 251
20. Bagnall D M, Chen Y F, Zhu Z, Yao T, Koyama S, Shen M Y and Goto T 1997 *Appl. Phys. Lett.* 70 2230
21. Brown M E (ed) 1957 *ZnO—Rediscovered* (New York: The New Jersey Zinc Company)
22. Look D C, Reynolds D C, Litton C W, Jones R L, Eason D B and Cantwell G 2002 *Appl. Phys. Lett.* 81 1830
23. Madelung O (ed) 1996 *Semiconductors—Basic Data 2nd Revised Edn* (Berlin: Springer)
24. Yu P Y and Cardona M 2005 *Fundamentals of Semiconductors 3rd edn* (Berlin: Springer)
25. Kamalasanan M N and Chandra S 1996 *Thin Solid Films* 288 112
26. Paraguay F D, Estrada W L, Acosta D R N, Andrade E and Miki-Yoshida M 1999 *Thin Solid Films* 350 192
27. Shionoya S and Yen W H (ed) 1997 *Phosphor Handbook By Phosphor Research Society* (Boca Raton, FL: CRC Press)
28. Nanto H, Sokooshi H and Usuda T 1991 *Solid-State Sensors and Actuators* 24–27 596

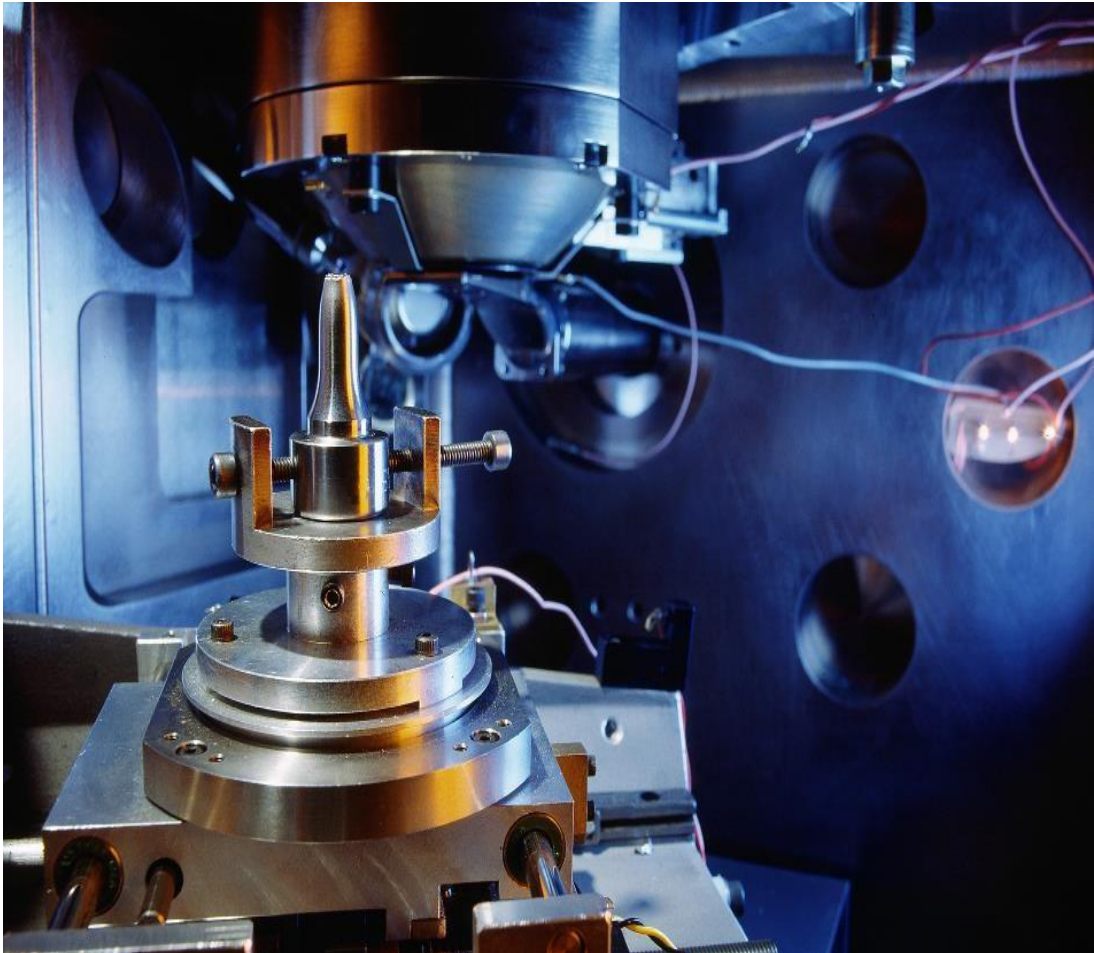
29. Florescu D I, Mourokh L G, Pollak F H, Look D C, Cantwell G and Li X 2002 J. Appl. Phys. 91 890
30. Ozgür U, Gu X, Chevtchenko S, Spradlin J, Cho S-J, Morkoc, H, Pollak F H, Everitt H O, Nemeth B and Nause J E 2006 J. Electr. Mater. 35 550
31. Suscavag M et al 1999 MRS Internet J. Nitride Semicond. Res. 4S1 G3.40
32. Ohshima E, Ogino H, Niikura I, Maeda K, Sato M, Ito M and Fukuda T 2004 J. Cryst. Growth 260 166
33. Reynolds D C, Litton C W, Look D C, Hoelscher J E, Claflin B, Collins T C, Nause J and Nemeth B 2004 J. Appl. Phys. 95 4802
34. Nause J and Nemeth B 2005 Semicond. Sci. Technol. 20 S45
35. Ardakani H K 1996 Thin Sol. Films 287 280
36. Tuomisto F, Saarinen K, Look D C and Farlow G C 2005 Phys. Rev. B 72 085206
37. Look D C, Hemsky J W and Sizelove J R 1999 Phys. Rev. Lett. 82 2552
38. Nomura K, Hiromichi O, Takagi A, Kamiya T, Hirano M and Hosono H 2004 Nature 432 488
39. Fryar J, McGlynn E, Henry MO, Cafolla AA, Hanson CJ (2004) Nanotechnology 15:1797
40. Wang ZL, Gao PX (2004) J Phys Chem B 108:7534
41. Gomez JL, Tigli O (2011) In: IEEE NMDC, Jeju
42. Carcia PF, McLean RS, Reilly MH, Crawford MK, Blanchard EN, Kattamis AZ, Wagner S (2007) J Appl Phys 102: 074512
43. Ozgur U, Alivov YI, Liu C, Teke A, Reshchikov MA, Dogan S, Avrutin V, Cho SJ, Morkoc H (2005) J Appl Phys 98: 041301
44. Klingshirn C, Fallert J, Zhou H, Sartor J, Thiele C, Maier-Flaig F, Schneider D, Kalt H (2010) Phys Status Solid B-Basic Solid-State Phys 247:1424
45. Hsueh TJ, Hsu CL, Chang SJ, Lin YR, Lin TS, Chen IC (2007) J Electrochem Soc 154:H153
46. Hahn YB (2011) Korean J Chem Eng 28:1797 J Mater Sci (2013) 48:612–624 623
47. S. Priya, D.J. Inman, Energy Harvesting Technologies, 2009, pp. 1e517, <https://doi.org/10.1007/978-0-387-76464-1>.
48. K. Ellmer and A. Klein, “Zinc Oxide and its Applications,” in Transparent Conductive Zinc Oxide-Basics and Applications, K. Ellmer, A. Klein and B. Rech, Eds., New York, Springer, pp. 1-33, 2008

49. A. Janotti and C. Van de Walle, "Fundamentals of Zinc Oxide as a Semiconductor," *Reports on Progress in Physics*, vol. 72, no. 12, pp. 1-29, 2009.
50. A. Janotti, J. Varley, J. Lyons and C. Van de Walle, "Controlling the Conductivity in Oxide Semiconductors," in *Functional Metal Oxide Nanostructures*, vol. 6, J. Wu, J. Cao, W. Han, A. Janotti and H. Kim, Eds., Santa Barbara, Springer, pp. 23-35, 2012.
51. A. Janotti and C. Van de Walle, "Native Point Defects and Doping in ZnO," in *Zinc Oxide Materials for electronic and optoelectronic device applications*, C. Litton, D. Reynolds and T. Collins, Eds., West Sussex, Wiley, pp. 113-134, 2011
52. C. Van de Walle, "Oxides as Semiconductors," Santa Barbara, 2014.
53. C. Jagadish and S. Pearton, *Zinc Oxide Bulk, Thin Films and Nanostructures: Processing, Properties and Applications*, Amsterdam: Elsevier, 2006.
54. C. Wang, L. Zhang, D. Xiang and R. Gao, "Metal Oxide Gas Sensors: Sensitivity and Influencing Factors," *Sensors*, vol. 10, no. 3, pp. 2088-2106, 2010.
55. Q. Peng and Y. Qin, "ZnO Nanowires and their Application for Solar Cells," in *Nanowires-Implementations & Applications*, Nanchang, InTech, pp. 157-178, 2011.
56. S. Gunalan, R. Sivaraj and V. Rajendran, "Green synthesis of ZnO nanoparticles against bacterial and fungal pathogens," *Progress in Natural Science: Materials International*, vol. 22, no. 6, pp. 693-700, 2012.
57. Abou El-Nour KMM, Eftaiha A, Al-Warthan A, Ammar RAA. Synthesis and applications of silver nanoparticles. *Arab J Chem* 2010; 3:135-40.
58. Nirmala JNS, Sagayaraj P. The influence of capping by TGA and PVP in modifying the structural, morphological, optical and thermal properties of ZnS nanoparticles. *Appl Sci Res* 2012;4(2):1079-90.
59. Alabi AB, Coppede N, Vilani M, Calestani D, Zappetini A, Babalola O, et al. Photocatalytic activity of nanostructured copper (II) oxide particles. *Ife J Sci* 2013;15(2):409-14.
60. Rao CNR, Rao GVS. Transition metal oxide, crystal chemistry phase transition and related aspects, NSRDS-NBS 49. Washington DC: U.S. Government Printing Office; 1974.
61. Mark TG, Zheng HL. Thin-film metal oxides in organic semiconductor devices: their electronic structures, work functions and interfaces. *NPG Asia Mater* 2013;5:e55, <http://dx.doi.org/10.1038/am.2013.29>.

62. Li D, Hu J, Fan F, Bai S, Luo R, Chen A, et al. Quantum-sized ZnO nanoparticles synthesized in aqueous medium for toxic gases detection. *J Alloys Compd* 2012; 539:205–9.
63. Wang ZH, Geng DY, Han Z, Zhang ZD. Characterization and optical properties of ZnO nanoparticles obtained by oxidation of Zn nanoparticles. *Mater Lett* 2009;63: 2533–5.
64. Samuel SM, Bose L, George KC. Optical properties of ZnO nanoparticles. *SB Acad Rev* 2009;1(2):57–65.
65. Karami H, Fakoori E. Synthesis and characterization of ZnO nanorods based on a new gel pyrolysis method. *J Nanomater* 2011, <http://dx.doi.org/10.1155/2011/628203> [Article ID 628203; 11 pp.].
66. Xudong W, Jinhui S, Zhong LW. Nanowire and nanobelt arrays of zinc oxide from synthesis to properties and to novel devices. *J Mater Chem* 2007; 17:711–20.
67. Lupan O, Pauporte T, Chow L, Viana B, Pelle F, Ono LK, et al. Effects of annealing on properties of ZnO thin films prepared by electrochemical deposition in chloride medium. *Appl Surf Sci* 2010; 256:1895–907.

Chapter-2

Instrumentation



• **Characterization Techniques:**

There are several different methods to characterize the sample to determine its phase, morphology, band gap, lattice vibration, crystallite size, interplanar distance, crystal plane etc. Here, in this work also these methods and machineries are being used to determine various properties of the prepared samples. There are mainly 3 types of characterization analysis that one sample can have, i.e.,

- **Morphological characterization**
- **Phase or crystallographic characterization**
- **Spectroscopic characterization.**

These three types of characterization techniques include a wide range of different apparatus and machineries. In this chapter major instruments and their basic working principle which were used in this project will be discussed briefly.

➤ **Morphological Characterization:**

Morphological characterization defines as the technique or method to get information about the morphology of the sample in micro and nano level. In nanotechnology, ordinary optical microscope can not be used due to their limited focus range which is not able to get the information in nano level. Hence, the need of electron microscopes has been emerged and resulting two types of very important electron microscope, i.e., **Scanning Electron Microscope (SEM)** and **Transmission Electron Microscope (TEM)**.

▪ **Scanning Electron Microscope (SEM):**

One of the most adaptable tools for inspecting and deciphering the morphology of microstructures is the scanning electron microscope (SEM). The surface of the object is routinely scanned by a focused electron beam in a scanning electron microscope (SEM), yielding a significant number of signals. An image is produced from these electron impulses and displayed on a cathode ray tube (CRT). There are two techniques to produce the electron beam:

- a) Thermionic emission; b) Field emission.

Thermal energy is used to regulate the source's electron emission to produce thermionic emission. In modern electron microscopes, field emission electron guns (FEG) are a great replacement for thermionic electron guns. Very minute topographic characteristics on the surface of whole or fragmented objects can be observed with a FESEM. Researchers in the fields of biology, chemistry, and physics utilise this technique to examine structures as small as 1 nanometer, or billionths of a millimetre. Organelles and DNA material in cells, synthetic polymers, and microchip coatings can all be studied with the FESEM.

- **Sample preparation for FESEM:**

The specimens that can be analysed must be compatible with high vacuum (10⁻⁵ mbar), as the SEM is operated under high vacuum. This suggests that liquids and objects made of volatile substances, like water, cannot be directly studied. To prevent contaminating the SEM specimen chamber, fine powder samples must also be firmly connected to a specimen holder substrate. A thin conductive layer must be sprayed or evaporated onto non-conductive materials before they are attached to a conductive specimen container. Common coating materials include carbon, Au, Pt, Pd, and their alloys.

- **Components of FESEM:**

- **Electron Guns:**

Modern FESEM systems require a constant electron beam from the electron cannon that has a high current, a small spot size, configurable energy, and minimal energy dispersion. A variety of electron guns are used in a FESEM system, and the quality of the electron beam produced by each differs greatly. The tungsten "hairpin" or lanthanum hexaboride (LaB₆) cathodes used in the first FESEM systems have since been replaced by field emission sources, which provide more current and less energy dispersion. The longevity of the emitter is a crucial consideration when selecting electron sources.

- **Electron Lenses:**

Electron beams can be concentrated by electrostatic or magnetic fields. The FESEM system, however, solely employs a magnetic field since an electron beam governed by one has less aberration. Electromagnets can be used to alter the electrons' routes.

- **Condenser Lenses:**

The electron beam will diverge after passing through an anode plate from the emission source. The electron beam is brought together and collimated by the condenser lens into a nearly parallel stream. Two rotationally symmetric iron pole pieces make form a magnetic lens, and a copper winding generates the magnetic field. The centre of each pole piece has a hole through which the electron beam can travel. Through a lens-gap between the two pole components, the magnetic field shapes (focuses) the electron beam. Condenser lens current can be changed to change the focus point's location.

- **Scan Coils:**

The scan coils cause the electron beam to be zigzagged as it passes over the object. The development of the image on the display and the scan movement are coordinated. The scan velocity controls both the screen's refresh rate and the amount of noise in the image. In scan coils, upper and lower coils are frequently utilized to avoid the formation of a circular shadow at low magnification.

- **Objective Lens:**

The electron beam will diverge below the condenser aperture. The electron beam is demagnified further and focused into a probe point on the specimen surface using objective lenses. The diameter of the electron beam on the specimen surface (spot size), which affects image resolution, decreases as aperture size and fundamentals of Scanning Electron Microscopy increase.

- **Stigmator Coil:**

The stigmator coils are used to rectify inconsistencies in the beam's x and y deflection, resulting in a perfectly round beam. When the beam is ellipsoidal rather than circular, the picture seems fuzzy and stretched.

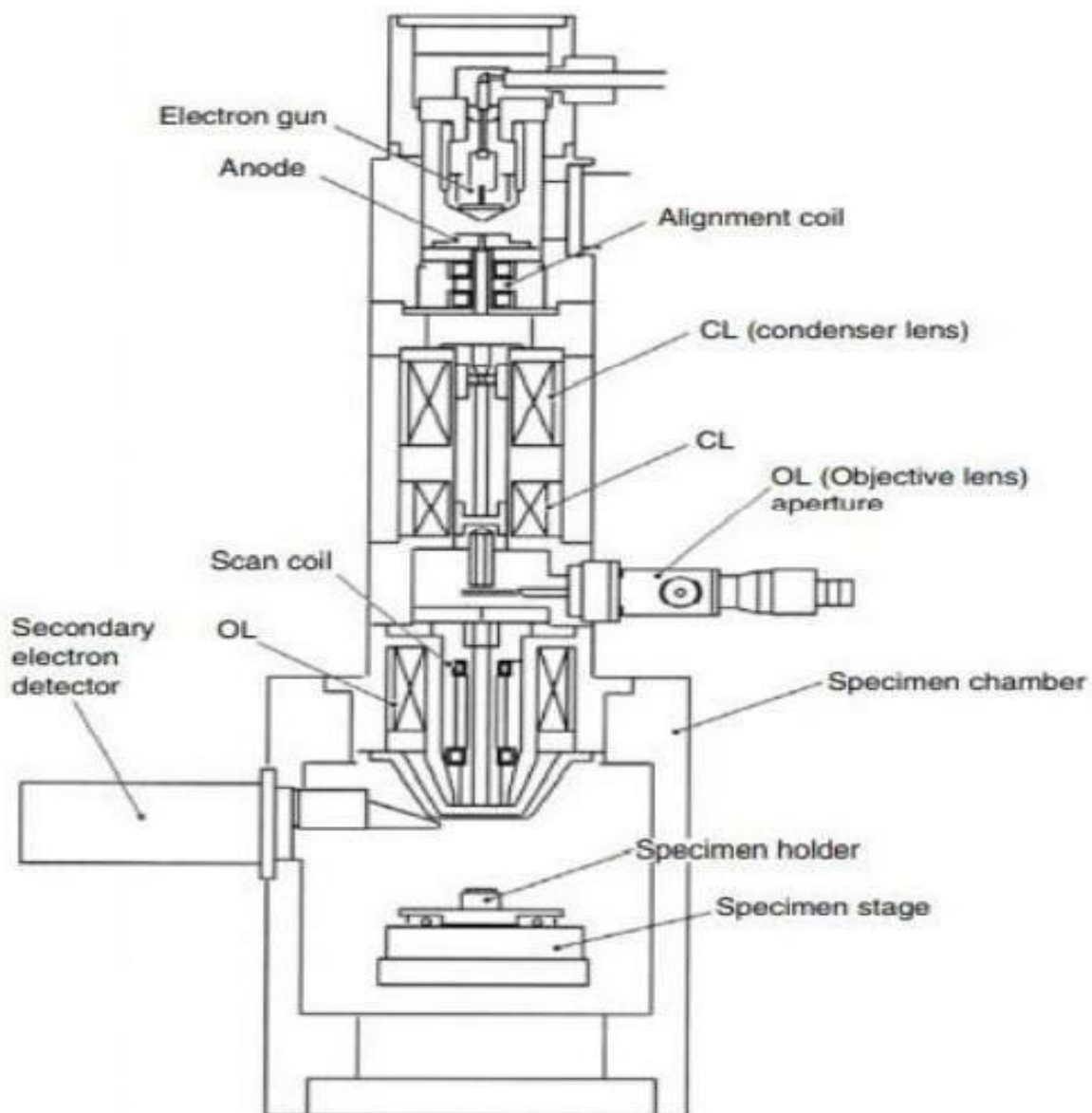


Fig 2.1. Schematic diagram of FESEM

- **Object Chamber:**

The object is coated with a conductive coating before being set on a particular holder. The object is anchored on a moveable stage and introduced into the high vacuum section of the microscope through an exchange chamber. The secondary electron emission detector (scintillator) is placed behind the object holder in the chamber.

- **Image Information:**

Complex interactions take place when an electron beam impinges on a specimen surface in a FESEM and stimulates various signals for FESEM inspection. It is possible to collect and display secondary electrons, back scattered electrons (BSEs),



Fig 2.2. FESEM (Hitachi S-4800) set up

transmitted electrons, and specimen current on a monitor. To determine the specimen's composition, the excited x-ray or Auger electrons are analysed. This part will cover the interactions of the electron beam with the specimen surface as well as the idea behind making pictures out of different signals.

- **Transmission Electron Microscope (TEM):**

A beam of electrons is transmitted through a material to create a picture in the microscopy technique known as transmission electron microscopy (TEM). Most frequently, the specimen is a suspension on a grid or an ultrathin slice that is less than 100 nm thick. As the beam passes through the specimen, a picture is created as a result

of the electrons' interactions with it. An imaging device, such as a fluorescent screen, a sheet of photographic film, or a sensor like a scintillator linked to a charge-coupled device, is then used to magnify and focus the image.

The operating modes of TEM instruments include diffraction, spectroscopy, scanning TEM imaging (STEM), conventional imaging, and combinations of these. There are numerous fundamentally diverse ways that contrast is formed, or "image contrast processes," even within conventional imaging. Contrast can result from position-to-position variations in thickness or density (referred to as "mass-thickness contrast"), atomic number (referred to as "Z contrast" using the standard abbreviation for atomic number Z), crystal structure or orientation (referred to as "crystallographic contrast" or "diffraction contrast"), the slight quantum-mechanical phase shifts that individual atoms produce in electrons that pass through them (referred to as "phase contrast"), the energy lost by electrons. Depending on the contrast mechanism as well as how the microscope is used—the settings of the lenses, apertures, and detectors—each mechanism provides the operator with a different kind of information. This means that a TEM is capable of returning a remarkable array of nanometer- and atomic-resolution data, and in ideal instances reveals not only the locations of all atoms but also the kind of atoms they are and the types of bonds they form with one another. Because of this, TEM is recognized as a crucial technique for nanoscience in the disciplines of biology and materials.

- **Components of HRTEM:**

A HRTEM is made up of a number of parts, including an electron emission source for creating the electron stream, an electron vacuum system in which the electrons move, a number of electromagnetic lenses, and electrostatic plates. The last two let the user direct and control the beam anyway they see fit. A mechanism that enables the insertion, movement, and removal of specimens from the beam path is also necessary. The electrons that escape the system are then utilised to generate an image using imaging devices.

- **Vacuum System:**

A standard HRTEM is evacuated to low pressures, typically on the scale of 10^{-4} Pa, to lengthen the mean free path of the electron gas interaction. This is necessary in two ways: first, to allow for the voltage differential between the cathode and the ground without causing an arc; and second, to drastically lower the frequency of electron collisions with gas atoms, a phenomenon known as the mean free path. It is necessary to regularly insert or replace HRTEM components such as film cartridges and specimen holders, hence the system must be able to re-evacuate. As a result, HRTEMs are not completely vacuum sealed and are furnished with several pumping systems and airlocks. There are various

stages in the vacuum system used to evacuate a HRTEM to a working pressure level. A turbo-molecular or diffusion pump is used to create the high vacuum level required for operations after first achieving a low or roughing vacuum with either a rotary vane pump or a diaphragm pump, which sets a low enough pressure to allow for its operation. The vacuum side of a low-pressure pump can be connected to chambers that hold the turbo-molecular pump's exhaust gases, allowing the low vacuum pump to run intermittently while the turbo-molecular pumps run continuously. Pressure-limiting apertures can be used to isolate different vacuum levels in separate parts of the HRTEM, such as a greater vacuum of 10^{-4} to 10^{-7} Pa or higher in the electron gun in high-resolution or field-emission HRTEMs.

- **Specimen Stage:**

In order to enter the specimen holder into the vacuum with the least amount of vacuum loss in other parts of the microscope, HRTEM specimen stage designs feature airlocks. The specimen holders can accommodate self-supporting specimens or sample grids of a standard size. 3.05 mm is the standard HRTEM grid size, with thickness and mesh sizes ranging from a few to 100 m. A meshed region with a diameter of roughly 2.5 mm receives the sample. Platinum, gold, molybdenum, and copper are the typical grid materials. The sample holder, which is connected to the specimen stage, receives this grid. Depending on the kind of experiment being run, a wide range of stage and holder designs are available. Aside from 3.05 mm grids, 2.3 mm grids are also occasionally, if infrequently, used. These grids were utilised mostly in the mineral sciences, where specimen material can be extremely uncommon and a significant amount of tilt might be necessary. The typical thickness of electron transparent specimens is less than 100 nm, while the exact value depends on the accelerating voltage.

The sample must be moved after being placed within a HRTEM in order to position the region of interest to the beam, as in single grain diffraction, in a certain orientation. The HRTEM stage allows for sample movement in the XY plane, Z height adjustment, and frequently a single tilt direction parallel to the axis of side entrance holds to accommodate this. On specialised diffraction holders and stages, sample rotation might be possible. Some contemporary HRTEMs have double-tilt sample holders, which are specialised holder designs that allow for two orthogonal tilt angles of movement. Some stage designs may only have X-Y translation available, such as top-entry or vertical insertion stages that were once popular for high resolution TEM research. Due to the combined demands of

mechanical and electron-optical restrictions, the design criteria for HRTEM stages are complicated, and there are specific models available for various techniques.

- **Electron Guns:**

The filament, a biasing circuit, a Wehnelt cap, and an extraction anode are the main parts that make up an electron cannon. Electrons can be "pumped" from the electron cannon to the anode plate and the HRTEM column, completing the circuit, by connecting the filament to the negative component power supply. The gun's goal is to produce an electron beam that emerges from the assembly at a specific angle, or gun divergence semi-angle, or. Electrons that escape the filament in a divergent fashion are, under appropriate operation, forced into a converging pattern, the minimum size of which is the gun crossover diameter, by designing the Wehnelt cylinder such that it has a higher negative charge than the filament itself.

- **Electron Lens:**

By focusing parallel electrons at a fixed focal distance, electron lenses are intended to mimic the behaviour of an optical lens. Electron lenses can function magnetically or electrostatically. The majority of electron lenses for HRTEM produce a convex lens using electromagnetic coils. The magnetic lens's radial symmetry must be maintained for the lens's field to be radially symmetrical; otherwise, astigmatism and other aberrations like spherical and chromatic aberration would worsen. Iron, iron-cobalt, or nickel-cobalt alloys, such as permalloy, are used to make electron lenses. These are chosen based on their magnetic characteristics, including permeability, hysteresis, and magnetic saturation. The yoke, the magnetic coil, the poles, the polepiece, and the external control circuitry are among the components. The boundary conditions for the magnetic field that creates the lens depend on how symmetrically the pole piece is made. Serious deviations in the magnetic field's symmetry might result from flaws in the pole piece's construction, and these distortions will ultimately reduce the lenses' capacity to recreate the object plane. A finite element study of the magnetic field is frequently used to determine the precise dimensions of the gap, the internal diameter and taper of the pole piece, as well as the overall design of the lens, while taking the design's thermal and electrical constraints into account.

- **Apertures:**

Apertures are annular metallic panels that allow electrons that are too far from the optic axis to pass through to be excluded. These are made of a thin metallic disc that allows axial electrons to flow through but prevents other electrons from doing so. Apertures reduce beam intensity as electrons are filtered out of the beam, which may be desired in the case of beam-sensitive samples. This permission of centre electrons in a HRTEM causes two effects concurrently. Second, this filtering eliminates electrons that are scattered at high angles for a variety of reasons, including chromatic or spherical aberration or diffraction from internal sample interactions. Condenser lenses, for example, have fixed apertures within the column. Other apertures, however, can be adjusted in the plane perpendicular to the beam path or inserted or removed from the beam path. Aperture assemblies are mechanical tools that enable the user to choose between various aperture sizes and trade off the intensity and filtering effect of the aperture. Micrometres are frequently included in aperture assemblies in order to change the aperture when optical calibration is necessary.

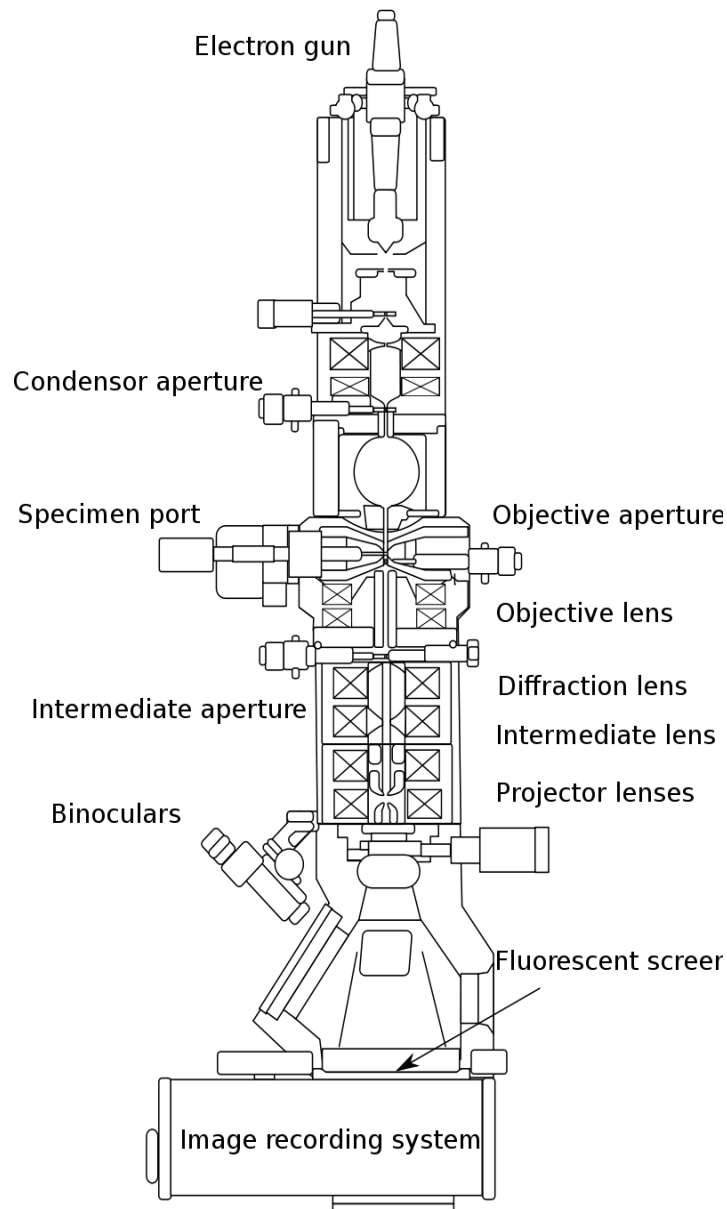


Fig 2.3. Schematic diagram of HRTEM

- **Image Contrast and interpretation:**

A high-resolution transmission electron microscopy image's contrast results from the electron wave's interference with itself in the image plane. Only the amplitude in the image plane is saved because we are unable to store an electron wave's phase. However, a significant portion of the sample's structural data is encoded in the electron wave's phase. It must be detected by tuning the microscope's aberrations (such defocus) so that

they translate the wave's phase at the specimen exit plane into amplitudes in the picture plane. Although the relationship between the electron wave and the sample's crystal structure is complicated, a qualitative understanding of the relationship can be quickly attained. The sample and each imaging electron interact separately. The wave of an electron above the sample can be roughly described as a plane wave incident on the sample surface. The positive atomic potentials of the atom cores attract it as it enters the sample, and it channels along the atom columns of the crystallographic lattice (s-state model). Bragg diffraction is caused simultaneously by the interaction of the electron waves in various atom columns. The holy grail of electron microscopy continues to be an accurate description of dynamical scattering of electrons in a sample not fitting the weak phase object approximation, which is practically all real samples. But there is enough knowledge about the physics of electron scattering and how electron microscope images are created to allow for accurate simulation of electron microscope images.



Fig 2.4. FEI Tecnai TEM

➤ **Phase or crystallographic characterization:**

The main instrument involved in phase or crystallographic characterization is X-ray Diffraction. It operates with X-Ray to determine the phase of the sample. Apart from that, it is also possible to get information about the crystallographic planes, interplanar distance, crystal size and the lattice structure of the prepared sample.

▪ **X-Ray Diffraction (XRD):**

X-rays are a form of electromagnetic radiation that has high energies and short wavelengths on the order of the atomic spacing for solids. When a beam of x-rays

impinges on a solid material, a portion of this beam will be scattered in all directions by the electron associated with each atom or ion that lies within the beam's pathway. Let us now examine the necessary conditions for diffraction of X-rays by a periodic arrangement of atoms. Diffraction occurs when a wave encounters a series of regularly spaced obstacles that are capable of scattering the wave and have spacing that are comparable in magnitude to the wavelength. Furthermore, diffraction is a consequence of specific phase relationships established between two or more waves that have been scattered by the obstacles. The phase relationship between the scattered waves, which will depend upon the difference in path length is important. One possibly results when its pathway length is an integral number of wavelengths.

Bragg's Law:

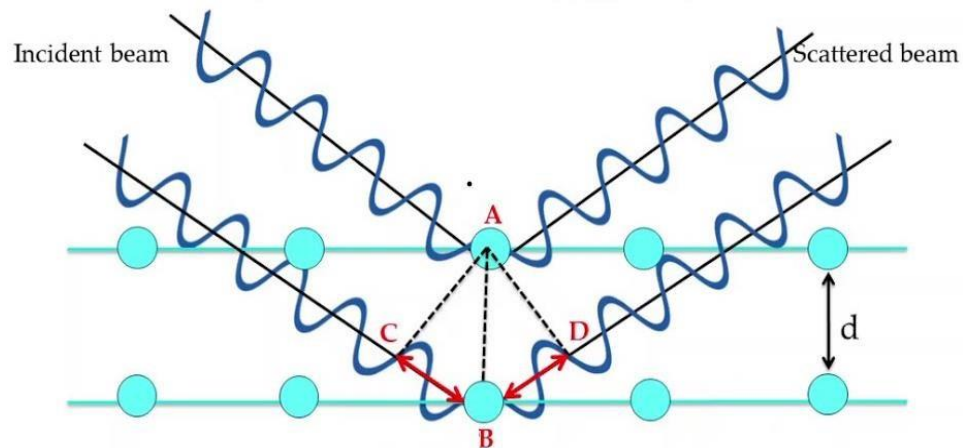


Fig 2.5. Bragg's Law of diffraction

Considering the two parallel planes of atoms, which have the same h , k and l Miller indices and are separated by the interplanar spacing d . Now assuming a parallel, monochromatic and coherent (in-phase) beam of x-rays of wavelength λ is incident on these two planes at an angle of θ . Two rays in this beam are scattered by atoms A and B. Constructive interference of the scattered waves occur also an angle of θ to the planes, if the path length difference (i.e. $CB+BD$) between these waves is equal to a whole number, n , of wavelengths. So, the condition for diffraction is

$$n\lambda = CB + BD$$

$$\text{or, } n\lambda = d \sin\theta + d \sin\theta$$

$$\text{or, } n\lambda = 2d \sin\theta$$

Production of X-ray:

X-rays are produced by bombarding a metal target (e.g., Cu, Mo usually) with a beam of electrons emitted from a hot filament (often tungsten). The incident beam will ionize electrons from the K-shell (1s) of the target atom and X-rays are emitted as the resultant vacancies are filled by electrons dropping down from the L (2p) or M (3p) levels. This gives rise to K_α and K_β lines.

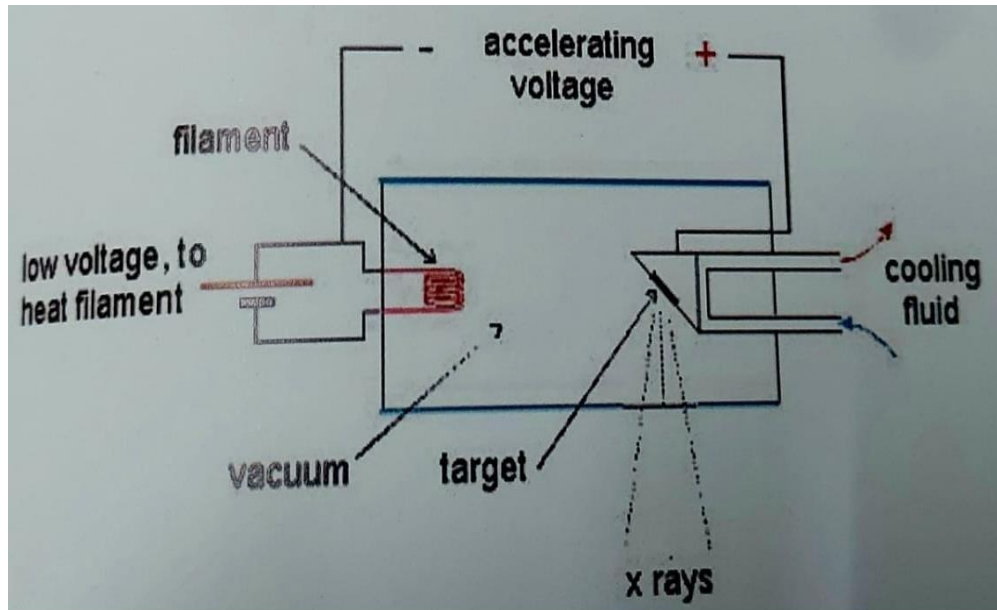


Fig 2.6. Production of X-Rays



Fig 2.7. X-Ray Diffraction (Bruker D8 advance)

Particle Size determination by Scherrer's formula:

Experimentally obtained diffraction patterns of the sample are compared with the standard powder diffraction files published by the JCPDS. The average grain size of the samples was calculated using Scherrer's formula:

$$D = \frac{0.9\lambda}{\beta \cos \theta}$$

Where, λ is the wavelength of x-rays,

And β is the full width at half maximum intensity in radians.

It is important to realize that the Scherrer's formula provides a lower bound on the particle size. The reason behind this is that a variety of factors can contribute to the width of a diffraction peak; besides particle size, the most important of these are actually is dependent on the factors like inhomogeneous strain and instrumental errors. If all of these other factors contributing to the peak width were zero, then the peak width

would be determined solely by the particle size and the Scherrer's formula would apply. If the other contributors to the peak width is non-zero, then the particle size can be larger than the predicted by this formula, with the "extra" peak width coming from the other facts.

➤ **Spectroscopic characterization:**

▪ **UV-VIS near infrared Spectroscopy:**

The optical transmittance, absorbance, and reflectance in the ultraviolet-visible spectral area are measured using UV-Vis-NIR Spectrophotometers. Measurements of optical transmittance, absorbance, and reflectance in the ultraviolet visible spectral area are made using UV-Vis near Infrared (UV- Vis-NIR) Spectrophotometers. The amount of radiation that is absorbed, transmitted, or reflected at each wavelength is quantified using UV-Vis absorption spectroscopy. Typically, this is done by measuring the absorption while scanning the wavelength range. To determine the degree of multiple bond or aromatic conjugation within molecules, it is frequently employed in organic chemistry. The method can be expanded to include gases and solids as well as go beyond absorption to measure reflected light as opposed to transmitted light.

Light absorption can be described by two fundamental laws as:

• **Lambert's Law:**

The proportion of incident light absorbed by a transparent medium is independent of the intensity of the light (provided that there is no other physical or chemical change to the medium). Therefore, successive layers of equal thickness will transmit an equal proportion of the incident energy.

Lambert's law can be expressed by

$$\frac{I}{I_0} = T$$

Where I is defined as the intensity of transmitted light, I_0 is defined as intensity of incident light and T is the transmittance.

- **Beer's Law:**

The absorption of light is directly proportional to both the concentration of the absorbing medium and the thickness of the medium in the light path.

A combination of the two laws (known jointly as the Beer-Lambert Law) defines the relationship between absorbance (A) and transmittance (T).

$$A = \log \frac{I_0}{I} = \log \frac{100}{T} = \epsilon cb$$

Where, A is absorbance, ϵ is molar absorptivity, c is molar concentration and b is path length.

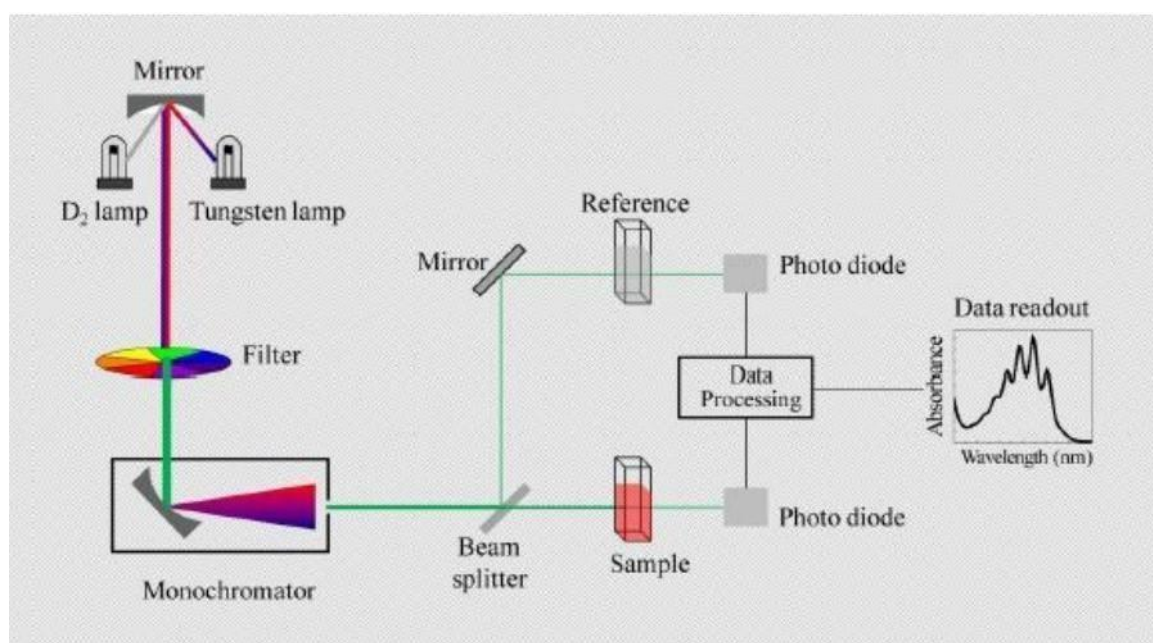


Fig 2.8. Basic working principle of UV-Vis spectroscopy

- **LIGHT REFLECTION AND REFLECTANCE SPECTRA:**

The spectrometer beam is directed into the sample, where it is reflected, dispersed, and transmitted through the sample material, resulting in diffuse reflectance (shown on the right). The accessory collects the back reflected, diffusely dispersed light (part of which is absorbed by the sample) and directs it to the detector optics. Diffuse reflection refers to the portion of a beam that is dispersed within a sample and returns to the surface.

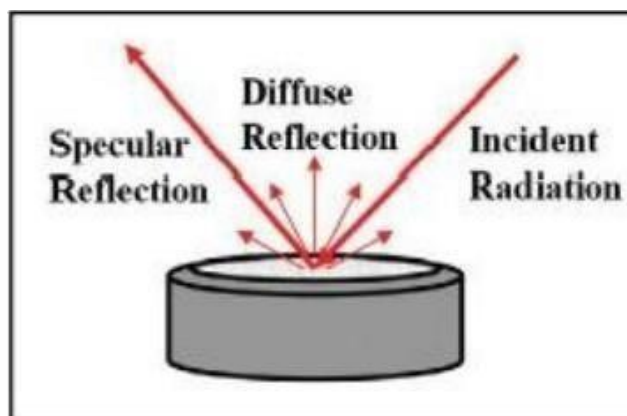


Fig 2.9. Diffuse and Specular Reflectance

Particle size, refractive index, homogeneity, and packing are further parameters that contribute to excellent spectral quality in diffuse reflectance sampling. The raw diffuse reflectance spectra will seem different from its transmission counterpart despite all of these sample preparation techniques (stronger than expected absorption from weak IR bands).

To correct for these discrepancies, a Kubelka-Munk conversion can be performed to a diffuse reflectance spectrum.

Kubelka-Munk Function:

$$F(R) = \frac{(1 - R)^2}{R} = \frac{k}{s}$$

R stands for the sampled layer's absolute reflectance, k for the molar absorption coefficient, and s for the scattering coefficient.

This spectral conversion for ibuprofen obtained via diffuse reflectance is illustrated in the spectrum above. The Kubelka-Munk converted spectrum for ibuprofen compares well to the transmission spectrum and is easily recognised using a transmission spectral data base library search.

- **Components of UV-Vis:**

- i) Spectrophotometer consists of the following components
- ii) A source of radiation of appropriate wavelength.
- iii) Monochromator and optical geometry.
- iv) Filter sample compartment.
- v) Detector, photomultiplier, measuring system and computer.

The UV VIS spectra carried out by Shimadzu UV 3600 spectrophotometer.



Fig 2.10. UV-VIS-NIS (SHIMADZU UV-3600) Spectrophotometer

- **FOURIER TRANSFORM INFRA-RED SPECTROSCOPY (FTIR):**

For studying the vibrational properties of synthesised materials, FTIR spectroscopy is a very useful tool. The band positions and absorption peak of thin films are influenced not only by their chemical composition and structure, but also by their morphology.

The preferred method of infrared spectroscopy is known as Fourier Transform InfraRed (FT-IR). Infrared spectroscopy involves passing IR radiation through a sample. The sample absorbs some of the infrared radiation and passes some of it through (transmitted). The resulting spectrum depicts the sample's molecular absorption and transmission, resulting in a molecular fingerprint. No two unique molecular structures produce the same infrared spectrum, just like a fingerprint. As a result, infrared spectroscopy can be used for a variety of purposes.

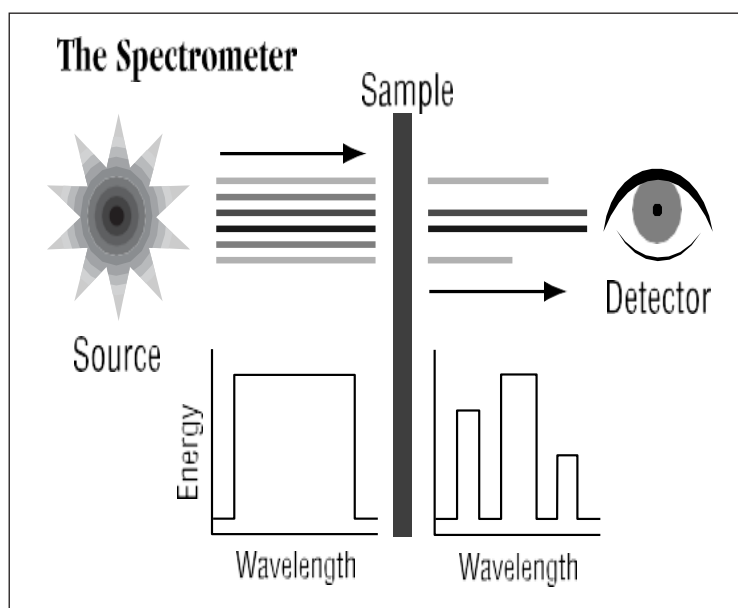


Fig2.11. Spectrometer

So, what kind of information can FT-IR give you?

- It can determine the quality or consistency of a sample
- It can determine the number of components in a mixture
- It can identify unknown materials

WHY INFRARED SPECTROSCOPY?

For over seventy years, infrared spectroscopy has been a workhorse technique in the laboratory for materials analysis. An infrared spectrum is a sample's fingerprint, with absorption peaks corresponding to the frequencies of vibrations between the bonds of the material's atoms. Because each material is made up of a different set of atoms, no two compounds have the same infrared spectrum. As a result, infrared spectroscopy can be used to positively identify (qualitatively analyse) any type of material. Furthermore, the size of the peaks in the spectrum indicates the amount of material present. Infrared is an excellent tool for quantitative analysis thanks to modern software algorithms.

OLDER TECHNOLOGY:

The first infrared instruments were dispersive in nature. Individual frequencies of energy emitted from the infrared source were separated using these instruments. A prism or grating was used to accomplish this. A visible prism separates visible light into its colours, and an infrared prism does the same (frequencies). A grating is a more modern dispersive element that separates infrared energy frequencies better. The detector counts the amount of energy that has passed through the sample at each frequency. As a result, a spectrum is created, which is a plot of intensity against frequency.

For several reasons, Fourier transform infrared spectroscopy is preferred to dispersive or filter methods of infrared spectral analysis:

- It is a non-destructive technique
- It provides a precise measurement method that does not require external calibration
- It can increase speed, collecting a scan every second

- It can increase sensitivity – one second scans can be co-added together to ratio out random noise
- It has greater optical throughput.

Why FT-IR?

In order to overcome the limitations of dispersive instruments, Fourier Transform Infrared (FT-IR) spectrometry was developed. The slow scanning process was the main issue. It was necessary to develop a method for measuring all infrared frequencies simultaneously rather than individually. An interferometer, a very simple optical device, was used to develop a solution. The interferometer generates a unique signal that contains all of the infrared frequencies "encoded." The signal can be measured very quickly, usually in a fraction of a second. As a result, the time element per sample is reduced from several minutes to a few seconds. A beam splitter is used in most interferometers to divide the incoming infrared beam into two optical beams.



Fig 2.12. An interferogram signal

A flat mirror, which is fixed in place, reflects one beam. The other beam reflects off a flat mirror that moves a very short distance (typically a few millimetres) away from the beam splitter thanks to a mechanism. When the two beams meet again at the beam splitter, they reflect off their respective mirrors and are recombined. The signal that exits the interferometer is the result of these two beams "interfering" with each other because one beam's path is fixed and the other's is constantly changing as its mirror moves.

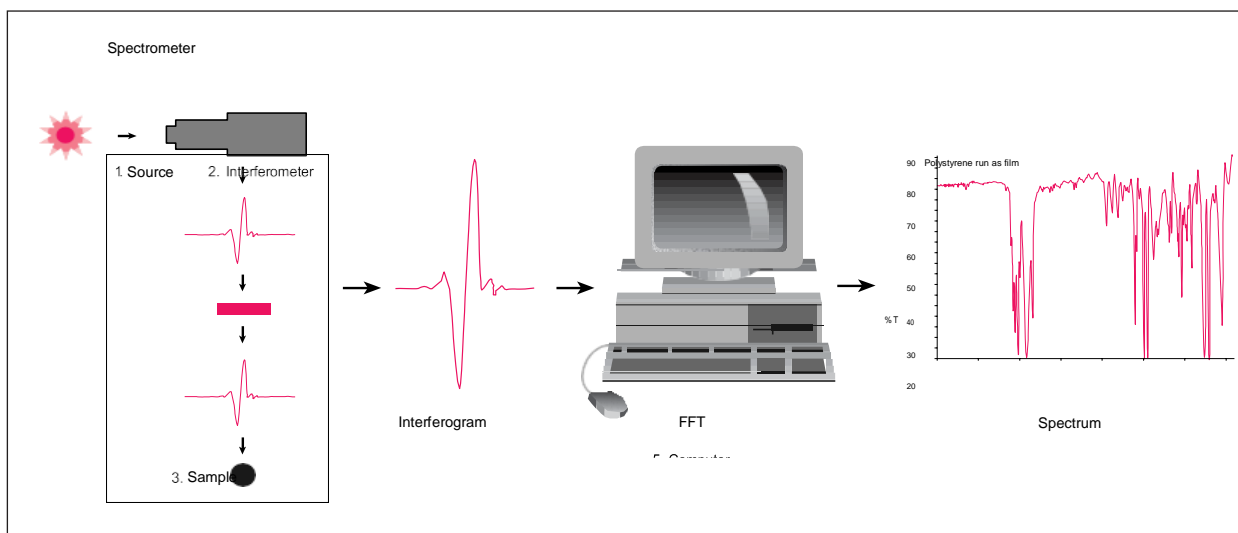


Fig 2.13. Process of generating an FTIR spectra

The resulting signal is known as an interferogram, and it has the unique property of having information about each infrared frequency that comes from the source in every data point (a function of the moving mirror position) that makes up the signal. This means that all frequencies are measured simultaneously as the interferogram is measured. As a result of the interferometer's use, measurements are extremely quick. The measured interferogram signal cannot be interpreted directly because the analyst requires a frequency spectrum (a plot of the intensity at each individual frequency) in order to make an identification. It's necessary to have a way of "decoding" the individual frequencies. The Fourier transformation, a well-known mathematical technique, can be used to accomplish this. The computer performs this transformation and then presents the user with the desired spectral information for analysis.

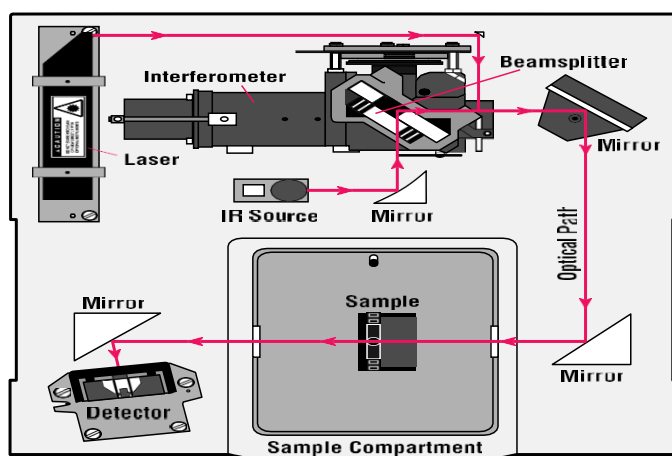


Fig 2.14. A simple spectrometer layout

THE SAMPLE ANALYSIS PROCESS:

The standard instrumental procedure goes like this:

1. **The Source:** A glowing black-body source emits infrared energy. This beam passes through an aperture that regulates how much energy is delivered to the sample (and, ultimately, to the detector).
2. **The Interferometer:** The beam passes through the interferometer, which performs "spectral encoding." The interferogram signal is then output from the interferometer.
3. **The Sample:** Depending on the type of analysis being performed, the beam enters the sample compartment and is transmitted through or reflected off the surface of the sample. This is where the sample's specific frequencies of energy, which are unique to it, are absorbed.
4. **The Detector:** The beam finally reaches the detector, where it is measured. The detectors used were created specifically to measure the interferogram signal.
5. **The Computer:** The measured signal is digitised and sent to the computer, which performs the Fourier transformation. The user is then presented with the final infrared spectrum for interpretation and any further manipulation.

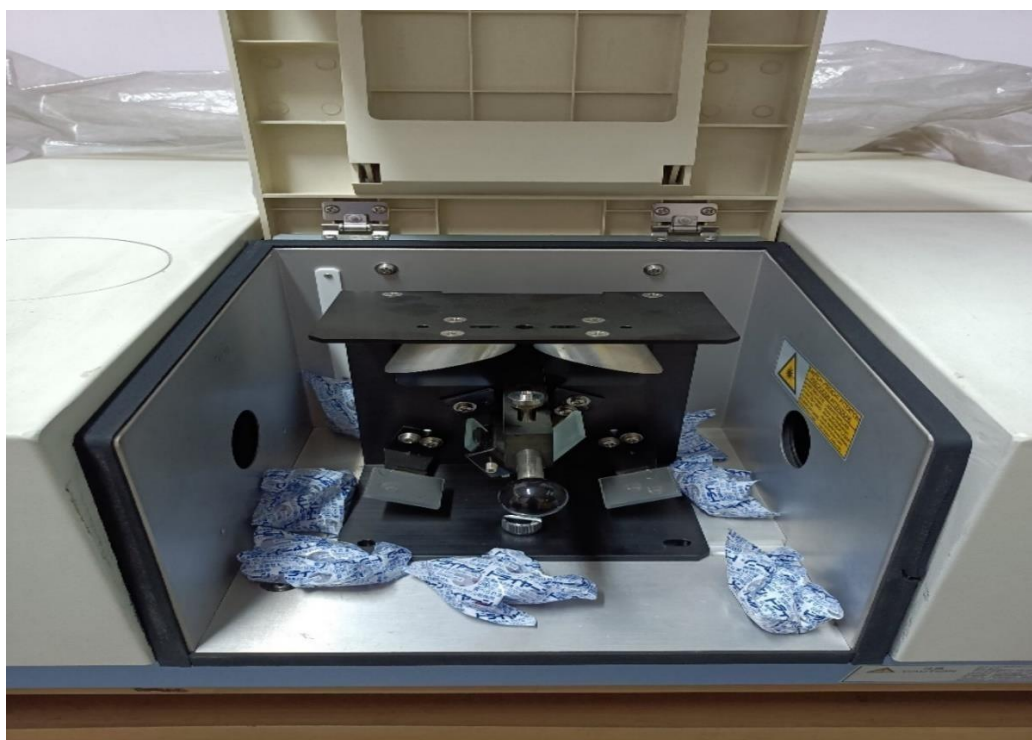


Fig 2.15. Internal components of FTIR instrument.

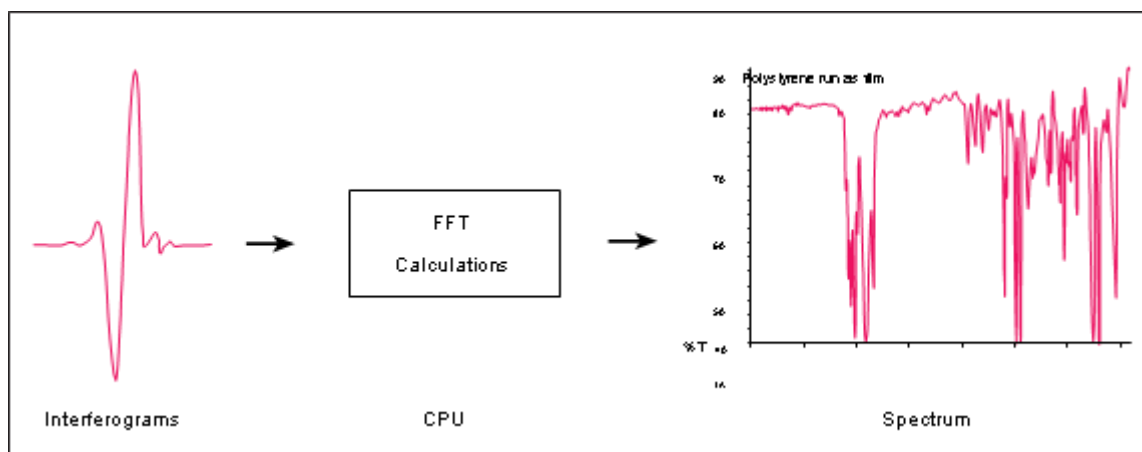


Fig 2.16. Internal Process for the formation of FTIR spectra

Because the absorption intensity must be measured on a relative scale, a background spectrum must also be measured. Normally, this is a measurement without a sample in the beam. This can be compared to the "percent transmittance" measurement taken with the sample in the beam. This method yields a spectrum that is devoid of all instrumental characteristics. As a result, all spectral features present are solely due to the sample. Because the instrument's spectrum is characteristic, a single background measurement can be used for multiple sample measurements.

▪ **Raman Spectroscopy:**

Raman scattering was first observed by Dr. C.V. Raman in 1928 and was used to investigate the vibrational states of many molecules.

▪ **Raman System:**

A typical Raman system consists of the following basic components: (1) Excitation source, usually a laser; (2) Optics for sample illumination; (3) Double or triple monochromator and (4) Signal processing system consisting of a detector, an amplifier and an output device. A sample is mounted on the sample chamber and laser light is focused on it with help of a lens. The scattered light is collected using another lens and is focused at the entrance slit of the monochromator. The monochromator effectively rejects stray light and serves as a dispersing element for incoming radiation. The light

leaving the exit slit of the monochromator is collected and focused on the surface of a detector. The optical signal is converted to an electrical signal within the detector and further manipulated using detector electronics. Such a signal is stored in computer memory for each predetermined frequency interval. In a conventional Raman system using photomultiplier tube (PMT) detector, light intensity at various frequencies is measured by scanning the monochromator. A plot of signal intensity against wavenumber constitutes its Raman spectrum.

▪ **Principle:**

When a sample is irradiated with an intense monochromatic light source (usually a laser), most of the radiation is scattered by the sample and the same wavelength as that of the incoming laser radiation is a process known as Rayleigh scattering. However, a small portion of the incoming light approximately one photon out of million is scattered at a wavelength that is shifted from the original laser wavelength.

1. Laser light excites the sample.
2. This light is scattered in all directions.
3. Some of this scattered light directed to the detector, which records the Raman spectrum.
4. This spectrum shows light at the original laser (Rayleigh) frequency and the Raman spectrum features unique to the sample.

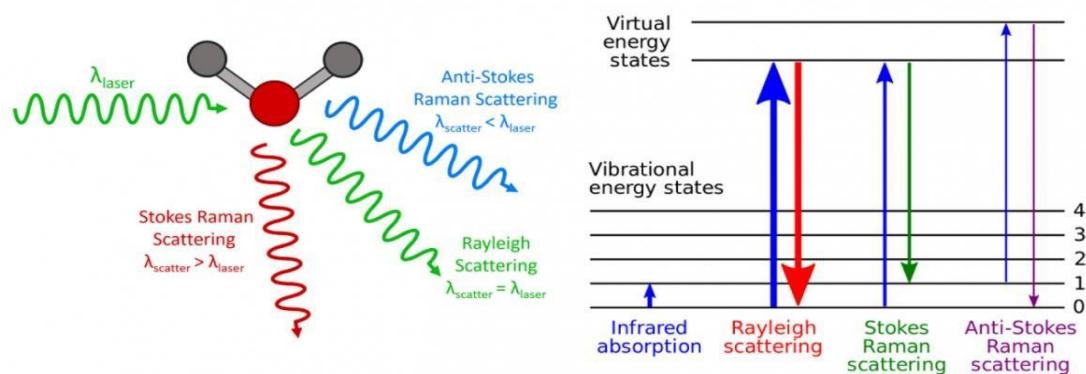


Fig 2.17. Different types of Scattering

The same transition between molecular vibration states (M) and (M*) in the infrared absorption can also result in Raman scattering. A key difference between Raman and infrared process is that, in the former process, the photons involved are not absorbed or

emitted but rather shifted in frequency by an amount corresponding to the energy of the particular vibrational transition. In the Stokes process, which is the parallel absorption, the scattered photons are shifted to lower frequencies as the molecule's abstract energy from the exciting photons; in the anti-stokes process, which is parallel to emission, the scattered photons are shifted to higher frequencies as they pick up the energy released by the molecules in the course of transitions to the ground state. Relaxation from the virtual state occurs almost instantaneously and is predominantly to the initial ground state. This process results in Rayleigh scattering, which is scattered light of the same wavelength as excitation laser. Relaxation to the first excited vibrational level results in a Stokes-Raman shift. Stokes-Raman shifted scattered light is of lower energy (longer wavelength) than that of the laser light. In addition, most systems have at least a small portion of molecules that are initially in an excited vibrational state. When the Raman scattering process starts from the excited vibrational level, relaxation to the ground state is possible, producing scatter of higher energy (shorter wavelength) than that of the laser light. This type of scatter is called anti-Stokes-Raman scattering. Two molecules can give exactly the same Raman spectrum and the intensity of the scattered light is proportional to the amount of material present. Thus, Raman spectrum provides both qualitative and quantitative information about the sample. The Raman spectrum carried out by *WITEC alpha 300R-RAMAN spectroscopy*.

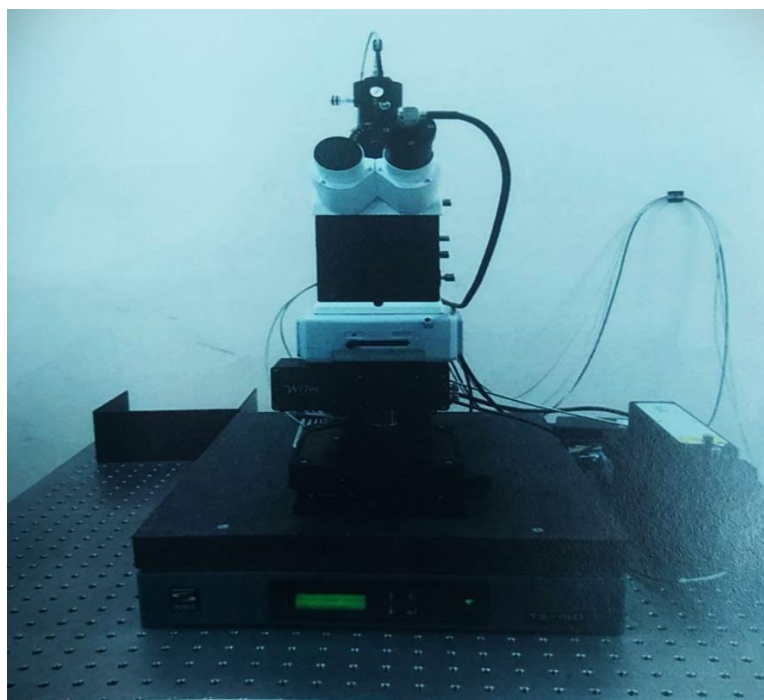


Fig 2.18. WITEC alpha 300R-RAMAN spectroscopy.

▪ **X-ray Photoelectron Spectroscopy (XPS):**

A surface-sensitive quantitative spectroscopic method based on the photoelectric effect called X-ray photoelectron spectroscopy (XPS) can identify the elements present in a material (its elemental composition) or that are present on its surface, as well as their chemical state, general electronic structure, and density of the electronic states in the material. Because it reveals both the elements that are present and the other elements to which they are linked, XPS is a strong measurement technique. The method can be applied to depth profiling when combined with ion-beam etching or to line profiling of the elemental composition throughout the surface. It is frequently used to investigate chemical reactions in materials in their natural condition as well as those that have undergone cleavage, scraping, heating, exposure to reactive gases or solutions, ultraviolet radiation, or ion implantation. XPS is a type of photoemission spectroscopy in which an X-ray beam is used to irradiate a material in order to produce electron population spectra.

By measuring the kinetic energy and the quantity of expelled electrons, chemical states can be deduced. Although ambient-pressure XPS, in which materials are evaluated at pressures of a few tens of millibar, is currently under development, it requires high vacuum (residual gas pressure $p \sim 10^{-6}$ Pa) or ultra-high vacuum ($p < 10^{-7}$ Pa).

Except for hydrogen and helium, all elements are easily detected by XPS when using laboratory X-ray sources. The detection limit is in the parts per thousand range, however long collecting durations and concentration at the top surface can provide parts per million (ppm).

Inorganic substances, metal alloys, semiconductors, polymers, elements, catalysts, glasses, ceramics, paints, papers, inks, woods, plant parts, make-up, teeth, bones, medical implants, bio-materials, coatings, viscous oils, glues, and many more materials are frequently analysed using XPS. By freezing them in their hydrated state in an ultrapure environment and enabling multiple layers of ice to sublime away before examination, XPS is used to study the hydrated forms of materials like hydrogels and biological samples, which is a little less frequently.

▪ Cyclic Voltammetry:

Cyclic voltammetry is the most widely used technique for acquiring qualitative data and information about electrochemical reactions. It offers a rapid location of redox potentials of the electroactive species. A method for measuring the current response of a redox active solution to a linearly cycled potential sweep between two or more pre-set values is called cyclic voltammetry. It is a valuable technique for quickly obtaining details about the redox processes' thermodynamics, the analyte's energy levels, and the kinetics of electronic-transfer reactions. Cyclic voltammetry utilises a three-electrode setup, consisting of a working electrode, reference electrode, and counter electrode, similar to other methods of voltammetry. The electrolyte solution, a reference solution, and the three electrodes are initially introduced to an electrochemical cell in order to perform cyclic voltammetry.

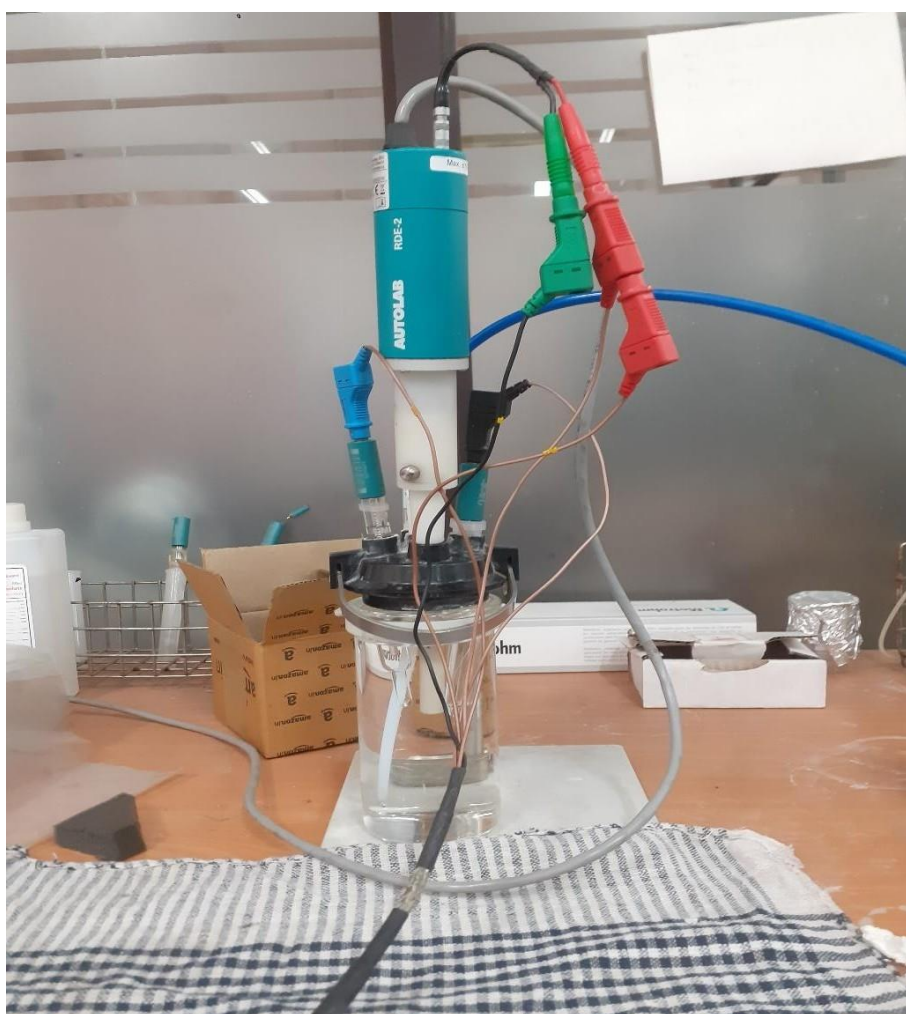


Fig 2.19. Cyclic Voltammetry (GAMRY-autolab) setup

▪ **Operation:**

In cyclic voltammetry the voltage is swept between two values at a fixed rate, however now when the voltage reaches V2, the scan is reversed and the voltage is swept back to V1. A typical voltammogram recorded for a reversible single electrode transfer reaction is shown in below. Again, the solution contains only a single electrochemical reactant. For a reversible electrochemical reaction, the CV record has certain well-defined characteristics.

1. The voltage separation between the current peak is cyclic.
2. The positions of peak voltage do not alter as a function of voltage scan rate.
3. The ratio of the peak currents is equal to one.
4. The peak currents are proportional to the square root of the scan rate.

The CV for cases where the electron transfer is not reversible show considerably different behaviour from their reversible counterparts. By analysing variation of peak position as a function of scan rates, it is possible to gain an estimate for the electron transfer rate constants.

▪ **I-V characterization:**

The techniques for the measurement of the electrical behavior of laminated composites are the two- probe method and four probe methods. The two-probe method is based on the definition of resistance when two electrodes are used to measure the electrical resistance. Figure below shows a specimen, on which a pair of contacts (probe 1 and probe 2) with conductive wires is attached. Two probes are used for the electrical current input, as well as for the voltage measure. The resistance of the segment between the voltage contacts can be calculated through Ohm's law:

$$V = I * R$$

where, V and I are the voltage and current from the voltage and current contacts, respectively.

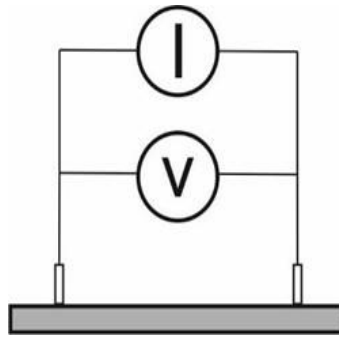
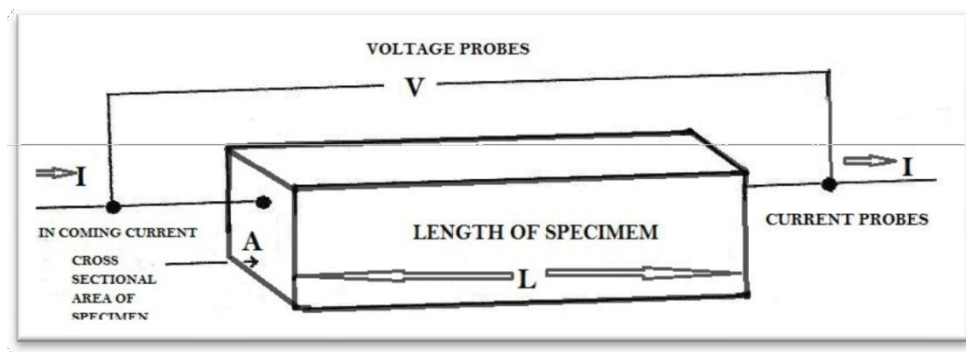


Fig 2.20. Electrical resistivity measurement by two probe method



(a)



(b)

Fig2.21. (a, b) Two probe device used in the project.

• References:

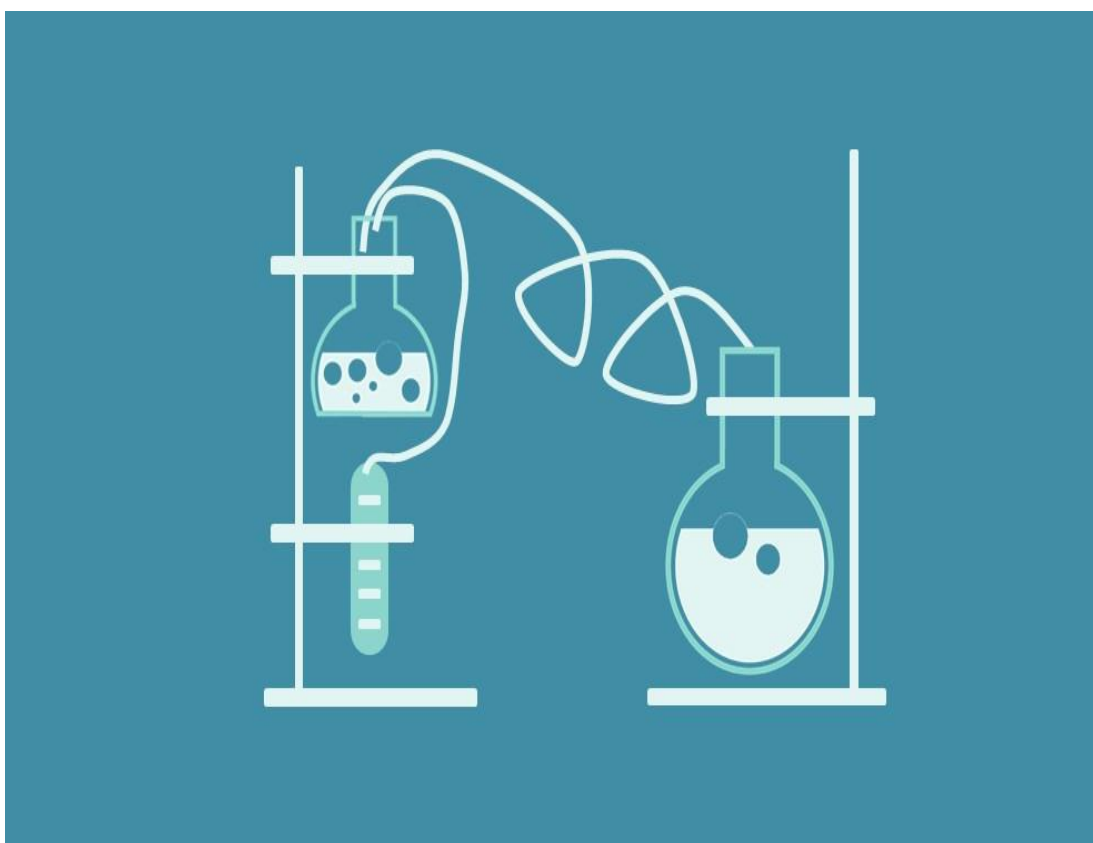
1. Z. Yang, Z. Z. Ye, Z. Xu and B. H. Zhao, "Effect of the Morphology on the Optical Properties of ZnO Nanostructured," *Physica E: Low-Dimensional Systems and Nanostructures*, Vol. 42, No. 2, December 2009, pp. 116- 119. doi: 10.1016/j.physe.2009.09.010.
2. Thermo Nicolet, *Introduction to Fourier Transform Infrared Spectrometry*, © 2001 Thermo Nicolet Corporation.
3. Kortüm, G. *Reflectance Spectroscopy: Principles, Methods, Applications*; Kortüm, G., Ed.; Springer: Heidelberg/Berlin, Germany, 1969.
4. Frei, R.W.; Frodyma, M.M.; Lieu, V.T. Diffuse reflectance spectroscopy. In *Instrumentation for Spectroscopy. Analytical Atomic Absorption and Fluorescence Spectroscopy. Diffuse Reflectance Spectroscopy*; Svehla, G., Ed.; Wilson & Wilson's Comprehensive Analytical Chemistry; Elsevier Scientific Publishing Company: Amsterdam, The Netherlands, 1975; Volume 4, Chapter 3, pp. 263–345.
5. Höpe, A. Diffuse Reflectance and Transmittance. In *Spectrophotometry: Accurate Measurement of Optical Properties of Materials*; Germer, T.A., Zwinkels, J.C., Tsai, B.K., Eds.; Experimental Methods in the Physical Sciences; Academic Press Elsevier Inc.: Amsterdam, The Netherlands, 2014; Volume 46, Chapter 6, pp. 179–219.
6. Lambert, J.H. *Lambert's Photometrie. Photometria Sive De Mensura Et Gradibus Luminis, Colorum et Umbrae* (1760); Anding, E., Ed.; Ostwald's Klassiker der exakten Wissenschaften; Verlag von Wilhelm Engelmann: Leipzig, Germany, 1892; Volume 31.
7. Bouguer, P. *Traité d'optique sur la gradation de la lumiere*; l'Abbé de la Caille, M., Ed.; De l'Imprimerie de H.L. Guerin & L.F. Delatour: Paris, France, 1760.
8. Ångström, K. Ueber die Diffusion der strahlenden Wärme von ebenen Flächen. *Ann. Phys.* 1885, 262, 253–287. [CrossRef]
9. Messerschmitt, J.B. Ueber diffuse Reflexion. *Ann. Phys.* 1888, 270, 867–896. [CrossRef]
10. Seeliger, H. Zur Photometrie zerstreut reflectirender Substanzen. In *Sitzungsberichte der Mathematisch-Physikalischen Classe der k. b. Akademie der Wissenschaften zu München*; Franz, G., Ed.; Verlag der K. Akademie: Munich, Germany, 1888; Volume 18, pp. 201–248.
11. Lommel, E. Die Photometrie der diffusen Zurückwerfung. *Ann. Phys.* 1889, 272, 473–502. [CrossRef]
12. Uljanin, W. Ueber das Lambert'sche Gesetz und die Polarisation der schief emittirten Strahlen. *Ann. Phys.* 1897, 298, 528–542. [CrossRef]
13. Wright, H. Die diffuse Reflexion des Lichtes an matten Oberflächen. *Ann. Phys.* 1900, 306, 17–41. [CrossRef]
14. Pokrowski, G.I. Zur Theorie der diffusen Lichtreflexion. *Z. Phys.* 1924, 30, 66–72. [CrossRef]
15. Schulz, H. Untersuchungen über die Reflexion an teilweise lichtzerstreuenden Flächen. *Z. Phys.* 1925, 31, 496–506. [CrossRef]
16. Harrison, V.G.W. The light-diffusing properties of magnesium oxide. *Proc. Phys. Soc.* 1946, 58, 408–419. [CrossRef]
17. Torrent, J.; Barrón, V. Diffuse Reflectance Spectroscopy. In *Methods of Soil Analysis Part 5–Mineralogical Methods*; Number 5 in the Soil Science Society of America Book

- Series; Ulery, A.L., Drees, L.R., Eds.; Soil Science Society of America Inc.: Madison, WI, USA, 2008; Volume 5, Chapter 13, pp. 367–385.
18. Blake, T.A.; Johnson, T.J.; Tonkyn, R.G.; Forland, B.M.; Myers, T.L.; Brauer, C.S.; Su, Y.F.; Bernacki, B.E.; Hanssen, L.; Gonzalez, G. Methods for quantitative infrared directional-hemispherical and diffuse reflectance measurements using an FTIR and a commercial integrating sphere. *Appl. Opt.* 2018, 57, 432–446. [CrossRef]
 19. Clarke, F.J.J.; Compton, J.A. Correction Methods for Integrating-Sphere Measurement of Hemispherical Reflectance. *Color Res. Appl.* 1986, 11, 253–262. [CrossRef]
 20. Kortüm, G.; Braun, W.; Herzog, G. Prinzip und Meßmethodik der diffusen Reflexionsspektroskopie. *Angew. Chem.* 1963, 75, 653–661. [Cross Ref]
 21. Hanssen, L. Integrating-sphere system and method for absolute measurement of transmittance, reflectance, and absorptance of specular samples. *Appl. Opt.* 2001, 40, 3196–3204. [CrossRef] [PubMed]
 22. Jacquez, J.A.; McKeehan, W.; Huss, J.; Dimitroff, J.M.; Kuppenheim, H.F. An Integrating Sphere for Measuring Diffuse Reflectance in the Near Infrared. *J. Opt. Soc. Am.* 1955, 45, 781–785. [Cross Ref]
 23. Goebel, D.G.; Caldwell, B.P.; Hammond, H.K. Use of an Auxiliary Sphere with a Spectro reflectometer to Obtain Absolute Reflectance. *J. Opt. Soc. Am.* 1966, 56, 783–788. [CrossRef]
 24. Adams, J.B. Interpretation of Visible and Near-Infrared Diffuse Reflectance Spectra of Pyroxenes and other Rock-Forming Minerals. In *Infrared and Raman Spectroscopy of Lunar and Terrestrial Minerals*; Karr, C., Ed.; Academic Press Inc.: London, UK, 1975; Chapter 4, pp. 91–115.
 25. Photoluminescence Spectroscopy, Physics U600, Adv Lab I – Physics of Waves and Optics – Summer 2004, D. Heiman, North eastern University, 6/1/2004.
 26. J. Reichman, *Handbook of Optical Filters for Fluorescence Microscopy* (Chroma Technology, Brattleboro, 2010).
 27. C. Ronda, *Luminescence from Theory to Applications* (Wiley-VCH, New York, 2008).
 28. I. Parreu, J.J. Carvajal, X. Solans, F. Díaz, M. Aguiló, *Chem. Mater.* 18, 221 (2006).
 29. Y. Hong, J. W. Y. Lam, and B. Z. Tang, *Chem. Commun.*, 2009, 4332.
 30. Photoluminescence Spectroscopy and its Applications, Ruquan Ye, Andrew R. Barron, OpenStaxCNX module: m38357.
 31. M. Anpo, M. Kondo, S. Coluccia, C. Louis, and M. Che, *J. Am. Chem. Soc.*, 1989, 111, 8791.

Chapter-3

Different Synthesis

Techniques



• **Synthesis Techniques:**

Carbonaceous materials such as graphite, graphene, graphene oxide (GO) and reduced graphene oxide (rGO) have a huge interest in new days industry due to their huge range of different applications in different fields of new technology. These materials are having a rich synthesis history of 150 years. With time the synthesis procedure indulging these materials upgraded itself with bulk production and less hazards. There are multiple synthesis processes to produce graphene oxide (GO) from graphite and then reducing it in to rGO. The past has revealed three main techniques for producing graphene oxides: Staudenmaier's (ST) method, which employs a chlorate oxidant in fuming nitric acid; Hofmann's (HO) version, which uses chlorate in sulfuric acid; and Hummers' (HU) technique which employs a permanganate oxidant. ST method and Hummer's method for synthesis of GO are being discussed in this chapter. The rGO can be produced using this already produced GO by hydrothermal process. Brief description of hydrothermal process is also included in this chapter.

Numerous methods have been developed to fabricate Si nanostructures as well using top-down or bottom-up approaches, such as vapor-liquid-solid (VLS) growth, reactive ion etching (RIE), electrochemical etching, solution-liquid-solid (SLS) process, chemical vapor deposition (CVD), molecular beam epitaxy (MBE) or metal-assisted chemical etching, all of which aim to control various parameters of the Si structures. In this chapter we have discussed about two techniques namely, Chemical Etching and VLS process, in details.

▪ **GO synthesis using Staudenmaier's (ST) method:**

Materials: Graphite, Sulphuric acid (H_2SO_4), Nitric acid (HNO_3) and Potassium chlorate (KClO_3).

Process:

1. At first sulphuric acid and nitric acid are added to a reaction flask containing magnetic bit for stirring.
2. Then the solution is cooled at 0°C for 10 to 15 minutes.
3. After cooling the solution, graphite is added to the mixture under vigorous stirring so that it cannot agglomerate itself and disperse homogenously into the acid mixture.

4. Once the graphite is dispersed into the acid mixture, potassium chlorate is poured into the solution very carefully and slowly at 0°C to avoid sudden increase in temperature and production of chlorine dioxide which is very much explosive at high concentration.
5. After the potassium chlorate has completely dissolved, the reaction flask is loosely sealed to enable gas evolution, and the mixture is rapidly agitated for a lengthy amount of time (80 to 100 hours) at room temperature.
6. The mixture is placed into ultra-pure water and then filtered when the reaction was finished.
7. To remove sulphate ions, the GO is then redistributed and repeatedly rinsed with HCl solutions.
8. Finally, the GO is cleaned with ultra-pure water until the filtrate's pH is neutral. Before usage, the slurry GO is then dried for five to seven days at 50°C in a vacuum oven.

▪ **GO synthesis using Hummers' (HU) method:**

Materials: Graphite, concentrated sulphuric acid (H_2SO_4), Sodium Nitrate (NaNO_3), Hydrogen peroxide (H_2O_2) and Potassium Permanganate (KMnO_4).

Process:

1. To start the reaction, at first graphite is stirred with H_2SO_4 in a reaction flask for few minutes at 0°C so that it can be dispersed into the solution.
2. After that sodium nitrate is added to the mixture in some portions and kept it for 1 hour under stirring.
3. Then potassium permanganate is poured slowly into the solution at 35°C which eventually rise the temperature to 90°C . The temperature is maintained as the same for next 1 hour.
4. Extra water is added to the solution followed by pouring of H_2O_2 .
5. Once the solution ends its reaction, it is washed multiple times with warm water.
6. To separate the solid GO, the mixture was then centrifuged multiple times and the solid GO is collected.
7. The solid GO then dried in vacuum oven for some days before use.

▪ **Hydrothermal Process:**

The hydrothermal synthesis was defined in the literature [1] as a process in a closed system, in which chemical reactions take place exclusively in a water solvent at increased temperatures, at a pressure that is higher than atmospheric pressure ($P > 101,325 \text{ Pa}$). This definition is often modified by scholars, e.g., Byrappa and Yoshimura [2] proposed a definition of the “hydrothermal reaction” as any heterogeneous chemical reaction in the presence of a solvent (whether aqueous or non-aqueous) above the room temperature and at a pressure greater than 1 ATM in a closed system. For the purposes of this review, we assume that the “hydrothermal synthesis” is a process occurring in an aqueous environment (where $\text{mH}_2\text{O} > 50\%$), with the pressure equal to or higher than atmospheric pressure. In hydrothermal processes, reaction products are mainly oxides and salts due to the properties of water as a solvent.

Solvothermal synthesis is a method for preparing a variety of materials such as metals, semiconductors, ceramics, and polymers. The process involves the use of a solvent under moderate to high pressure (typically between 1 ATM and 10,000 ATM) and temperature (typically between 100°C and 1000°C) that facilitates the interaction of precursors during synthesis. If water is used as the solvent, the method is called ‘hydrothermal synthesis’. The synthesis under hydrothermal conditions is usually performed below the supercritical temperature of water (374°C). The process can be used to prepare structures including various morphologies including thin films, bulk powders, single crystals, and nanocrystals.

In addition, the morphology (sphere (3D), rod (2D), or wire (1D)) of the crystals formed is controlled by manipulating the solvent supersaturation, chemical of interest concentration, and kinetic control. The method can be used to prepare thermodynamically stable and metastable states including novel materials that cannot be easily formed from other synthetic routes [3].

• **ADVANTAGES OF THE HYDROTHERMAL METHOD:**

- i) Possible to precipitate powders directly from solution
- ii) Ability to synthesize crystals of substances which are unstable near melting point
- iii) Suitable when it is difficult to dissolve precursors at room or lower temperatures
- iv) Can be hybridised with other processes like microwave, ultrasound etc [10].

- **DISADVANTAGES OF THE HYDROTHERMAL METHOD:**

- i) High cost of equipment e.g., the need of expensive autoclaves.
- ii) II. Inability to observe the crystals in the process of their growth [11, 12].

- **REDUCTION OF GO TO rGO:**

The prepared GO can be more reduced to remove its most of the edge linked functionalization groups to form a pure layer of graphene oxide with less groups (eventually called as reduced graphene oxide) using hydrothermal method. As hydrothermal or solvothermal technique possess constant temperature and pressure, thus, effectively the reduction can be done easily in less time. The reduction can include doping as well which is an extra hand of using hydrothermal process. Different amide groups, sulphur groups etc. can be used as reduction agent. Nitrogen, sulphur, boron etc. can be doped by tuning the components of the reaction.

In this project work, modified Hummer's method is being used for producing good quality of graphene oxide (GO) and rGO is synthesised using hydrothermal process.

- **Metal Assisted Chemical Etching Method:**

Among the various methods, metal-assisted chemical etching has attracted increasing attention in recent years for several reasons –

1. Metal-assisted Chemical etching is a low-cost and easy approach for manufacturing a variety of Si nanostructures with the ability to regulate a number of factors (e.g., cross-sectional shape, diameter, length, orientation, doping type, and doping level) [23, 24, 25, 26]. Almost all processes may be completed without the need of pricey equipment in a chemical lab.
2. Metal-assisted chemical etching enables control of the orientation of Si nanostructures (e.g., nanowire, pore) relative to the substrate.
3. VLS-based techniques can only develop wires with circular cross-sections, but metal-assisted chemical etching is far more versatile and can

be utilized to create structures with a greater surface-to-volume ratio. [14, 17].

4. The crystalline quality of Si nanowires produced from single crystalline substrates using metal-assisted etching is typically good. Despite the fact that their surfaces are generally rougher than those of nanowires grown by VLS, the nanowires lack the apparent crystallographic flaws caused by solution-based etching, whereas dry etching (e.g., RIE) tends to create faults in an area near to the etched Si surfaces. [18].
5. The size of features produced via metal-assisted chemical etching has no evident limit. The technique may be used to create straight and well-defined holes or wires with sizes ranging from 5 nm to 1 μm .

As a result, metal-assisted chemical etching has grown in importance during the previous decade. Various Si or Si/Ge nanostructures have been created using this approach.

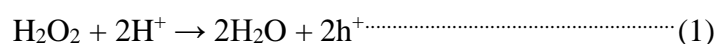
- **Deposition of Noble Metal:**

In metal-assisted chemical etching, Ag, Au, are the most frequently used noble metals. They can be deposited on the Si substrate via various methods, which include thermal evaporation, sputtering, electron beam (e-beam) evaporation, electroless deposition-focused-ion- beam (FIB) deposition or spin coating of noble metal particles. Electroless deposition is a simple process for depositing noble metals that is typically used when the morphology of the resulting etched structures is not a strict requirement. Noble metals may be electrolessly deposited onto a Si substrate using a variety of plating solutions containing noble metal ions. The plating is a typical galvanic process (reported by Ogata et al. [34]). In a brief, the ions of the noble metal inject holes into the Si substrate's valence band. Metal ions are reduced and form nuclei on the surface of Si during this process. On the other hands, holes injected into the Si substrate oxidize the Si to SiO_2 . The plating solutions composed of HF and noble metal ions. Hence the plating under such solutions occurs simultaneously, with the chemical etching process. If we have immersed a Si substrate in a solution containing HF and M^+ ($\text{M} = \text{Ag}$ or Au) for a considerable span of time (e.g., longer than 30 seconds) then the dendrite

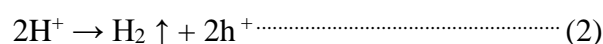
structures of the deposited metal forms. Because the electrochemical potential of Ag^+/Ag was more positive than the Fermi energy of the Si substrate, a galvanic cell was created by submerging a Si substrate in the HF/AgNO_3 solution. Ag^+ was used to introduce holes into the valence band of Si. The Ag^+ was reduced to elemental Ag forming nuclei. The Ag nuclei developed into large particles as the etching time increased. Simultaneously, holes fed into Si's valence band through Ag particles aided local Si atom oxidation and disintegration beneath the Ag particles. The particles sunk into the Si substrate due to the breakdown of Si atoms beneath the Ag particles. The charge transfer took place at the etching front, the interface between Si and the deposited Ag particle, with the etching front being the preferred location. As a result, no new Ag nuclei formed on the etched pores' sidewalls, and the Ag^+ was preferentially reduced, resulting in Ag particles developing at the bottom of the etched pores. Accordingly, the Ag nuclei grew into dendrite structures. By varying the concentration of AgNO_3 and HF , the diameter of the Si nanowires could be roughly tuned.

- **Reactions:**

A Si substrate in contact with an isolated noble metal particle is etched in an etchant consisting of HF and H_2O_2 . It is investigated and reported that the chemical or electrochemical reactions occur preferentially near the noble metal. It is studied from various literatures that the H_2O_2 is reduced at the cathode (metal):



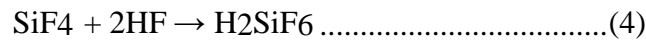
Meanwhile, Li and Bohn [19] and Harade et al. [15] claimed that, in addition to reaction (1), another cathode reaction was the reduction of protons into hydrogen:



Chartier et al. [20], on the other hand, ascribed the gas development during etching to an anode reaction. The conclusion of Chartier et al. came from the judgment that H_2O_2 instead of H^+ was the principal reaction agent at cathodic sites, because in a H_2O_2 free HF solution, no etching occurred in a Pt-particle-

loaded Si substrate [21]. Meanwhile, the possibility that gas was generated from a decay of H₂O₂ was excluded because gas evolution did not occur on an Ag⁰ particle-loaded Si substrate in solution with high concentration of H₂O₂ in the absence of HF

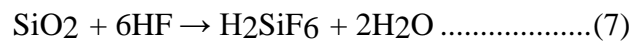
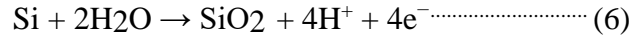
[20]. The Si substrate is oxidized and dissolved at the anode. There have been a variety of models developed for the dissolution of Si (anode reaction), which may be divided into three categories (1) In the tetravalent state, direct dissolution of Si is possible. [19]



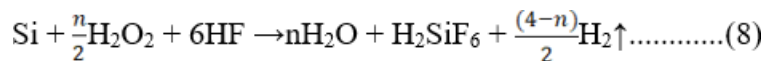
(2) Direct dissolution of Si in divalent state [20]



(3) Si-dioxide formation followed by dissolution of oxide [20, 21]



Chartier et al. [20] proposed a mixed reaction composed of divalent and tetravalent dissolution for the dissolution of Si in metal-assisted chemical etching: The overall reaction is:



- **The Overall Etching Process:**

Based on the various research results, a scenario describing the processes in metal-assisted chemical etching is tentatively suggested here:

1. The noble metal functions as a tiny cathode on which the oxidant is reduced (cathode reaction) due to the noble metal's catalytic activity. The holes generated due to the reduction of the oxidant diffuse through the

noble metal and are injected into the Si substrate that is in contact with the noble metal.

2. The implanted holes oxidise the Si atoms beneath the noble metal, which are then dissolved by HF (anode reaction).
3. Along the contact between Si and the noble metal, the reactant (HF) and by-products disperse. The hole concentration is highest near the Si/metal contact. As a result, HF etches the Si that is in touch with the metal more quicker than a bare Si surface without metal covering.
4. The metal particle sinks straight into the Si substrate and etches the Si substrate, forming a pore. Well-separated noble metal particles usually result in well-defined pores, while continuous films with a few holes lead to well-defined wires with more uniform cross-sectional shapes and spacing. The Si substrate will be etched into an array of Si nanowires with similar cross-sectional shapes and spacing if the metal film includes ordered dispersed pores with uniform diameters and cross-section shapes.

▪ Catalyst Assisted VLS Growth Process:

- Vapor-Liquid-Solid (VLS) mechanism:

Nanowires are the result of anisotropic, 1D crystal growth on a nanoscale. Therefore, the main issue for the nanowire growth is how we can control the 1D growth. On the basis of that, many approaches have been there, namely, metal catalyst assisted vapor-liquid-solid (VLS) mechanism, template-assisted (TA) mechanism, oxide-assisted growth (OAG), dissolution condensation (DC) mechanism etc. The VLS mechanism is the most commonly utilized approach among these because of its simplicity and adaptability in a wide range of semiconductor systems. The VLS mechanism derives its name from the fact that vapor travels through a liquid droplet then became a solid. The VLS mechanism was first proposed by Wagner and Ellis [22] in the mid-1960s is the key mechanism for silicon-wire growth. Their suggested VLS mechanism is based on two observations: that adding specific metal impurities to silicon wires is required for development, and that tiny globules of the impurity are found near the wire's tip during growth.

According to these findings, the globule at the wire tip must be engaged in the development of silicon wires by functioning "either a preferred sink for incoming Si atoms or, maybe more likely, as a catalyst for the chemical process involved." [22]. The mechanism works at high temperature at which the metal catalyst forms a liquid alloy. Occasionally, metal catalyst stayed in solid state in a vapor or liquid environment and the process referred as vapor-solid-solid (VSS) or liquid-solid-solid (LSS) process.

Since the 1970s, VLS mechanism has been used to grow various types of whiskers on the micrometer or millimeter scale. Several groups, notably the Lieber group at Harvard University, the Yang group at the University of California Berkeley, and the Samuelson group at Lund University, utilized this technique to build 1D structures on a nanoscale scale in the 1990s. In a VLS growth, the process can be simply described as following as sketched in Figure 1. The growing species is initially evaporated before diffusing and dissolving into a liquid droplet. The liquid's surface has a high accommodation coefficient, making it an ideal location for deposition. The Saturated growth species in the liquid droplet will diffuse to the interface between the substrate and the liquid, where they will precipitate. After nucleation, precipitation will occur, followed by crystal growth. The substrate and the liquid droplet will be separated by further precipitation or growth, resulting in the formation of nanowires.

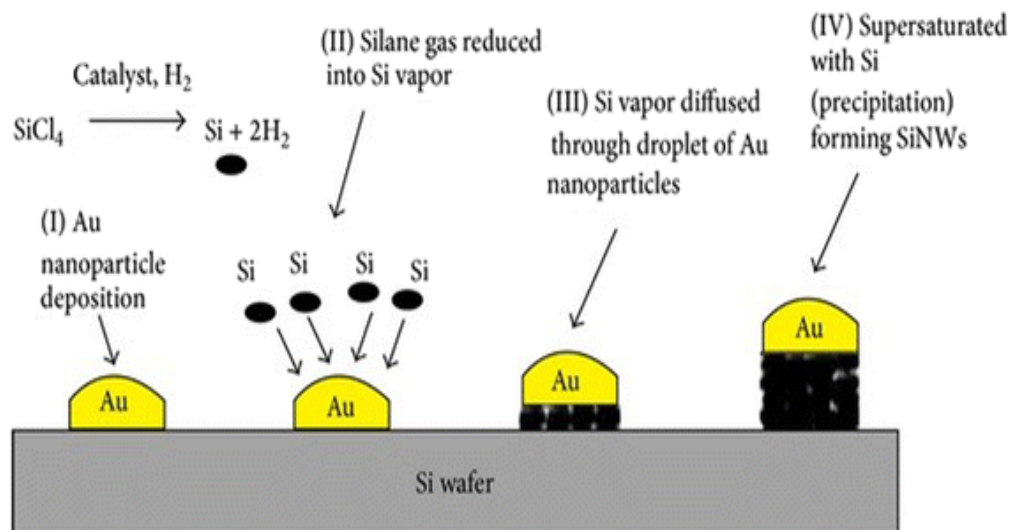


Fig 3.1. Schematic diagram of the VLS growth process

Let's use the formation of silicon nanowires using gold as a catalyst as an example to demonstrate the VLS growth experimental procedure. A thin layer of gold is evaporated on a silicon substrate and annealed at an elevated temperature (above the eutectic point of 363°C of the silicon-gold system). Silicon and gold react during annealing to create a liquid combination that forms a droplet on the silicon substrate surface. When silicon species is evaporated from the source and preferentially absorbed by the surface of the liquid droplet, the liquid droplet will become supersaturated with silicon. Subsequently, the supersaturated silicon will diffuse from the liquid-vapor interface and precipitate at the solid-liquid interface resulting in the growth of silicon. The growth will proceed unidirectionally perpendicular to the solid-liquid interface.

- **Fundamentals of homogeneous nucleation and growth:**

A new phase emerges when the concentration of a solute in a solvent exceeds its equilibrium solubility. A solution with solute exceeding solubility or supersaturation, for example, has a high Gibbs free energy; by isolating the solute from the solution, the total energy of the system is lowered. The decrease of the total Gibbs free energy of a supersaturated solution by creating a solid phase and maintaining an equilibrium concentration in the solution is shown schematically in Figure 2. Both nucleation and growth are fueled by the decrease of Gibbs free energy.

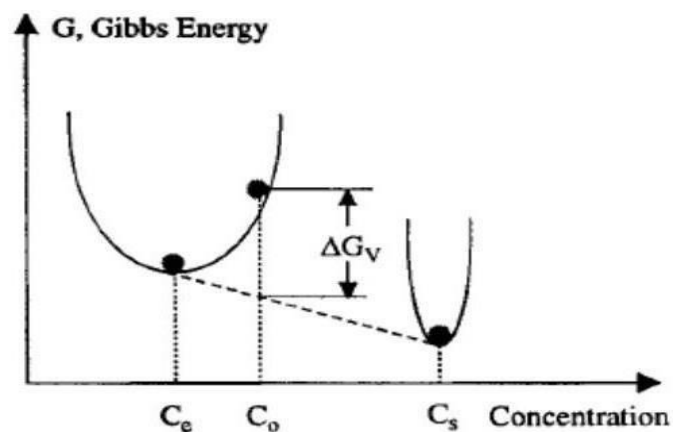


Fig 3.2. Schematic diagram of reduction of the overall Gibbs free energy of a supersaturated solution by forming a solid phase and maintaining an equilibrium concentration in the solution.

The variation in Gibbs free energy per unit volume of the solid phase, G_v , is linked to the solute concentration:

$$\Delta G_v = -\frac{kT}{\omega} \ln\left(\frac{c}{c_0}\right) = -\frac{kT}{\omega} \ln(1 + \sigma)$$

Where C is the concentration of the solute, C_0 is the equilibrium concentration or solubility, k is the Boltzmann constant, T is the temperature, ω is the atomic volume, and supersaturation defined by $(C-C_0)/C_0$. Without supersaturation G_v is zero, and no nucleation would occur. When $C > C_0$, ΔG_v is negative and nucleation occurs spontaneously. Only when the radius of the freshly created nucleus surpasses a certain size, r^* , is it stable. A nucleus that is less than r^* will dissolve into the solution, lowering the overall free energy, whereas a nucleus that is larger than r^* will remain stable and continue to develop. The critical size, r^* , and critical energy ΔG^* are defined as:

$$r^* = -2 \frac{\gamma}{\Delta G_v} \text{ and } \Delta G^* = \frac{16\pi\gamma}{(3\Delta G_v)^2}$$

r^* is the minimal size of a stable spherical nucleus, and ΔG^* is the energy barrier that a nucleation process must overcome. Only when the supersaturation reaches a specific value above the solubility, which corresponds to the energy barrier for the production of nuclei, can nucleation begin. There will be no nucleation, once when the concentration of the growth species rises over the equilibrium concentration. Nucleation, on the other hand, happens when the concentration exceeds the minimal saturation necessary to break the critical energy barrier, and the nucleation rate quickly increases as the concentration rises. Although, without a nucleus, the development process is suspended. When nuclei are formed, they begin to expand at the same time.

Nucleation and growth are inseparable processes above the minimum concentration; nevertheless, they happen at distinct rates.

• References:

1. Henglein, A. Small-particle research-physicochemical properties of extremely small colloidal metal and semiconductor particles. *Chem. Rev.* 1989, 89, 1861–1873.
2. Trindade, T.; O'Brien, P.; Pickett, N.L. Nanocrystalline semiconductors: Synthesis, properties, and perspectives. *Chem. Mater.* 2001, 13, 3843–3858.
3. Kuchibhatla, S.; Karakoti, A.S.; Bera, D.; Seal, S. One dimensional nanostructured materials. *Prog. Mater. Sci.* 2007, 52, 699–913.
4. Bera, D.; Kuiry, S.C.; Seal, S. Synthesis of nanostructured materials using template-assisted electrodeposition. *JOM* 2004, 56, 49–53.
5. P. Wick, A. E. Louw-Gaume, M. Kucki, H. F. Krug, K. Kostarelos, B. Fadeel, K. A. Dawson, A. Salvati, E. Vazquez, L. Ballerini, M. Tretiach, E. Flahaut, L. Gauthier, M. Prato and A. Bianco, Classification framework for graphene-based materials, *Angew. Chem., Int. Ed.*, 2014, 53(30), 7714–7718.
6. M. I. Katsnelson, Graphene: Carbon in two dimensions, *Mater. Today*, 2007, 10(1–2), 20–27.
7. S. Alwarappan and A. Kumar, Graphene-based materials: Science and Technology, Chapter 1: Graphene an introduction, Taylor & Francis group, CRC Press, London, New York 2014.
8. K. Deshmukh and G. M. Joshi, Embedded capacitor applications of graphene oxide reinforced poly(3,4-ethyl)-tetramethacrylate(PEDOT-TMA)composites, *J.Mater.Sci.:Mater. Electron.*, 2015, 26, 5896–5909.
9. G. J. Thangamani, K. Deshmukh, K. K. Sadasivuni, K. Chidambaram, M. B. Ahamed, D. Ponnamm, M. A. A. AlMaadeed and S. K. K. Pasha, Recent advances in electrochemical biosensor and gas sensors based on graphene and carbon nanotubes (CNT) – a review, *Adv. Mater. Lett.*, 2017, 8, 196–205.
10. K. K. Sadasivuni, D. Ponnamm, S. Thomas and Y. Grohens, Evolution from graphite to graphene elastomer composites, *Prog. Polym. Sci.*, 2014, 39(4), 749–780.
11. K. Deshmukh, M. B. Ahamed, S. Sankaran, S. K. K. Pasha, K. K. Sadasivuni, D. Ponnamm and M. A. A. AlMaadeed, Studies on the mechanical, morphological and electrical properties of highly dispersible graphene oxide reinforced polypyrrole and polyvinyl alcohol blend composites, *Mater. Today: Proc.*, 2018, 5, 8744–8752.

12. K. Deshmukh, S. Sankaran, M. B. Ahamed, S. K. K. Pasha, K. K. Sadasivuni, D. Ponnammam and M. A. A. AlMaadeed, Studies on the electrical properties of graphene oxide reinforced poly(4-styrene sulfonic acid) and polyvinyl alcohol blend composites, *Int. J. Nanosci.*, 2018, 17, 1760005–1760013.
13. Gao, Wei. Springer, Cham, 2015. 61-95
14. Chan WC, Maxwell DJ, Gao X, Bailey RE, Han M: Luminescent quantum dots for multiplexed biological detection and imaging. *Curr Opin Biotechnol* 2002, 13(1):40–46.
15. [https://www.nanowerk.com/what_are_quantum_dots.php#:~:text=Quantum%20dots%20\(QDs\)%20are%20nanoscale%20structures%20that%20emit%20light%20when%20excited%20by%20light%20or%20other%20energy%20sources%20and%20are%20used%20in%20a%20wide%20range%20of%20applications%20including%20biology%20and%20medicine.](https://www.nanowerk.com/what_are_quantum_dots.php#:~:text=Quantum%20dots%20(QDs)%20are%20nanoscale%20structures%20that%20emit%20light%20when%20excited%20by%20light%20or%20other%20energy%20sources%20and%20are%20used%20in%20a%20wide%20range%20of%20applications%20including%20biology%20and%20medicine.)
16. Xia C., Zhu S., Feng T., Yang M., Yang B. Evolution and synthesis of carbon dots: From carbon dots to carbonized polymer dots. *Adv. Sci.* 2019;6:1901316. doi: 10.1002/advs.201901316.
17. Namdari P., Negahdari B., Eatemadi A. Synthesis, properties and biomedical applications of carbon-based quantum dots: An updated review. *Biomed. Pharmacother.* 2017;87:209–222. doi: 10.1016/j.biopha.2016.12.108.
18. Sahu S., Behera B., Maiti T.K., Mohapatra S. Simple one-step synthesis of highly luminescent carbon dots from orange juice: Application as excellent bio-imaging agents. *Chem. Commun.* 2012;48:8835–8837. doi: 10.1039/c2cc33796g.
19. Atabaev S. Size-tunable carbon nanoparticles with excitation-independent fluorescent properties. *Mater. Today Proc.* 2017;4:4896–4899. doi: 10.1016/j.matpr.2017.04.092.
20. De B., Karak N. A green and facile approach for the synthesis of water-soluble fluorescent carbon dots from banana juice. *RSC Adv.* 2013;3:8286–8290. doi: 10.1039/c3ra00088e.
21. Zhou M., Zhou Z., Gong A., Zhang Y., Li Q. Synthesis of highly photoluminescent carbon dots via citric acid and Tris for iron(III) ions sensors and bioimaging. *Talanta.* 2015;143:107–113.
22. Zhou J., Shan X., Ma J., Gu Y., Qian Z., Chen J., Feng H. Facile synthesis of P-doped carbon quantum dots with highly efficient photoluminescence. *RSC Adv.* 2014;4:5465–5468. doi: 10.1039/c3ra45294h.
23. Dong Y., Pang H., Yang H.B., Guo C., Shao J., Chi Y., Li C.M., Yu T. Carbon-based dots co-doped with nitrogen and sulfur for high quantum yield and excitation-independent emission. *Angew. Chem. Int. Ed.* 2013;52:7800–7804. doi: 10.1002/anie.201301114.

24. Bourlinos A.B., Trivizas G., Karakassides M.A., Baikousi M., Kouloumpis A., Gournis D., Bakandritsos A., Hola K., Kozak O., Zboril R., et al. Green and simple route toward boron doped carbon dots with significantly enhanced non-linear optical properties. *Carbon*. 2015;83:173–179. doi: 10.1016/j.carbon.2014.11.032.
25. Barman M.K., Jana B., Bhattacharyya S., Patra A. Photophysical Properties of Doped Carbon Dots (N, P, and B) and Their Influence on Electron/Hole Transfer in Carbon Dots—Nickel (II) Phthalocyanine Conjugates. *J. Phys. Chem. C*. 2014;118:20034–20041. doi: 10.1021/jp507080c.
26. Xu Q., Pu P., Zhao J., Dong C., Gao C., Chen Y., Chen J., Liu Y., Zhou H. Preparation of highly photoluminescent sulfur-doped carbon dots for Fe(III) detection. *J. Mater. Chem. A*. 2015;3:542–546. doi: 10.1039/C4TA05483K.
27. Zhang J., Zhao X., Xian M., Dong C., Shuang S. Folic acid-conjugated green luminescent carbon dots as a nanoprobe for identifying folate receptor-positive cancer cells. *Talanta*. 2018;183:39–47. doi: 10.1016/j.talanta.2018.02.009.
28. S. Tajik, Z. Dourandish, K. Zhang, H. Beitollahi, O. V. Le, H. W. Jang and M. Shokouhimehr, Carbon and graphene quantum dots: a review on syntheses, characterization, biological and sensing applications for neurotransmitter determination, *RSC Adv.*, 2020, 10, 15406–15429.
29. Nitrogen-doped graphene and graphene quantum dots: A review on synthesis and applications in energy, sensors and environment
Manpreet Kaur, Manmeet Kaur, Virender K.Sharma
30. Pan, Dengyu; Zhang, Jingchun; Li, Zhen; Wu, Minghong (2010). "Hydrothermal Route for Cutting Graphene Sheets into Blue-Luminescent Graphene Quantum Dots". *Advanced Materials*. 22 (6): 734–738. doi:10.1002/adma.200902825
31. Wang, Shujun; Cole, Ivan S.; Zhao, Dongyuan; Li, Qin (2016). "The dual roles of functional groups in the photoluminescence of graphene quantum dots". *Nanoscale*. 8 (14): 7449–7458. Bibcode:2016Nanos. 8.7449W. doi:10.1039/C5NR07042B. hdl:10072/142465. PMID 26731007.
32. Wu, Zhu Lian; Gao, Ming Xuan; Wang, Ting Ting; Wan, Xiao Yan; Zheng, Lin Ling; Huang, Cheng Zhi (2014). "A general quantitative pH sensor developed with dicyandiamide N-doped high quantum yield graphene quantum dots". *Nanoscale*. 6 (7): 3868–3874. Bibcode:2014Nanos...6.3868W. doi:10.1039/C3NR06353D. PMID 24589665.

33. Ritter, Kyle A; Lyding, Joseph W (2009). "The influence of edge structure on the electronic properties of graphene quantum dots and nanoribbons". *Nature Materials*. 8 (3): 235–42. Bibcode:2009NatMa...8..235R. doi:10.1038/nmat2378. PMID 19219032
34. Wimmenauer, Christian; Scheller, Julianne; Fasbender, Stefan; Heinzl, Thomas (2019). "Single-particle energy – and optical absorption – spectra of multilayer graphene quantum dots". *Superlattices and Microstructures*. 132: 106171. doi:10.1016/j.spmi.2019.106171.
35. M. K. Kumawat, M. Thakur, R. B. Gurung and R. Srivastava, Graphene quantum dots from mangifera indica: Application in near-infrared bioimaging and intracellular nano-thermometry, *ACS Sustainable Chem. Eng.*, 2017, 5(2), 1382–1392.
36. X. Liu, W. Na, Z. Liu, X. Chen and X. Su, Fluorescence turn-on probe based on polypyrrole/graphene quantum composites for selective and sensitive detection of paracetamol and ascorbic acid, *Biosens. Bioelectron.*, 2017, 98, 222–226.
37. Y. H. Li, L. Zhang, J. Huang, R. L. Liang and J. D. Qiu, Fluorescent graphene quantum dots with a boronic acid appended bipyridinium salt to sense monosaccharides in aqueous solution, *Chem. Commun.*, 2013, 49(45), 5180–5182.
38. T.-F. Yeh, C.-Y. Teng, S.-J. Chen and H. Teng, Nitrogen-doped Graphene Oxide Quantum Dots as Photocatalysts for Overall Water-Splitting Under Visible Light Illumination, *Adv. Mater.*, 2014, 26, 3297–3303.
39. <https://www.rfwireless-world.com/Terminology/Advantages-and-Disadvantages-of-Quantum-Dots.html>
40. L. Li, G. Wu, G. Yang, J. Peng, J. Zhao, J.-J. Zhu Focusing on luminescent graphene quantum dots: current status and future perspectives *Nanoscale*, 5 (2013), pp. 4015-4039
41. L. Tang, R. Ji, X. Li, G. Bai, C.P. Liu, J. Hao, J. Lin, H. Jiang, K.S. Teng, Z. Yang, S.P. Lau Deep ultraviolet to near-infrared emission and photoresponse in layered N-doped graphene quantum dots *ACS Nano*, 6 (2014), pp. 6312-6320
42. T. Gao, X. Wang, L.-Y. Yang, H. He, X.-X. Ba, J. Zhao, F.-L. Jiang, Y. Liu Red, yellow, and blue luminescence by graphene quantum dots: syntheses, mechanism, and cellular imaging *ACS Appl. Mater. Interfaces*, 29 (2017), pp. 24846-24856
43. Y. Dong, J. Shao, C. Chen, H. Li, R. Wang, Y. Chi, X. Lin, G. Chen Blue luminescent graphene quantum dots and graphene oxide prepared by tuning the carbonization degree of citric acid *Carbon*, 12 (2012), pp. 4738-474

Chapter-4

Literature review



The fascinating features of the graphene-based materials, such as highly adjustable surface area, exceptional electrical conductivity, strong chemical stability, and great mechanical behaviour, make them potential for use in supercapacitors and other energy storage devices. Based on their macrostructural complexity, such as zero-dimensional (0D) (such as free-standing graphene dots and particles), one-dimensional (1D) (such as fiber-type and yarn-type structures), two-dimensional (2D) (such as graphene and graphene-based nanocomposite films), and three-dimensional (3D), this review summarises recent developments on graphene-based materials for supercapacitor electrodes (e.g. graphene foam and hydrogel-based nanocomposites). The rationalisation of their structures at various scales and dimensions, the development of efficient and affordable synthesis methods, the design and architectonics of graphene-based materials, as well as the clarification of their electrochemical performance, are all the subjects of extensive and ongoing research. Future research should concentrate on the overall device performance in energy storage devices and large-scale low-cost processes for the applications that are promising in portable and wearable electronic, transport, electrical, and hybrid vehicles.

- **Graphite, graphene oxide and rGO based supercapacitor:**

The electrical and thermal conductivities of graphite, a well-known natural mineral, are 1000 times higher in the in-plane direction than they are in the out-of-plane direction. Graphite is extremely anisotropic in both structure and functional behaviour. Similar to this, due to the various sorts of bonding in the two directions, graphite's in-plane strength and modulus are significantly higher than those of the out-of-plane. Graphite is thus one of the most commonly utilised materials in many structural, functional, chemical, and environmental applications. Various processes are employed to produce graphite of varying quality on a big scale. Applications for energy storage also employ this substance. Utilizing graphite as electrodes, Mitra et al. created solid-state electrochemical capacitors with extended cycle lives and rapid response times. The computed specific capacitances of these capacitors ranged from 0.74 to 0.98 mF cm⁻².

Chemically modified graphene (CMG) was first used as an electrode material by Ruoff et al. They discovered that the aqueous and organic electrolytes, respectively, could achieve the specific capacitances of 135 and 99 F g⁻¹. Ajayan et al. described a two-step process that involves deoxygenation with NaBH₄ and dehydration with strong sulfuric acid to create a

highly reduced GO. To retain performance during the demanding oxidation and reduction process, the comb-like linked sheet structure needs to be shielded. Graphene was created by Zhu et al. using sugar as a reduction agent. Zhang and colleagues used ascorbic acid. In addition, it was suggested that reduced graphene oxides may be produced using "green" materials including melatonin, vitamin C, bovine serum albumin, green tea polyphenols, and even bacterial respiration (rGO). One particular flexible and affordable approach for producing rGO is the one-step hydrothermal method. Shi et al. reported that the one-step hydrothermal method reduced the amount of GO. With aqueous electrolyte, the rGO exhibits a high conductance of $5 \times 10^3 \text{ S cm}^{-1}$ and a high specific capacitance of 175 F g^{-1} . Even yet, it can be difficult to totally remove GO because some of the surface groups that contain oxygen can be tricky to get rid of.

Wang et al. developed a flexible graphene paper incorporating with small amounts of carbon black nano-particles as spacers between graphene sheets, which provide an open structure for charge storage and ion diffusion channels, therefore resulting in a significant improvement in electrochemical performance (*i.e.*, a specific capacitance of 138 F g^{-1} in aqueous electrolyte at the scan rate of 10 mV s^{-1} and only 3.85% capacitance being lost after 2000 cycles at the current of 10 A g^{-1}). Li et al. reported a flexible graphene film paper using CNTs as a spacer to prevent the inter sheet restacking. This multilayered graphene structures enable the hybrid electrodes to have a high specific capacitance of 140 F g^{-1} at the current density of 0.1 A g^{-1} in $1 \text{ M H}_2\text{SO}_4$ solution. Si et al. employed the Pt as spacers to separate the graphene sheets, and they found that the Pt-separated graphene sheets exhibited a significantly enlarged capacitance of 269 F g^{-1} , compared to normal graphene with a capacitance of 14 F g^{-1} . Peak et al. modified graphene sheets with SnO_2 particles, which were mixed in between the inter-sheets of graphene layers. Due to the expended inner space among graphene sheets, the capacitance is greatly improved, leading to an enhanced energy storage ability.

With the restacking of graphene sheets being tackled at least partially, the gravimetric specific capacitance of graphene films with carbon-based spacers or metal nanoparticles is improved up to $\sim 300 \text{ F g}^{-1}$. In order to further increase the energy density, pseudocapacitive materials with large capacitances were employed as spacers. They are several transition metal oxides and hydroxides, such as RuO_2 , Fe_3O_4 , CuO , Ni(OH)_2 , MnO_2 , Co_3O_4 , and conductive polymers such as polyanilines (PANI), polypyrrole (PPy) and polythiophene (PT).

Wang et al. reported graphene sheets intercalated with single crystalline hexagonal Co(OH)_2 nanoplates, which can provide the desired void space between graphene layers and

contribute to the pseudocapacitance. This hybrid-type electrode material demonstrates an impressive specific capacitance of 1335 F g^{-1} at the current density of 2.8 A g^{-1} . Li et al. further developed a bendable film electrode material, where Ni(OH)_2 nanoplates are intercalated between the densely stacked graphene sheets (GNiF) (see [Fig. 5](#)). The 3D expressway-like electrode exhibits a capacitance performance of 537 F g^{-1} and a high volumetric capacitance of 655 F cm^{-3} . MnO_2 as a common pseudocapacitive material is also used to space graphene layers, which offers the environmental compatibility and low cost. Choi. et al. developed a film-type electrode by hybridizing graphene with MnO_2 by a filtration method. The resultant nanocomposite film shows a specific capacitance of 389 F g^{-1} in 1 M NaSO_4 and the capacitance retention of 95% after 1000 cycles. Yang et al. constructed an asymmetric configuration with Fe_2O_3 and MnO_2 nanoparticles being incorporated into macroporous graphene film electrodes. They found a working potential window up to 1.8 V and an energy density of 41.7 W h kg^{-1} together with a power density (13.5 kW kg^{-1}). The high energy and power density could be maintained for over 5000 cycles, even at a high current density of 16.9 A g^{-1} .

Reference:

1. J.R. Miller, P. Simon
Electrochemical capacitors for energy management
Science, 321 (2008), pp. 651-652
2. P. Simon, Y. Gogotsi
Materials for electrochemical capacitors.
Nat Mater, 7 (2008), pp. 845-854
3. W. Shi, J. Zhu, D.H. Sim, H.H. Tay, Z. Lu, X. Zhang, et al.
Achieving high specific charge capacitances in Fe₃O₄/reduced graphene oxide nanocomposites
J Mater Chem, 21 (2011), pp. 3422-3427
4. L.L. Zhang, R. Zhou, X.S. Zhao
Graphene-based materials as supercapacitor electrode
J Mater Chem, 20 (2010), pp. 5983-5992
5. S. Mitra, S. Sampath; Electrochemical capacitors based on exfoliated graphite electrodes batteries, fuel cells, and energy conversion. Electrochem Solid-State Lett, 7 (2004), pp. A264-A2685.
6. M.D. Stoller, S. Park, Y. Zhu, J. An, R.S. Ruoff
Graphene-based ultracapacitors
Nano Lett, 8 (2008), pp. 3498-3502
7. W. Gao, L.B. Alemany, L.J. Ci, P.M. Ajayan
New insights into the structure and reduction of graphite oxide
Nat Chem, 1 (2009), pp. 403-408
8. C. Zhu, S. Guo, Y. Fang, S. Dong
Reducing sugar: new functional molecules or the green synthesis of graphene nanosheets
ACS Nano, 4 (2010), pp. 429-437
9. J. Zhang, H. Yang, G. Shen, P. Cheng, J. Zhang, S. Guo
Reduction of graphene oxide via L-ascorbic acid
Chem Comm, 46 (2010), pp. 1112-1114
10. M.J. Merino, L. Guardia, J.I. Paredes, S.V. Rodil, P.S. Fernandez, A.M. Alonso, *et al.*
Vitamin C is an ideal substitute for hydrazine in the reduction of graphene oxide suspensions

J Phys Chem C, 114 (2010), pp. 6426-6432

11. J. Gao, F. Liu, Y. Liu, N. Ma, Z. Wang, X. Zhang
Environment-friendly method to produce graphene that employs vitamin C and amino acid
Chem Mater, 22 (2010), pp. 2213-2218
12. O. Akhavan, E. Ghaderi, S. Aghayee, Y. Fereydooni, A. Talebi
The use of a glucose-reduced graphene oxide suspension for photothermal cancer therapy
J Mater Chem, 22 (2012), pp. 13773-13781
13. J. Liu, S. Fu, B. Yuan, Y. Li, Z. Deng
Toward a universal “adhesive nanosheet” for the assembly of multiple nanoparticles based on a protein induced reduction/decoration of graphene oxide
J Am Chem Soc, 132 (2010), pp. 7279-7281
14. O. Akhavan, M. Kalaei, Z.S. Alavi, S.M.A. Ghiasi, A. Esfandiari
Increasing the antioxidant activity of green tea polyphenols in the presence of iron for the reduction of graphene oxide
Carbon, 50 (2012), pp. 3015-3025
15. O. Akhavan, E. Ghaderi
Escherichia coli bacteria reduce graphene oxide to bactericidal graphene in a self-limiting manner
Carbon, 50 (2012), pp. 1853-1860
16. E.C. Salas, Z. Sun, A. Luttge, J.M. Tour
Reduction of graphene oxide *via* bacterial respiration
ACS Nano, 4 (2010), pp. 4852-4856
17. L.J. Cote, R.C. Silva, J. Huang
Flash reduction and patterning of graphite oxide and its polymer composite
J Am Chem Soc, 131 (2009), pp. 11027-11032
18. Y. Zhou, Q. Bao, L. Ai, L. Tang, Y. Zhong, K.P. Loh
Hydrothermal dehydration for the “green” reduction of exfoliated graphene oxide to graphene and demonstration of tunable optical limiting properties
Chem Mater, 21 (2009), pp. 2950-2956

19. K. Ai, Y. Liu, L. Lu, X. Cheng, L. Huo
A novel strategy for making soluble reduced graphene oxide sheets cheaply by adopting an endogenous reducing agent
J Mater Chem, 21 (2011), pp. 3365-3370
20. C. Xu, X. Wang, J. Zhu
Graphene metal particle nanocomposites
J Phys Chem C, 112 (2008), pp. 19841-19845
21. O. Akhavan, E. Ghaderi
Photocatalytic reduction of graphene oxide nanosheets on TiO₂ thin film for photoinactivation of bacteria in solar light irradiation
J Phys Chem C, 113 (2009), pp. 20214-20220
22. G. Williams, B. Seger, P.V. Kamat
TiO₂-graphene nanocomposites UV assisted photocatalytic reduction of graphene oxide
ACS Nano, 2 (2008), pp. 1487-1491
23. O. Akhavan, M. Abdolahad, A. Esfandiar, M. Mohataashamifar
Photodegradation of graphene oxide sheets by TiO₂ nanoparticles after a photocatalytic reduction
J Phys Chem C, 114 (2010), pp. 12955-12959
24. O. Akhavan
Graphene nanomesh by ZnO nanorod photocatalysts
ACS Nano, 4 (2010), pp. 4174-4180
25. O. Akhavan, M. Choobtashani, E. Ghaderi
Protein degradation and RNA efflux of viruses photocatalyzed by graphene-tungsten oxide composite under visible light irradiation
J Phys Chem C, 116 (2012), pp. 9653-9965
26. H.R. Byon, S.W. Lee, S. Chen, P.T. Hammond, Y. Shao-Horn
Thin films of carbon nanotubes and chemically reduced graphenes for electrochemical micro-capacitors
Carbon, 49 (2011), pp. 457-467

Chapter-5

Experiments:

Synthesis of Samples



- **Synthesis of Graphene Oxide (GO) using modified Hummer's method:**

- **Materials:**

Graphite flakes (7–10 μm grain size, 99% purity) from Alfa Aesar; sodium nitrate (NaNO_3), 99% purity), sulfuric acid (H_2SO_4 , 98% by weight, G.R.), potassium permanganate (KMnO_4 , 99% purity), hydrochloric acid (HCL), hydrogen peroxide (H_2O_2 , 30% by weight, A.R.) from Merck were used for synthesis. Deionized (DI) water was taken from a Direct-Q Millipore deionized (18 Ω at 25°C) [6].

- **Sample Preparation:**

1. Graphene Oxide (GO) was produced through oxidation and exfoliation of graphite flakes using modified Hummer's method. To start the process, at first 3 gm. of graphite powder and 3 gm. of sodium nitrate were mixed well and taken in a 500 ml beaker containing 180 ml concentrated sulphuric acid. This solution was undergone vigorous stirring for 2 hours [3].
2. Then, 10 gm. of potassium permanganate were included into the black solution very slowly for 30 minutes keeping the temperature under 15° C. Again, the solution was kept under vigorous stirring for next 24 hours.
3. Then, to achieve a colour change from black to golden yellow, 200 mL DI and 10 mL 30% H_2O_2 were gradually added to the solution while maintaining a temperature of roughly 40°C. After that, the mixture was allowed to settle and cool to room temperature [4].
4. The bottom portion of the clear supernatant was decanted, centrifuged twice at 12000 rpm for 15 minutes, washed with 5% hydrochloric acid once, and the resultant supernatant was removed.
5. Following a DI wash, the bottom portion (brown in colour) was centrifuged for 10 minutes at 12000 rpm to create three layers in the centrifuged tube. The middle light brown colour solution was extracted after the upper colourless portion was first removed.
6. The bottom part of the solution having GO and excess graphite, was centrifuged subsequently 5 times and each time the middle portion containing GO was extracted and the lower part was removed [5].

7. To obtain newly prepared GO, the light brown suspension was dried in a vacuum oven for 24 hours at 48°C.

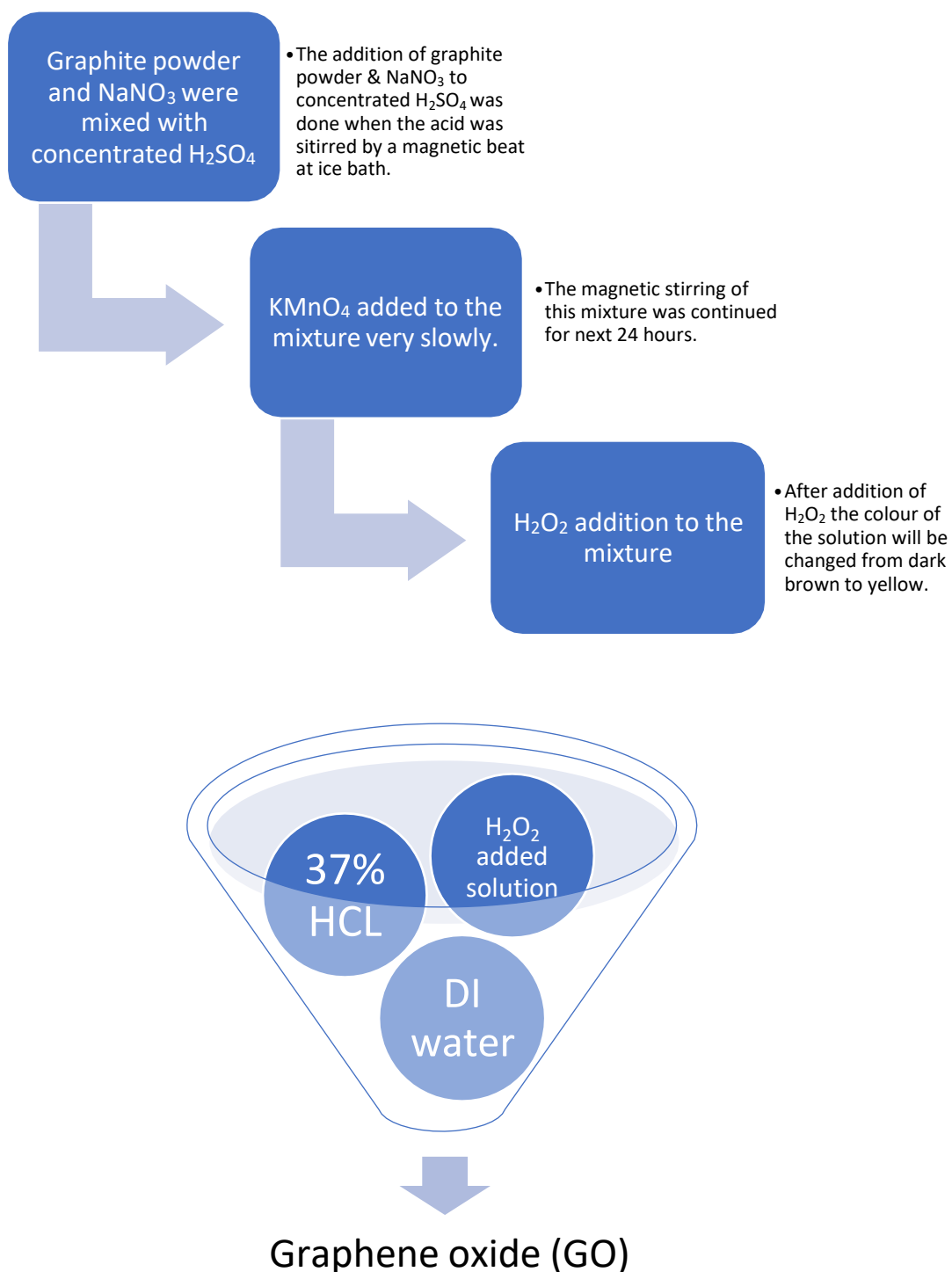


Fig 5.1. Schematic diagram of modified Hummer's method.

- **Synthesis of N-doped reduced Graphene Oxide (rGO) using hydrothermal method:**

- **Materials:** Graphene Oxide (GO) prepared using modified Hummer's method, Imidazole, ethanol ($\text{C}_2\text{H}_5\text{OH}$, 99% pure), ammonia solution (NH_4OH , 25% by weight), Teflon.

- **Sample preparation:**

1. The already prepared GO from Hummer's method is being reduced to nitrogen doped rGO using in-situ hydrothermal process. At first, 15 mg of fresh prepared GO had been added into 50 ml DI water in a 250 ml beaker and sonicated for 20 minutes so that the solid GO flakes can be dispersed well into DI.
2. After completion of sonication, the mixture was settled down for some time. In the meantime, 10 mg of imidazole was weighted and mixed with 10 ml of DI and 10ml of ammonia solution. This imidazole-ammonia-DI solution was then mixed with the dispersed GO solution and again sonicated for 10 minutes.
3. As prepared solution was then kept in a Teflon auto-clave and packed tightly into hydrothermal metal jacket. Finally, the solution was kept in oven at 90°C for 6h, 12h, 18h and 24h for different variation and comparative study of reduced graphene oxide and the role of nitrogen as a dopant.
4. After completion of the reactions, the solution was kept for getting settled and cool down to room temperature. Then, the solution was filtered through filter paper and washed subsequently with DI and ethanol for 5 to 6 times to remove excess and unreacted ammonia. Every time pH had been checked until it came to 7.
5. Once the pH of the filtered slurry N-doped rGO had come to 7, then it was dried at 50°C for 24 hours. To obtain fresh solid N-doped rGO flakes, the dried filtered paper was etched manually using spatula.

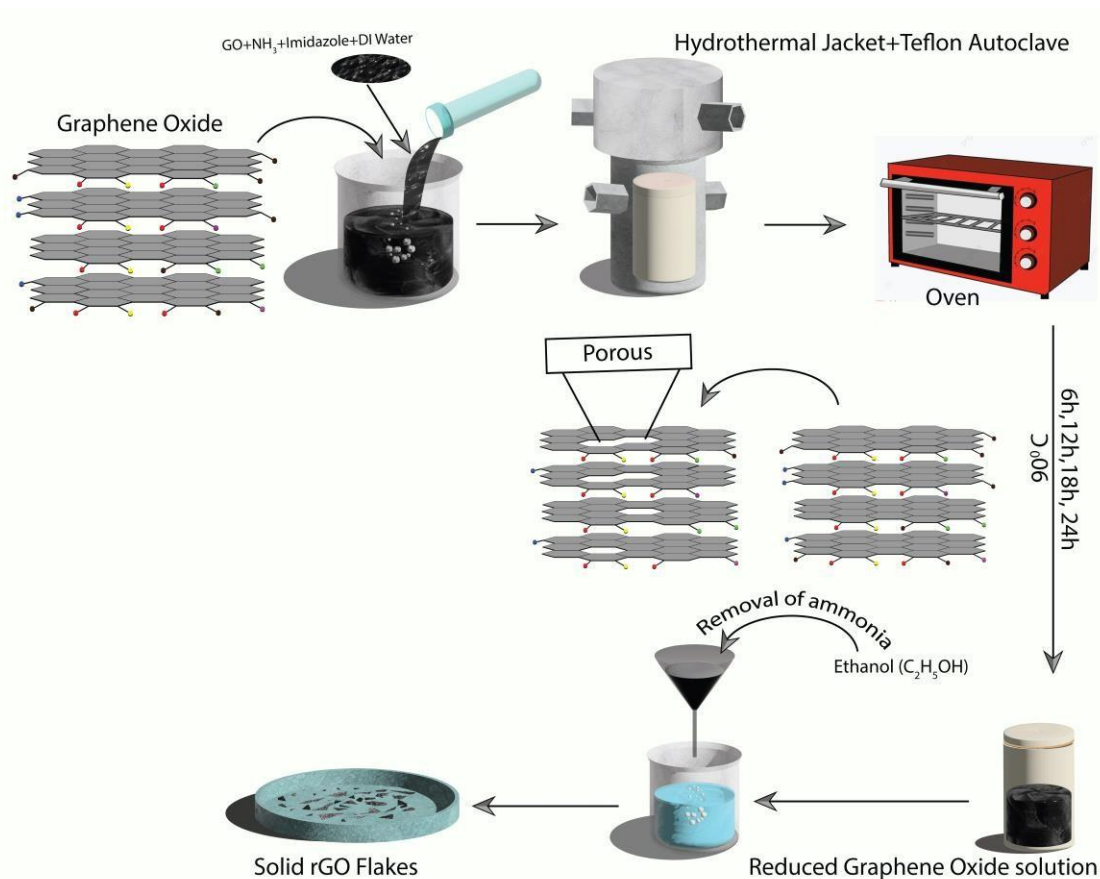


Fig 5.2. Schematic diagram of N-rGO synthesis from GO using hydrothermal process.

• Synthesis of N-type of Silicon Nanowires:

Vertical silicon nanowire was synthesis from a commercial Si wafer [n-type, (111)-oriented, 0.1-10 $\Omega\cdot\text{cm}$] by Metal (Ag) assisted chemical etching method [3]. A small piece of Si wafer (10mm×10mm in size) was processed to SiNWs by the following steps; Cleaning: Small pieces washed using the ultrasonic method with ethanol and acetone for 10 min, and then immersed in Piranha solution containing H_2SO_4 and H_2O_2 in the volume ratio of 3:1 for 20 min under room temperature to obliterate organics and to form a thin oxide layer. Then they were dipped in an aqueous solution of 14% HF for 10 min. Ag-deposition on Si-wafer: The clean Si wafer was placed immediately into an Ag coating solution containing HF (18% V/V with DI) and 10 ml of AgNO_3 (0.0234 gm) solution for 1 min. After a uniform layer of Ag nanoparticles (AgNPs) formed, the wafers were washed with deionized water to remove the extra Ag^+ ions. Etching: AgNPs deposited on Si wafer then immersed in a solution of HF

(18% V/V with DI) and H_2O_2 (1% V/V with DI) for 1.5 Hours. Then the wafers were washed repeatedly with Deionized water.

Ag-Remove: Then, etchant silicon Nanowire were immersed in 67% concentrated HNO_3 for 10 min to dissolve the AgNPs. SiNWs were washed frequently with Deionized water. After that, 14% HF (% V/V) solution was used for 10 min to removed oxides from SiNWs, then cleaned with Deionized water and Dried at 80°C for 20 min.

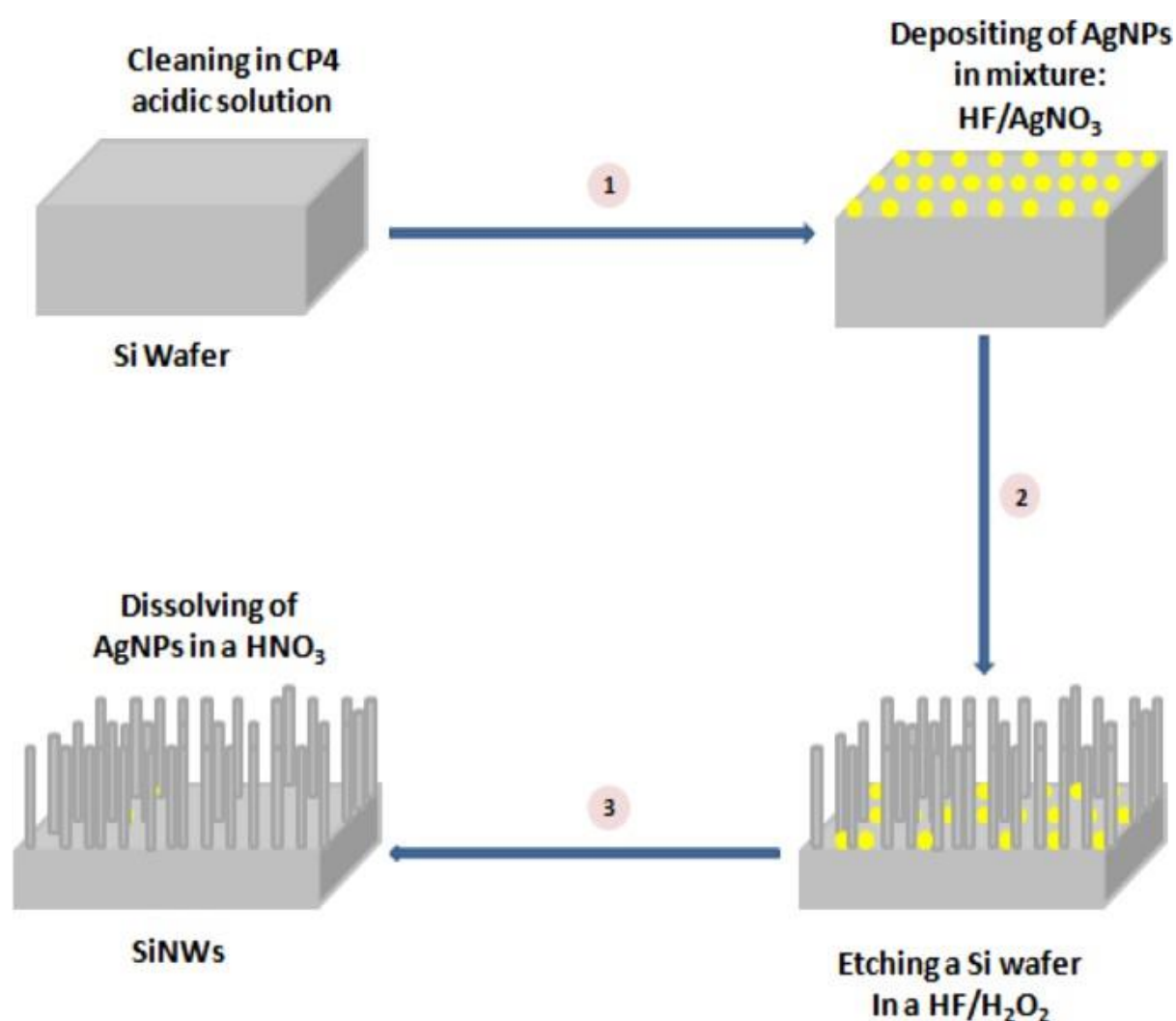


Fig 5.3. Schematic diagram of Metal assist Chemical Etching process for synthesize SiNWs.

References:

- [1] A. K. Geim, K. S. Novoselov, *Nat. Mater.* 2007, 6, 183–191.
- [2] a) C. K. Chua, M. Pumera, *Chem. Soc. Rev.* 2013, 42, 3222–3233; b) M. Pumera, *Electrochem. Commun.* 2013, 36, 14–18.
- L. Staudenmaier, *Ber. Dtsch. Chem. Ges.* 1898, 31, 1481–1487.
- [3] U. Hofmann, E. König, *Z. Anorg. Allg. Chem.* 1937, 234, 311–336.
- [4] W. S. Hummers, R. E. Offeman, *J. Am. Chem. Soc.* 1958, 80, 1339–1339.[8] C. K. Chua, Z. Sofer, M. Pumera, *Chem. Eur. J.* 2012, 18, 13453–13459.
- [9] a) A. Y. S. Eng, A. Ambrosi, C. K. Chua, F. Štaneček, Z. Sofer, M. Pumera, *Chem. Eur. J.* 2013, 19, 12673–12683; b) D. C. Marcano, D. V. Kosynkin, J. M. Berlin, A. Sinitskii, Z. Sun, A. Slesarev, L. B. Alemany, W. Lu, J. M. Tour, *ACS Nano* 2010, 4, 4806–4814.
- [10] C. K. Chua, M. Pumera, *Chem. Asian J.* 2012, 7, 1009–1012.[11] Y. Si, E. T. Samulski, *Chem. Mater.* 2008, 20, 6792–6797.
- [12] E. Morales-Narváez, A. Merkoçi, *Adv. Mater.* 2012, 24, 3298–3308.
- [13] C. Su, M. Acik, K. Takai, J. Lu, S. J. Hao, Y. Zheng, P. Wu, Q. Bao, T. Enoki, Y. J. Chabal, K. Ping Loh, *Nat. Commun.* 2012, 3, 1298.
- [14] a) R. Sitko, E. Turek, B. Zawisza, E. Malicka, E. Talik, J. Heimann, A. Gagor, B. Feist, R. Wrzalik, *Dalton Trans.* 2013, 42, 5682–5689; b) G. Zhao, X. Ren, X. Gao, X. Tan, J. Li, C. Chen, Y. Huang, X. Wang, *Dalton Trans.* 2011, 40, 10945–10952; c) G. Zhao, J. Li, X. Ren, C. Chen, X. Wang, *Environ. Sci. Technol.* 2011, 45, 10454–10462; d) C. J. Madarang, H. Y. Kim, G. Gao, N. Wang, J. Zhu, H. Feng, M. Gorrington, M. L. Kasner, S. Hou, *ACS Appl. Mater. Interfaces* 2012, 4, 1186–1193; e) Y. C. Lee, J. W. Yang, *J. Ind. Eng. Chem.* 2012, 18, 1178–1185.
- [15] F. Han, A. Banin, Y. Su, D. Monts, J. Plodinec, W. Kingery, G. Triplett, *Naturwissenschaften* 2002, 89, 497–504.
- [16] L. Järup, *Brit. Med. Bull.* 2003, 68, 167–182.
- [17] a) S. Wang, H. Sun, H. M. Ang, M. O. Tadé, *Chem. Eng. J.* 2013, 226, 336–347; b) R. Sitko, B. Zawisza, E. Malicka, *TrAC Trends Anal. Chem.* 2013, 51, 33–43; c) B. Zawisza, R. Sitko, E. Malicka, E. Talik, *Anal. Methods* 2013, 5, 6425–6430.
- [18] M. S. Mauter, M. Elimelech, *Environ. Sci. Technol.* 2008, 42, 5843–5859.
- [19] Y. Wang, S. Gao, X. Zang, J. Li, J. Ma, *Anal. Chim. Acta* 2012, 716, 112–118.
- [20] Y. Gao, Y. Li, L. Zhang, H. Huang, J. Hu, S. M. Shah, X. Su, *J. Colloid Interface Sci.* 2012, 368, 540–546.
- [21] S. T. Yang, S. Chen, Y. Chang, A. Cao, Y. Liu, H. Wang, *J. Colloid Interface Sci.* 2011, 359, 24–29.
- [22] a) M. Acik, G. Lee, C. Mattevi, A. Pirkle, R. M. Wallace, M. Chhowalla, K. Cho, Y. Chabal, *J. Phys. Chem. C* 2011, 115, 19761–19781; b) S. Park, K. S. Lee, G. Bozoklu, W. Cai, S. T. Nguyen,

- R. S. Ruoff, *ACS Nano* 2008, 2, 572–578 .D. Yang, A. Velamakanni, G. Bozoklu, S. Park, M. Stoller, R. D. Piner, S. Stankovich, I. Jung,
D. A. Field, C. A. Ventrice, Jr., R. S. Ruoff, *Carbon* 2009, 47, 145–152.
- [23] M. Giovanni, H. L. Poh, A. Ambrosi, G. Zhao, Z. Sofer, F. Sanek, B. Khezri,
R. D. Webster, M. Pumera, *Nanoscale* 2012, 4, 5002–5008.
- [24] C. Botas, P. Álvarez, C. Blanco, R. Santamaría, M. Granda, P. Ares, F. Rodríguez-Reinoso, R. Menéndez, *Carbon* 2012, 50, 275–282.
- [25] J. L. Li, K. N. Kudin, M. J. McAllister, R. K. Prud'homme, I. A. Aksay, R. Car,
Phys. Rev. Lett. 2006, 96, 176101.
- [26] a) S. Bai, X. Shen, X. Zhong, Y. Liu, G. Zhu, X. Xu, K. Chen, *Carbon* 2012, 50, 2337–2346;
b) G. D. Vuković, A. D. Marinković, S. D. Škapin, M. Đ. Ristić, R. Aleksić, A. A. Perić-
Grujić, P. S. Uskoković, *Chem. Eng. J.* 2011, 173, 855–865.

Chapter-6

Device Fabrication:

Part-I (Supercapacitor)



• **Preparation of Electrodes for supercapacitor:**

As it is known to all that supercapacitors are being operated in the same way as electrolyte capacitors with having much more energy density. Hence, alike electrolyte capacitors, supercapacitors are also having electrodes with better materials property. Electrodes are usually of conducting non-reactive materials which will eventually hold the sample in electrolyte without being participated in the electro-chemical reaction. However, the best electrode materials for supercapacitors are those with characteristics like stability, toughness, electrical conductivity, surface area, porosity, affordability, and accessibility. There are many electrode materials have been used in capacitors such as platinum, lithium, glassy carbon, nickel, brass, polyaniline, graphite etc. Among these materials, nickel foam was being the chosen one for this project due its better porosity and electron transfer capability. Nickel foam electrode with rGO material was being prepared using below steps for this project.

1. The solid rGO (reduced Graphene Oxide) flakes were dispersed in 100 micro-litres of DMF (N,N-Dimethylformamide) solvent under vigorous stirring.
2. After 1 hour of stirring, 2 mg of PVDF (Polyvinylidene fluoride) was added to the solution as a binding agent which will gradually make the solution thick for better pasting over the nickel foam. After adding, PVDF, again the solution was kept under stirring for next 3 hours.
3. In the meantime, the nickel foam was cut into small pieces with specific size and mass for later calculation and washed with DI water for 5 times. Then the oxide layers were washed with diluted HCL for 3 times.
4. Once the solution was prepared, then it was slowly casted over the washed nickel foam-pieces in specific calculated area using spatula and left it for next 4 hours to get dried and stucked with the electrode.
5. Using the same technique, 4 electrodes were being prepared with 4 different samples i.e., 6 hours, 12 hours, 18 hours and 24 hours for comparative study.

- **Preparation of Coplanar Interdigital Supercapacitor over flexible substrate:**

In modern age semiconductor device industry, it is very much needed to have small, integrated, flexible, reliable and efficient devices to incorporate for betterment of the wholesome technology. Therefore, nanotechnology is not only focused to use the potential properties of nanomaterials, also to fabricate in a very small and flexible manner. Now a days, starting from smart watch to mobile screen to any kind of electronics wearable, small scale flexible supercapacitors are in high demand. To fulfil that purpose and make my device and material useful for industry as well as society, I was focused to design coplanar interdigital capacitor over flexible substrate. It resolves many problems of usual sandwich model of electrode supercapacitors such as time taking long process to prepare electrodes, large in size, loading of lots of materials etc. with the advantage of great efficiency rate. In this project, the CI supercapacitor was designed in a very cost effective and innovative way where the electrolyte itself used as the flexible substrate.

Design of CI supercapacitors:

In this project, the design of CI supercapacitor was inspired from the ‘comb-like’ structure, where two sides of two different comb-like structure were interdigitated on a same plane with having small gaps in between them for the operation of the electrolyte. As sandwich type supercapacitors have an insulating layer (tissue paper) in between two electrodes, the same was provided in this CI model with air or the gap in between the electrode teeth. Here, the design has 5 electrode a-side of 2mm each having gap of 1 mm in between with other side electrode. There are two types of electrodes were interdigitated in this device i.e., support electrode and detective electrode. The 2mm thick electrode teeth were connected to a 5 mm thick support electrode.

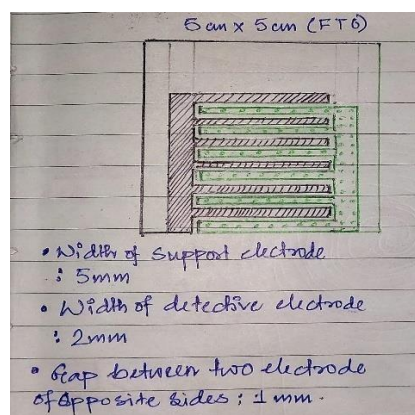


Fig 6.1. Drawing of Schematic design of rGO based symmetric CI supercapacitor

Preparation of the final device:

Step-1: Sample preparation: Like usual electrode material preparation, in this case the same technique wouldn't be sufficient to design a proper pattern. Hence, the sample for symmetric CI supercapacitor designing, the sample was prepared with more solvent and less binding materials for spraying purpose. For this reason, 5 mg of NrGO flakes were dispersed in 10 ml of DMF with 1 mg of nafion as the binding agent. This solution was kept under stirring for 2 hours.

Step-2: Designing of electrodes: At first, solid FTO (Fluorine-doped tin oxide) substrate [5cm*5cm] was cleaned with DI water multiple times and used as the primary base for patterning. The whole design was patterned one side of the electrodes at a time. For that purpose, with keeping the design intact, first the upper side of the substrate (2cm) and other side which would be eventually patterned later were tightly covered with Teflon tape. Then the whole substrate was covered fully with aluminium foil to draw the exact pattern of one side. The aluminium foil was cut into patterned design very carefully under optical microscope using surgical blade. The pattern was calibrated and cut in such a manner that, the place of support electrode and the electrode teeth were only visible over the FTO plate and other parts including the gap was still covered with foil, so that the sample could be fitted and kept intact in that much space only. The foil was intact and kept leakage-free over the substrate with the help of hair pins.

The already prepared sample solution was kept in a small spray bottle. Thus, the sample was sprayed all over the substrate very slowly and carefully so that most of the samples can be imported to the desirable places only. This step was done 7 to 8 times and after each spray, the substrate was kept under hot air for quick dry. Once the one-sided comb pattern turned into visible black pattern of NrGO, then the whole covering of hair pins, aluminium foil and Teflon were removed and checked carefully.

For, the other side, same technique as above was used, with proper maintaining of the gaps in between the electrode teeth. At last, two copper strips were attached with both sides of the support electrodes for measuring the capacitance of the device.



Fig 6.2. Digital photograph of one-sided support and detective electrodes

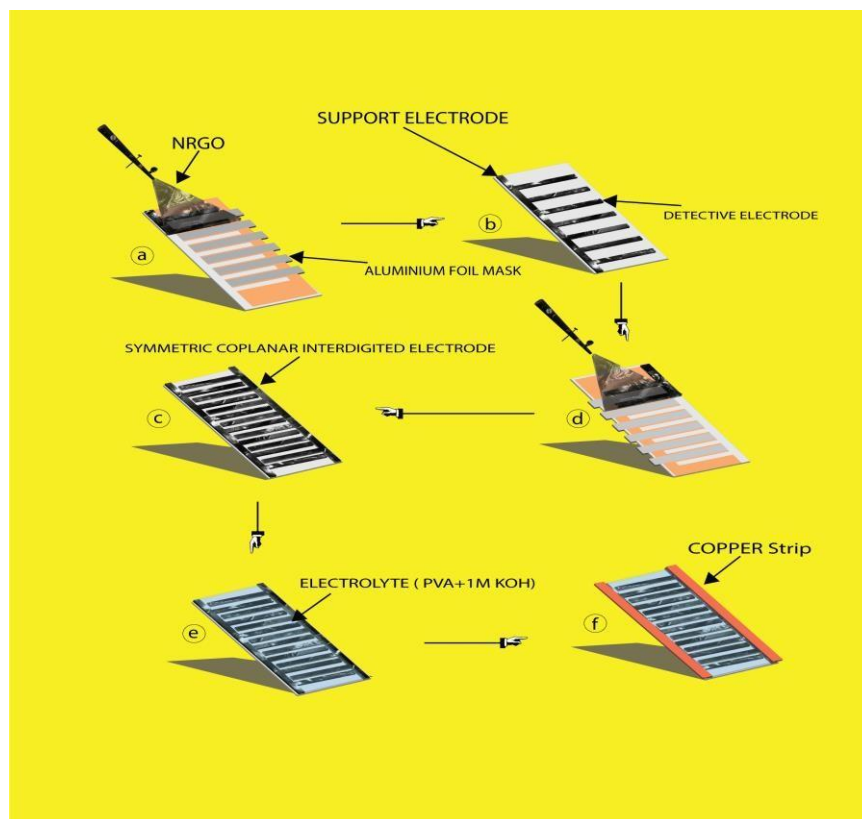


Fig 6.3. Schematic diagram of Device fabrication.

Flexible Electrolyte preparation: 1 gram of PVA (Poly vinyl alcohol) was dissolved in 10 ml of DI water. After that, 0.45 gram of KOH was added to this solution and the mixture was kept under vigorous stirring at 85⁰ C temperature for 4 hours. The stirring was observed carefully, so that the formation of electrolyte gel was not disturbed by any mean. After successful completion of stirring, 1 M KOH/PVA gel was prepared and ready for the device.

Replication of electrode design over flexible electrolyte gel: After preparing the gel, it was kept in room temperature for settling down the higher temperature. Once it was chilled down to room temperature, first layer of electrolyte gel was casted over the pattern carefully without touching the copper strips and left for 15 minutes for drying in room temperature. As PVA is a flexible polymer, the pattern of electrodes was replicating over the polymer slowly during the dry process. Due to glossy surface of FTO substrate and attaching property of polymer, the pattern was easily replicated upon completion of drying. Like the above, 2 more layers of KOH/PVA gel was layered over the FTO substrate and kept for drying. At last, the dry flexible layer of KOH/PVA was separated carefully from the surface of the FTO. Thus, the final NrGO based flexible symmetric coplanar interdigital supercapacitor was obtained for measurements.

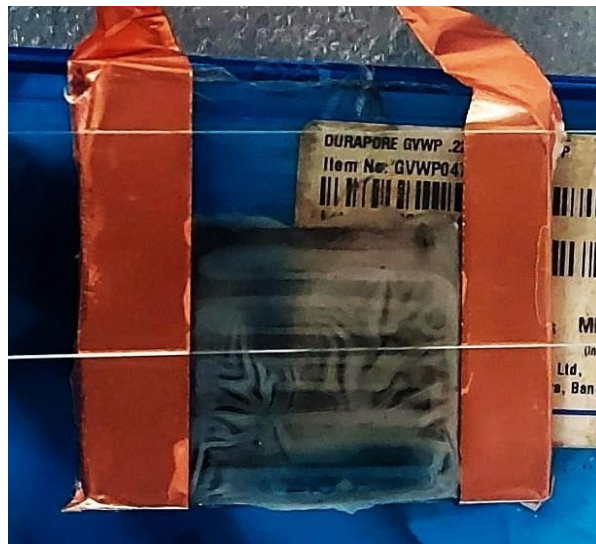


Fig6.4. Digital photograph of rGO based symmetric CI supercapacitor after casting one layer of KOH/PVA gel

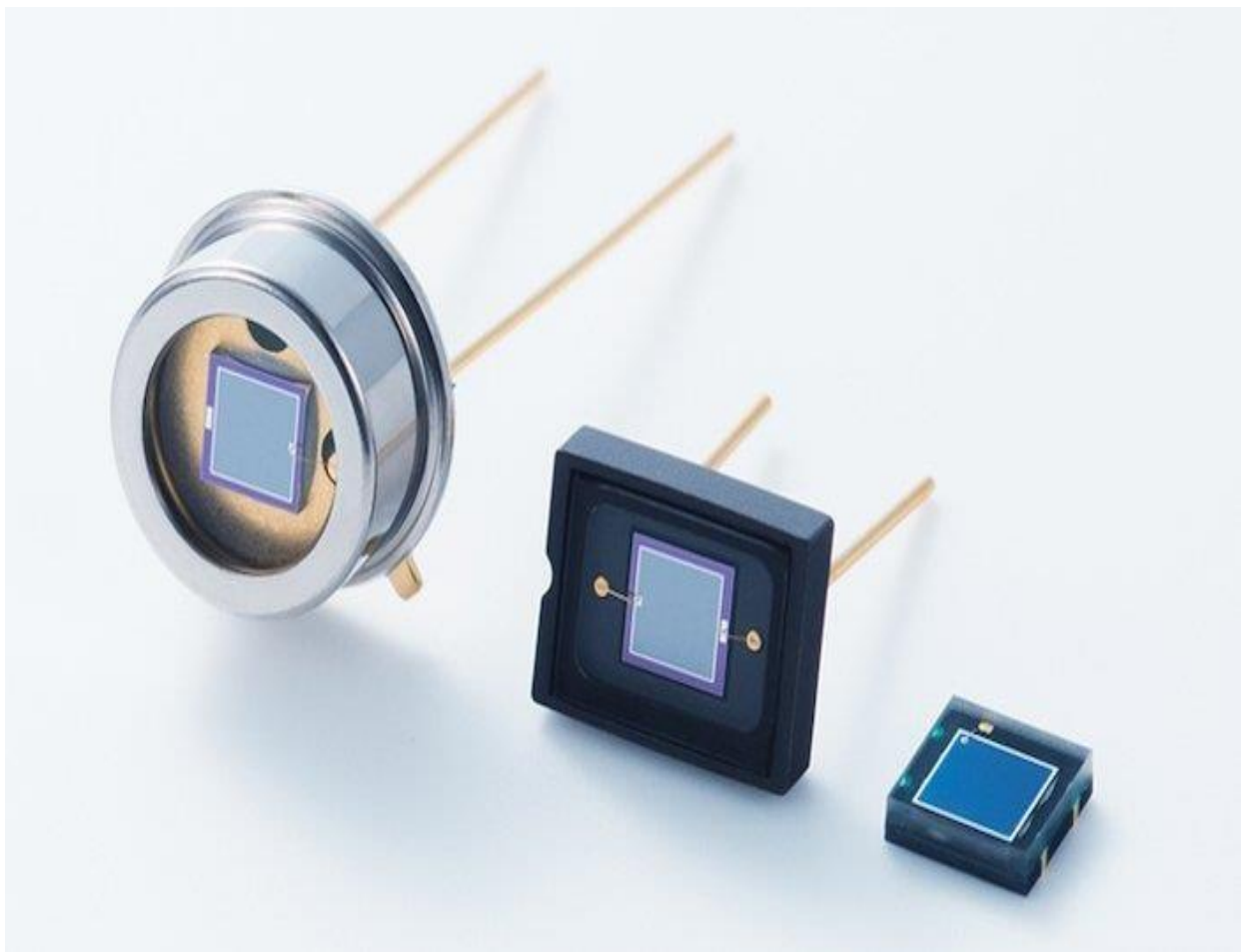


Fig 6.5. Digital Picture of final rGO based flexible symmetric CI supercapacitor.

Chapter-7

Device Fabrication: Part-II

(Photodetector)



- **Fabrication process of SiNWs/NrGO photodetector:**

The photodetector, also known as an Optoelectronics convertor, is a crucial component of the front end of an optical receiver that converts the incoming optical signal into an electrical signal. Due to their small size, quick detection speed, and high detection efficiency, semiconductor photodetectors, also known as photodiodes, are the most popular types of photodetectors used in optical communication systems. Photodiodes also have PN junction-based structures, which are similar to those of laser diodes. However, unlike a laser diode, a photodetector's PN junction is reversely biased, allowing for very little reverse saturation current to pass through the diode in the absence of an input optical signal. A photodiode's basic structure can be a straightforward PN junction, but in practice, photodiodes can have a variety of device architectures to improve quantum efficiency. An intrinsic layer, for instance, is sandwiched between the p- and n-type layers in the well-known PIN structure, which is why a semiconductor photodetector is also referred to as a PIN diode. Another popular form of detector is the avalanche photodiode (APD), which, when the bias voltage is high enough, can introduce considerable photon amplification through avalanche gain.

In an ideal situation, a photodiode instantly converts each photon of the received optical signal into a free electron, causing the photocurrent to be directly proportional to the optical signal's power. However, not every incoming photon can produce an electron in a real semiconductor material, which might be brought on by ineffective photon absorption and carrier collection. Carrier transient effect and the RC parasitic of the electric structures can both slow down photodetection. As a result, a variety of parameters, such as the semiconductor's bandgap structure, material quality, the photonic structure of the device, and electrode design, affect a photodiode's responsivity and detection speed.

In this project, the performance of **NN junction** photodiode has been studied and discussed. Below are the followed steps to fabricate SiNWs/NrGO photodiode.

1. At first, the silicon nanowires formed from the N-type silicon wafer was cleaned with HF and H₂O₂ solution to remove insulating layer of SiO₂.
2. In the meantime, the NrGO flakes were dissolved into acetone and stirred for 2 hours.
3. Then 20 μ L of the prepared solution was drop casted over the silicon nanowires using micro pipet. These SiNWs/NrGO wafers were then put in preheated oven at 60⁰ C for 15 minutes. This step was repeated for at least 10 times to enrich the concentration of rGO nanoparticles over the silicon nanowires which will eventually help to create the heterojunction.
4. Once the solution got dried and well placed over the silicon nanowires, it was again cleaned multiple times with DI water to remove the extra non-attached rGO particles from the nanowires.
5. Then 4 Ag-metal contacts had been made over the SiNWs/NrGO device using 5metal deposition evaporation technique. Thus, the SiNWs/NrGO photodiode had been finally prepared and was ready for measurement.



Fig.7.1 Digital picture of SiNW/rGO (NN) type device

References:

- [1] Barth, S.; Hernandez-Ramirez, F.; Holmes, J. D.; Romano- Rodriguez, A. Prog. Mater. Sci. 2010, 55, 563.73
- [2] Lieber, C. M.; Wang, Z. L. MRS Bull. 2007, 32, 99.
- [3] Hayden, O.; Agarwal, R.; Lieber, C. M. Nat. Mater. 2006, 5, 352.
- [4] Fan, Z.; Ho, J. C.; Jacobson, Z. A.; Razavi, H.; Javey, A. Proc. Natl. Acad. Sci. U.S.A. 2008, 105, 11066. [5] Soci, C.; Zhang, A.; Bao, X.-Y.; Kim, H.; Lo, Y.; Wang, D. J. Nanosci. Nanotechnol. 2010, 10, 1430.
- [6] Fischer, . E.; Alem n, B. J.; Tao, S. L.; Daniels, R. H.; Li, E. M.; B nger, M. D.; Nagaraj, G.; Singh, P.; Zettl, A.; Desai, T. A. Nano Lett. 2009, 9, 716.
- [7] Snyder, G. J.; Toberer, E. S. Nat. Mater. 2008, 7, 105.
- [8] Chan, C. K.; Peng, H.; Liu, G.; McIlwrath, K.; Zhang, X. F.; Huggins, R. A.; Cui, Y. Nat. Nanotechnol. 2008, 3, 31.
- [9] Liu, E.-S.; Nah, J.; Varshney, K. M.; Tutuc, E. Nano Lett. 2010, 10, 3297.
- [10] Awschalom, D. D.; Flatte, M. E. Nat. Phys. 2007, 3, 153.
- [11] Gould, C.; Pappert, K.; Schmidt, G.; Molenkamp, L. W. Adv. Mater. 2007, 19, 323.
- [12] International Technology Roadmap for Semiconductors: 2010 Update Overview; International Technology Roadmap for Semiconductors, 2010.
- [13] Ford, D. Semiconductor Revenue Expands by Record Margin in 2010, IHS iSuppli, 2010. Available online: www.isuppli.com.
- [14] J. de Boer , N. Geyer , J. V. Wittemann , U. Gösele , V. Schmidt , Nanotechnology 2010 , 21 , 095302.
- [15] Y. Harada , X. L. Li , P. W. Bohn , R. G. Nuzzo , J. Am. Chem. Soc. 2001 , 123 , 8709 .

Dr. slike Hpltmanns et al., "Cellular Authenticfication for mobile & Instrument services",

Chapter-8

Results and Discussion



In this chapter, different types of material characterization techniques for hydrothermally synthesized reduced Graphene Oxide (rGO) and metal assist-chemically etched silicon nanowires (SiNWs) have been discussed intensively. These various kinds of characterization techniques include morphological characterization & analysis; crystallographic characterization & analysis and optical or spectroscopic characterization & analysis. Apart from these techniques, to investigate the capacity and efficiency of the final devices, electrochemical and electrical characterization techniques are also being performed thoroughly.

- **Morphological Characterization & analysis:**

This thesis work involves mainly two types of morphological characterization for the two different samples such as rGO and SiNWs. These are field emission scanning electron microscopy (FESEM) and high-resolution transmission electron microscopy (HRTEM). FESEM image describes the basic morphological structure of the nanoparticles or nanosheets in the range of 500 nm to 5 μ m. Whereas, HRTEM image provides information about the morphological insights of the nanoparticles such as porosity, length of nanorods etc in the range of 20nm to 100nm.

- **Field Emission Scanning Electron Microscopy (FESEM) of N doped rGO:**

Reduced graphene oxide is having almost same morphology as graphene oxide or graphene which refers to the nano-structure of 2D nanomaterials. Their primary morphological structure imitates to a sheet like or layered structure. Here, a crust of thin layers can be seen in NORG-6h FESEM images [fig (a) & fig (b)] [1]. As the time is low for this synthesis process, the reduction is comparatively low which is resulting small broken thin layers of N-rGO. Now, in the case of NORG-12h [fig (c) & fig(d)], the layers are stacked one upon one and having long sheets with compared to NORG-6h[2].

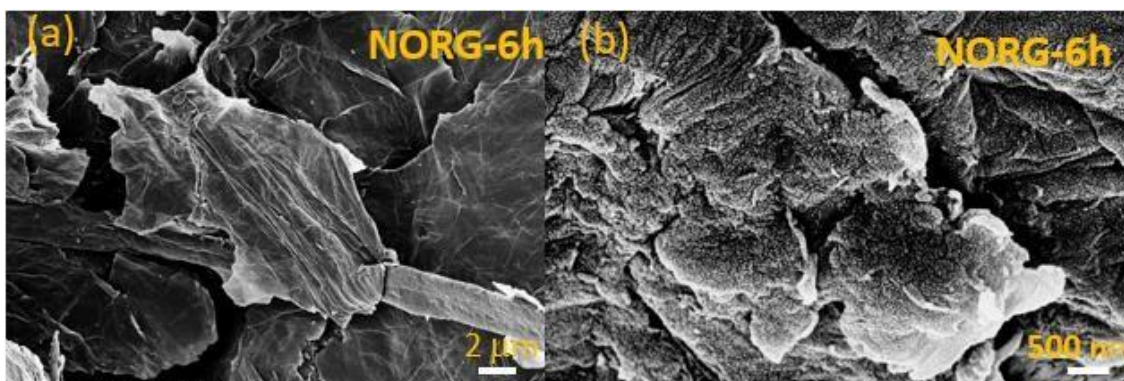


Fig 8.1 (a, b). FESEM image of NORG-6h

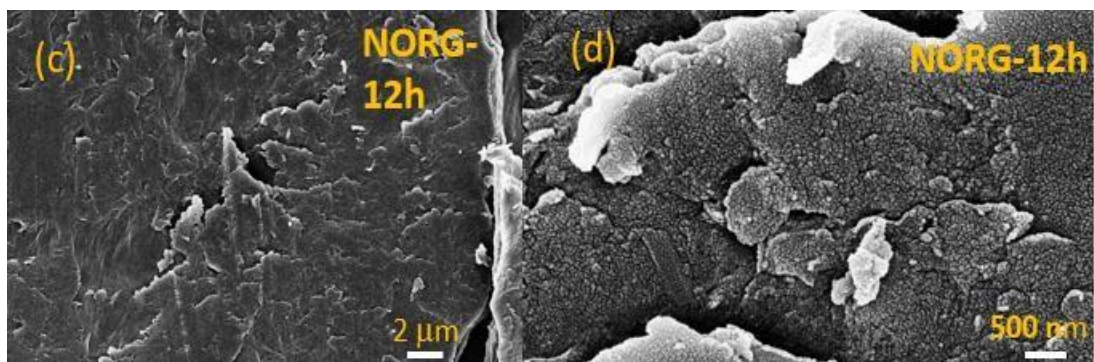


Fig 8.2 (c, d). FESEM image of NORG-12h

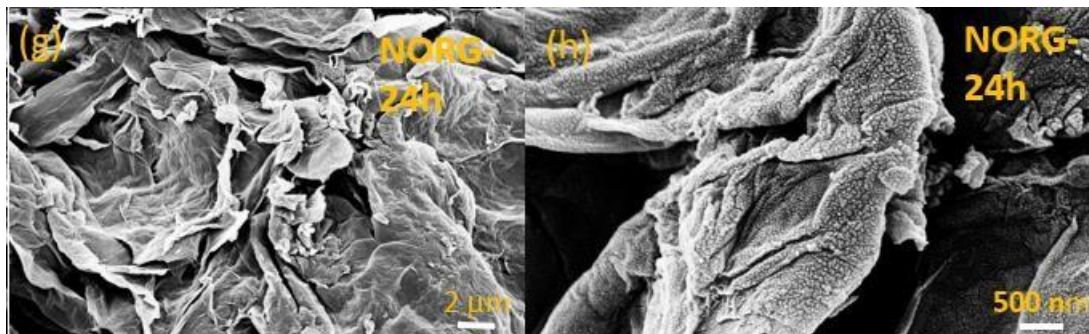
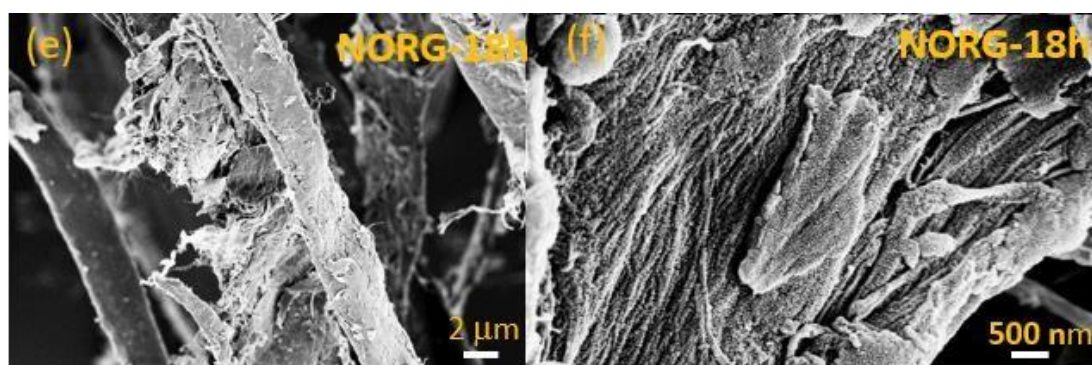


Fig 8.3 (e, f, g, h). FESEM image of NORG-18h & NORG-24h

On the other hand, from the FESEM images of NORG-18h [fig (e) & fig (f)], it is evident that with time the reduction is increasing and resulting crushed long strains of layered N doped rGO. From fig(f), it can be seen that the aggregation of the layers has been increased in NORG-18h with compared to NORG-6h and NORG-12h. Finally, from the NORG-24h [fig (g) & fig (h)] FESEM images, it is clear that with time the reduction had been increased and resulted large, mostly uniform and unbroken layers of N-doped rGO. Fig (g) provides the confirmation of successful preparation of the best thin layered N doped rGO among the other samples i.e., NORG-6h, NORG-12h & NORG-18h [7].

- **FESEM of Silicon Nanowires:**

The surface morphology and structure of the pure SiNWs nanostructures has been investigated by the field emission scanning electron microscope (FESEM) images as displayed in Figure 1. It is observed that nanowires have grown uniformly over the entire silicon wafer fig.(a) and fig.(b). It can be clearly seen that porous SiNWs are developed uniformly over the entire field of view, thus the yield is very high. The nanowires are vertical as (111) oriented silicon wafer is used for the experiment. It is seen in fig.(c) and fig. (d) that the tips of the nanowires get agglomerated for SiNW due to excessive increment of its length. The possible reason behind this conglomeration has been discussed by Zhang et. al. [24], and it describes about strong forces among the tip of the long nanowire which is due to dangling bonds and electrostatic charges resulting in mutual interaction between them.

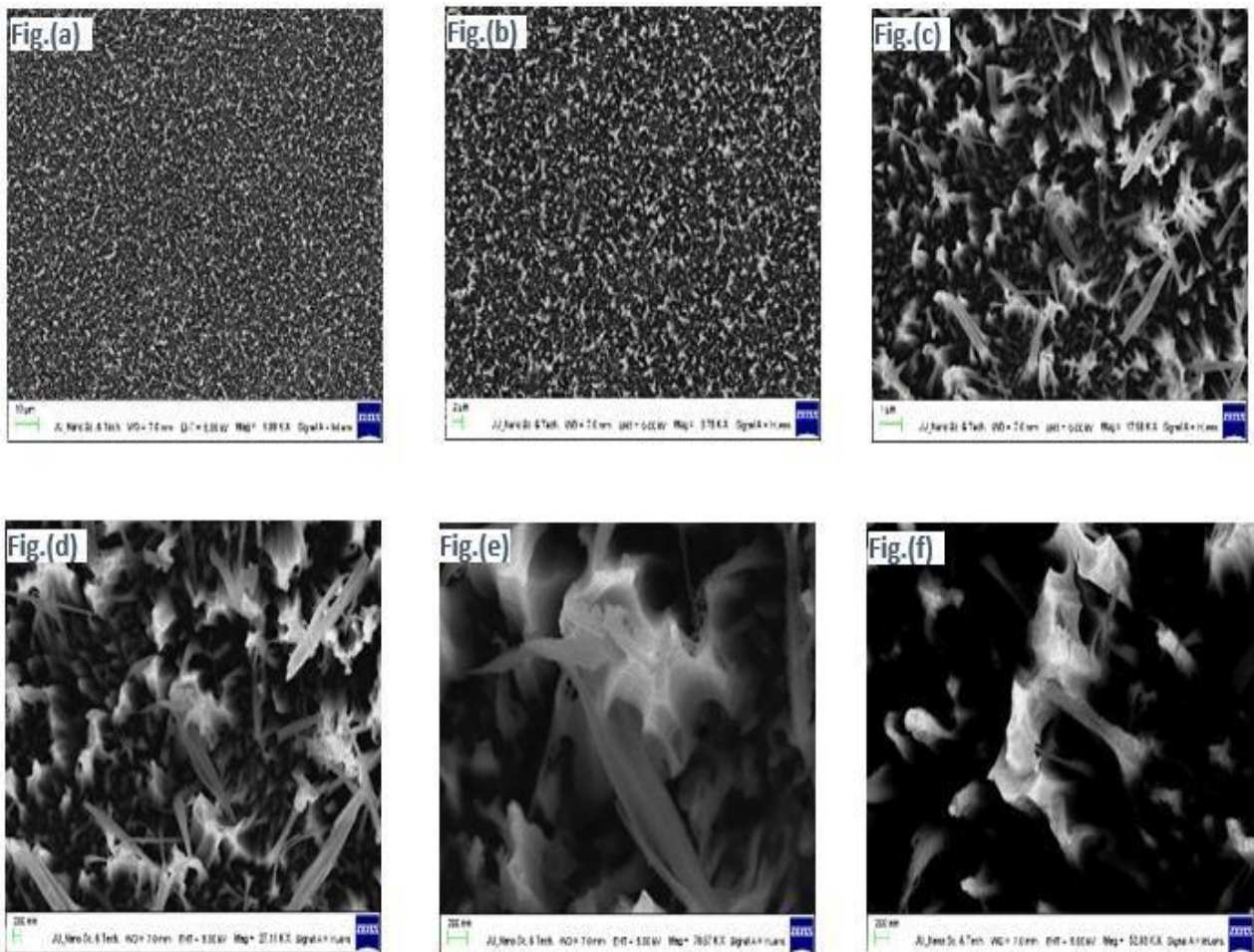


Fig 8.4 (a, b, c, d, e, f). Top view of MACE synthesized SiNWs.

- **High-resolution transmission electron microscopy (HRTEM) of N doped rGO:**

From the below HRTEM images, the nature of a single layer of N doped rGO is revealed. It is very much clear from the high-resolution images that the nature of the thin layer of rGO is porous. Because of this porous nature only, the super capacitive nature is evident in rGO. Hence, proving the porosity and nature of the porosity is very important in this project. In fig (a), the distribution of porosity is low throughout the sheet, nevertheless with increase in time of synthesis process, the porosity distribution and porous area have been increased. We can see in NORG-24h, the porosity distribution is comparatively much higher than NORG-6h, NORG-12h and NORG-18h. In NORG-24h even the size of pores has been increased, which suggests great reduction of graphene oxide [4].

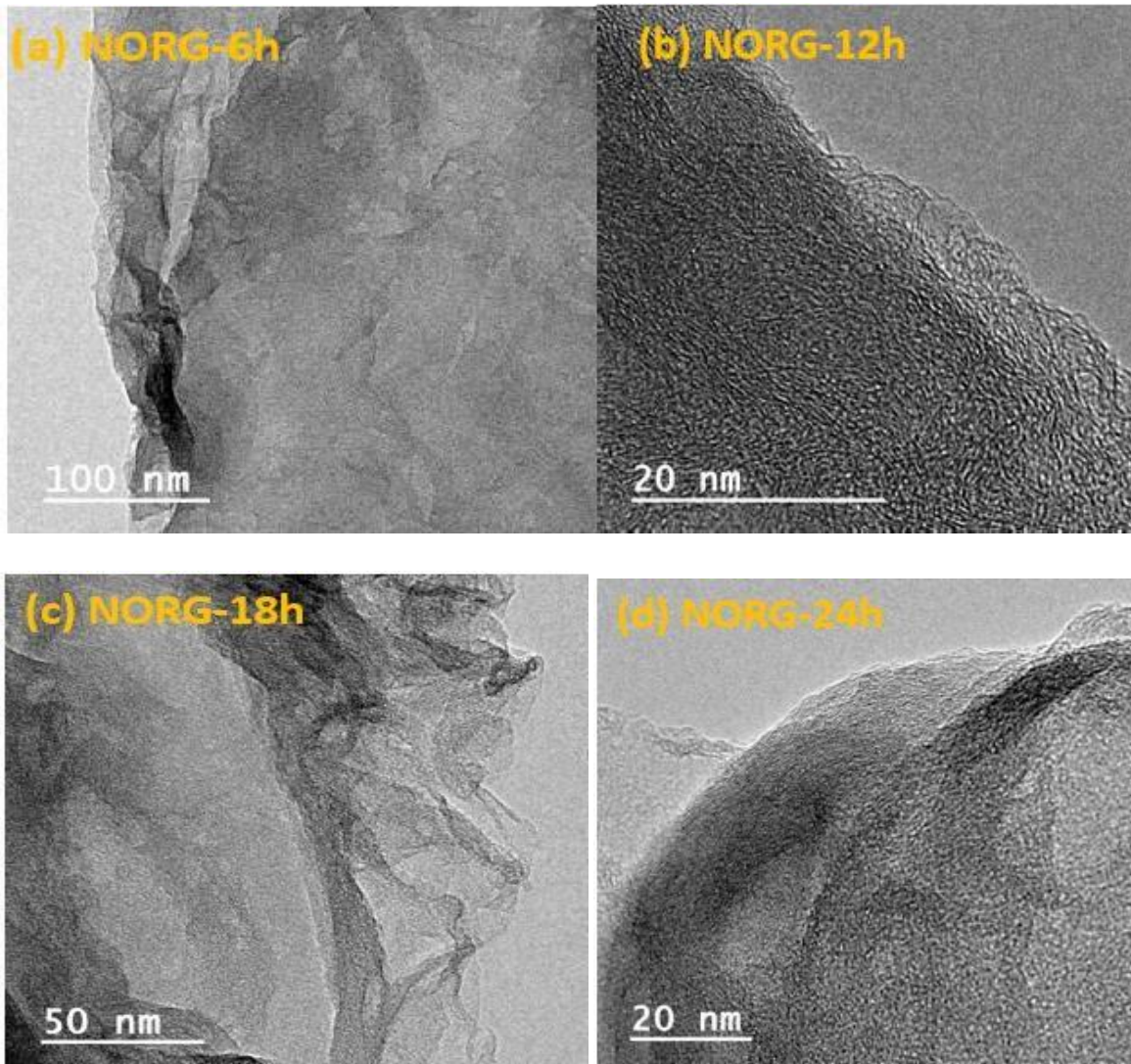


Fig 8.5. HRTEM images of NORG-6h (a), NORG-12h (b), NORG-18h (c) & NORG-24h (d).

- **Crystallographic Characterization & Analysis:**

To confirm the crystallographic nature such as crystal structure, interplanar spacing, lattice structure etc. it is very important to perform X-Ray Diffraction (XRD) for the samples. For this project work, XRD had been conducted for hydrothermally synthesized reduced graphene oxide. Here, an illustrative and comparative study of XRD analysis has been carried out and discussed below for NORG-6h, NORG-12h, NORG-18h and NORG-24h.

- **X-Ray Diffraction Analysis (XRD):**

XRD tool is being operated on the basic principle of Bragg's law of diffraction. It offers the information about the crystal type of the material such as amorphous or crystalline structure and the interlayer spacing in between two layers of the material. In this project work, at first, the peak of XRD plots of every sample has been compared with JCPDS database to confirm if the produced material is reduced graphene oxide or not [9]. The average peak angle (2θ) is equivalent to the JCPDS database record to confirm the products are rGO only. From the below graph, it is also confirmed from the hump or broadness of the peak that these materials are amorphous in nature [12].

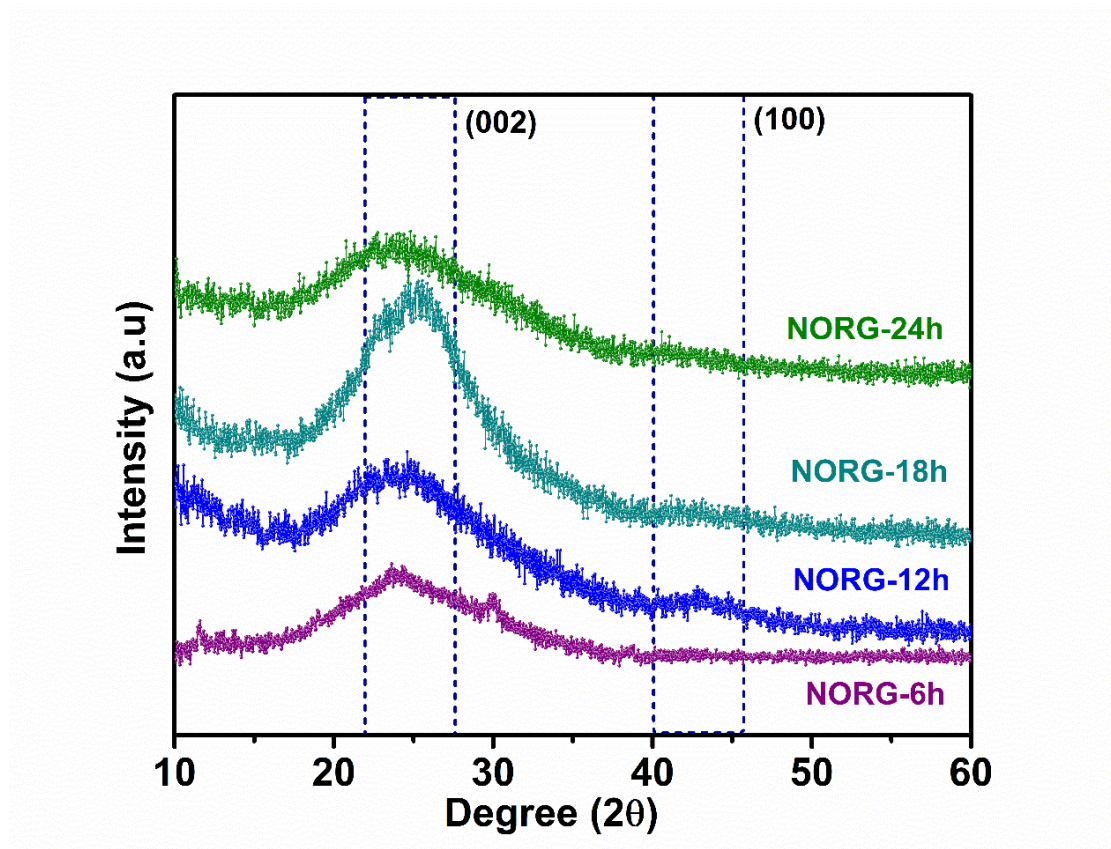


Fig 8.6. XRD analysis of NORG-6h, NORG-12h, NORG-18h & NORG-24h

On the other hand, XRD measurement of NORG-6h results a broad peak of (002) at $2\theta = 24.1077^\circ$. According to Bragg's law, we know,

$$n\lambda = 2d \sin\theta$$

Where n = order of reflectance = 1, λ = wavelength of X-ray = 1.5406 angstrom, d = interplanar spacing, θ = half of Bragg's angle.

Using the above relation, the interlayer spacing can be calculated easily for NORG-6h which is 3.68 angstrom. Like the same way, 2θ values are 24.68° , 24.81° and 25.07° for NORG-12h, NORG-18h and NORG-24h respectively [23]. The d values for NORG-12h, NORG-18h and NORG-24h are 3.60 angstrom, 3.58 angstrom and 3.54 angstrom in serial order. From the calculated interlayer spacing d values, it is evident that the distance decreases with the increase of the synthesis time. The decrease in interlayer spacing confirms the loss of oxygen functional groups like -CHO, -COOH, -C-O in rGO sheets with increase in time of reduction. As the 2θ value from NORG-6h to NORG-24 is increasing and right shifted, it results the enhancement of Van der Waals interactions in between the rGO atoms and stacking of rGO sheets. The out of plane crystallinity is decreased from NORG-6h to NORG-24h due to expulsion of graphene layer for reduction and resulting certain increase in in-plane grain size.

Materials	2θ (Degree)	d (Angstrom)
NORG-6h	24.10	3.68
NORG-12h	24.68	3.60
NORG-18h	24.81	3.58
NORG-24h	25.07	3.54

Table 8.1: Comparison table of 2θ and d for NORG-6h, NORG-12h, NORG-18h & NORG-24h.

Apart from interspacing distance, there are other characterization peaks of NORG-6h, NORG-12h, NORG-18h and NORG-24h are determined near at $2\theta = 42.46^\circ$, 42.59° , 42.71° , and 42.84° respectively, which is deconvoluted for component (100). The intensity of NORG-6h is much lower with respect to NORG-24h due to lack of in-plane crystallinity. As the reduction time increases, it results certain increase in in-plane crystallinity.

• Spectroscopic Characterization & Analysis:

➤ UV-Vis Spectroscopy of rGO:

Ultraviolet-visible spectroscopy is reflectance spectroscopy and absorption spectroscopy comprising of the ultraviolet and the adjacent full visible regions of electromagnetic spectrum, i.e., it uses light in the visible and the adjacent ranges. The reflectance or absorption in the visible range directly affects the perceived colours of the chemicals involved. In this region of the spectrum, atoms and molecules undergo electronic transitions. Absorption spectroscopy is complementary to fluorescence spectroscopy. Fluorescence deals with the transition from the excited state to the ground state whereas, absorption deals with the transition from ground state to the excited state.

Spectroscopic analysis is usually done in solutions but solids and gases may also be studied using this. It can also be used to determine kinetics or the rate of a chemical reaction.

Optical band gaps also can be calculated using UV-Vis data from Tauc plot. A Tauc plot typically displays the quantities $h\nu$ (the photon energy) on the abscissa and $(\alpha h\nu)^{1/2}$ on the ordinate, where α is the material's absorption coefficient. The energy of the optical bandgap of the amorphous material can then be obtained by extrapolating this linear region to the abscissa [12].

In this work, the main focus was always to obtain the optical band gap from UV-Vis data. It eventually helps to confirm which sample of NORG is having better band gap and can be used as the best material for device fabrication of photodetector or photodiode.

From the below Tauc plots of NORG-6h, NORG-12h, NORG-18h and NORG-24h, it can be found that the linear abscissa touches the photon energy ordinate defines their direct band gaps respectively. Here we can see NORG-6h is having highest band gap of 1.64 eV and NORG-24h has 1.50 eV.

Materials	Band gap (eV)
NORG-6h	1.64
NORG-12h	1.56
NORG-18h	1.53
NORG-24h	1.50

Table 8.2: Band gaps from Tauc plot of NORG-6h, NORG-12h, NORG-18h & NORG-24h

Tauc plot is derived from UV-Vis data consisting absorption and wavelength. Basically, one ordinate of Tauc plot is $(F(R).E)^2$ or $(\alpha h\nu)^{1/2}$ which equals to $[1240/\text{Wavelength of UV-Vis}]$. While calculation of photon energy is quite complicated and multi-step process. At first, the value of absorption is multiplied by 2.303 and the resulted value is again multiplied with the value of $[1240/\text{Wavelength of UV-Vis}]$. Finally, photon energy will be equals to the square of this value [9].

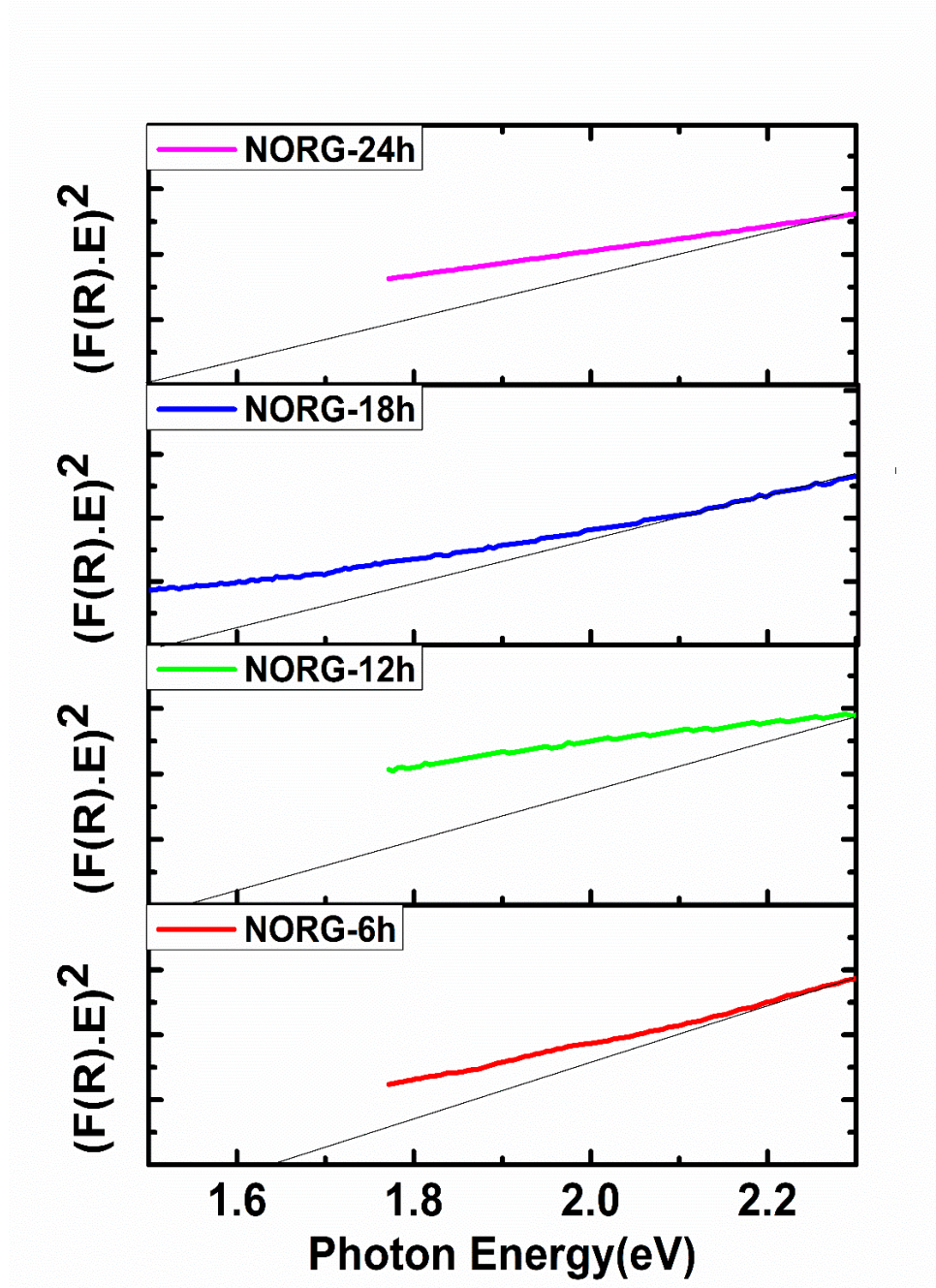


Fig 8.7. Tauc plot and band calculation of NORG-6h, NORG-12h, NORG-18h and NORG-24h.

➤ **FOURIER TRANSFORM INFRA-RED SPECTROSCOPY (FTIR) of rGO:**

The reduction process of graphene oxide has done to remove different oxygen functional groups such as carboxyl, epoxy, hydroxyl etc. from the plane of graphene. Here, FTIR provides the vibrational frequency of these groups. Hence by analysing the peaks and their intensity, the successful reduction of GO can be confirmed. From the below FTIR plot of the 4 samples have FTIR stretching frequency of 3448 cm^{-1} , 2930 cm^{-1} , 1658 cm^{-1} , 1540 cm^{-1} , 1120 cm^{-1} and 959 cm^{-1} for -OH, C-H, C=C, C=N, C-O-C and C=O groups respectively [14]. In NORG-24h, the intensity of -OH bond is comparatively low which has been increased and gets its highest intensity in NORG-6h. It defines the demonising of -OH group and confirms the successful reduction. Where as C-H bond is also vanishing towards NORG-24h from plane bend. For, obvious reasons the C=C bond remains almost same in frequency in all the samples, which implies no change in the structure of carbon bonds in rGO due to reduction [11]. On the other hand, C=N bond's frequency has been increased from NORG-6h to NORG-24h which confirms successful doping of nitrogen at the plane edge of rGO. Apart from these peaks, two small peaks correspond to C-O-C and C=O have been observed, though C=O bond has slightly more frequency in NORG-24 with compared to other samples [17].

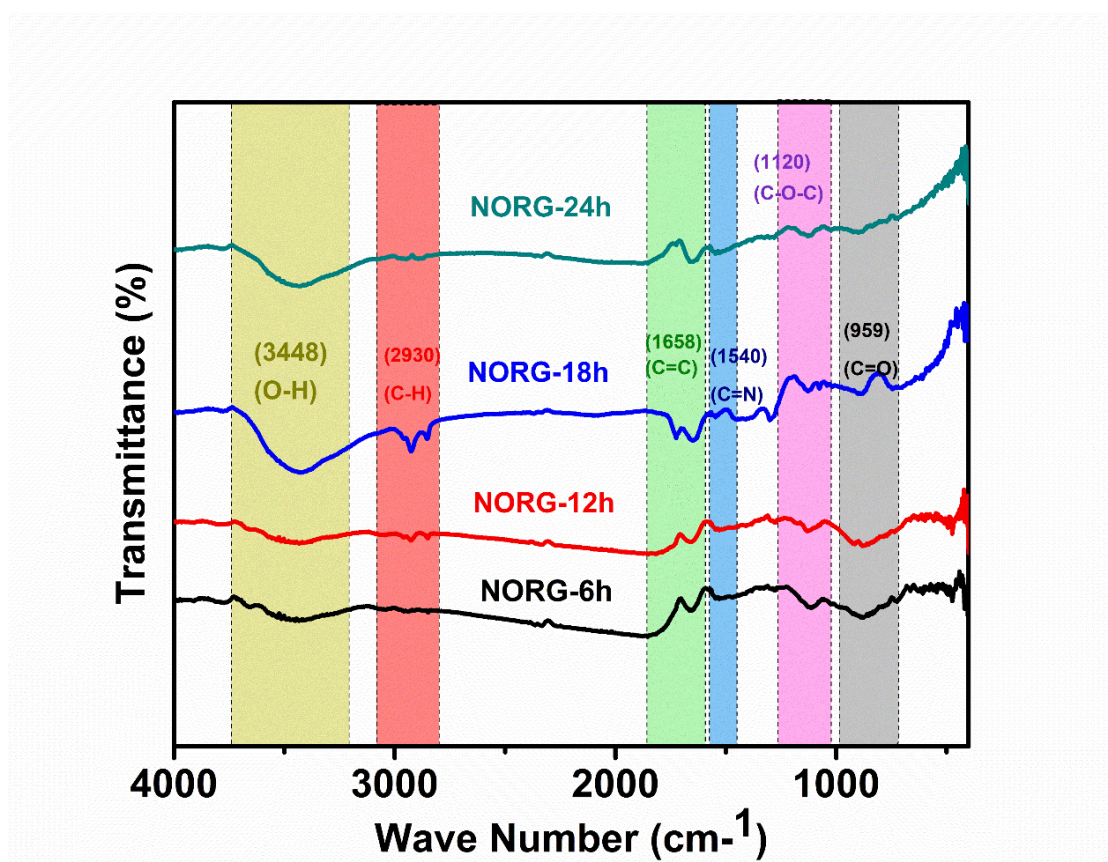


Fig 8.8. FTIR plot of NORG-6h, NORG-12h, NORG-18h & NORG-24h.

➤ X-Ray Photoelectron Spectroscopy (XPS) of rGO:

X-Ray photoelectron spectroscopy (XPS) is a very important instrument to confirm the addition of nitrogen functionalization after reduction and to determine the percentage of different elements in NrGO samples. Here, in this work, 3 types of high-resolution spectrums such as C1 s, N1 s and O1 s have been used to determine different groups.

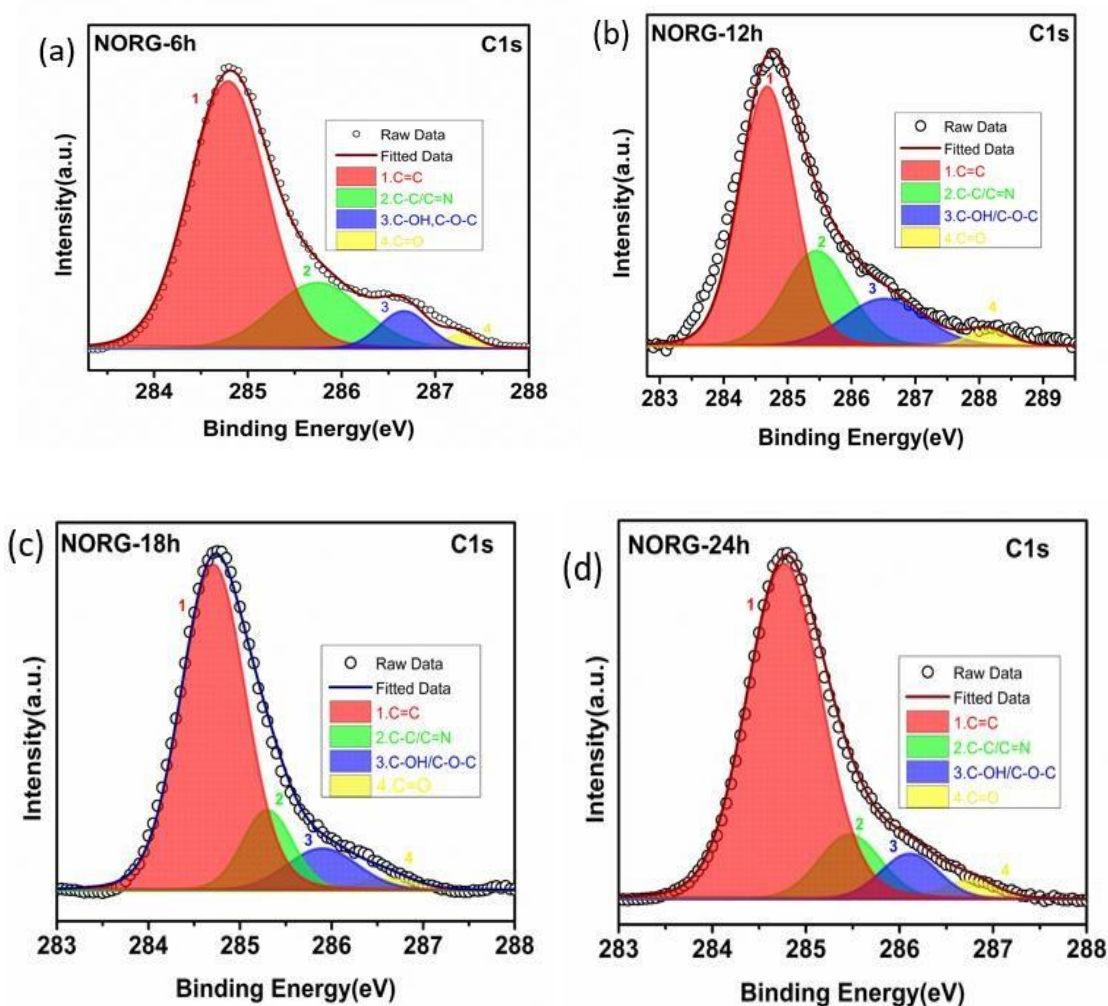


Fig 8.9. C1 s XPS spectrum of NORG-6h (a), NORG-12h (b), NORG-18h (c) & NORG-24h (d)

The high-resolution C1 s XPS spectrum indicates different functional groups attached with carbon such as C=C, C-C/C=N, epoxy carbon and C=O. The obtained peaks of NORG-6h on the ordinate of binding energy are 284.7 eV (C=C), 285.7 eV (C-C/C=N), 286.6 eV (epoxy carbon) and 287.2 eV (C=O) [fig a] [20]. Whereas, in NORG-24h, due to reduction the intensity of epoxy carbon groups have been lower and the trend has been followed in other 2 samples as well. On the other hand, intensity and area of the peak corresponds to C=N have

been increased in NORG-24h due to successful addition of nitrogen functional group. Percentage of epoxy carbon groups in NORG-6h is 15.35%, which has been significantly decreased in NORG-24h as 6.38%. Percentage of C=C bond has also been increased from 67.05% to 76.75% in NORG-6h to NORG-24h. This indicates the successful reduction of GO and addition of nitrogen groups.

Groups	NORG-6h (%)	NORG-12h (%)	NORG-18h (%)	NORG-24h (%)
C=C	67.05	71.56	73.26	76.75
C-C/C=N	12.24	14.11	20.51	24.91
C-OH/C-O-C	15.35	10.41	8.07	6.38
C=O	1.53	2.19	2.68	2.92

Table 8.3. Percentages of different C1 s groups of NORG-6h, NORG-12h, NORG-18h & NORG-24h.

N1 s spectrum of NRGO-6h has been assigned peak at 398.5 eV, 399.6 eV, 400.8 eV and 401.8 eV corresponding to pyridinic, amine, pyrrolic and graphitic nitrogen respectively [17]. Percentage of pyradinic (16.24%) and amine (73.13%) are comparatively high in NORG-6h, though the percentage of graphitic nitrogen (1.39%) is less. On the other hand, percentage of pyrrolic nitrogen has been increased in NORG-24h. With increasing synthesis-time at a constant temperature makes significant effect on graphitic nitrogen, which has been increased in NORG-24h. It may be because of more bond creation in between sp^2 carbon with more nitrogen. This confirms successful addition of nitrogen functional groups.

Groups	NORG-6h (%)	NORG-12h (%)	NORG-18h (%)	NORG-24h (%)
Pyridinic	16.24	10.39	9.09	7.39
Amine	73.13	69.15	65.92	64.48
Pyrrolic	9.24	17.13	20.70	23.58
Graphitic	1.39	3.33	4.27	4.53

Table 8.4. Percentages of different N1 s groups of NORG-6h, NORG-12h, NORG-18h & NORG-24h.

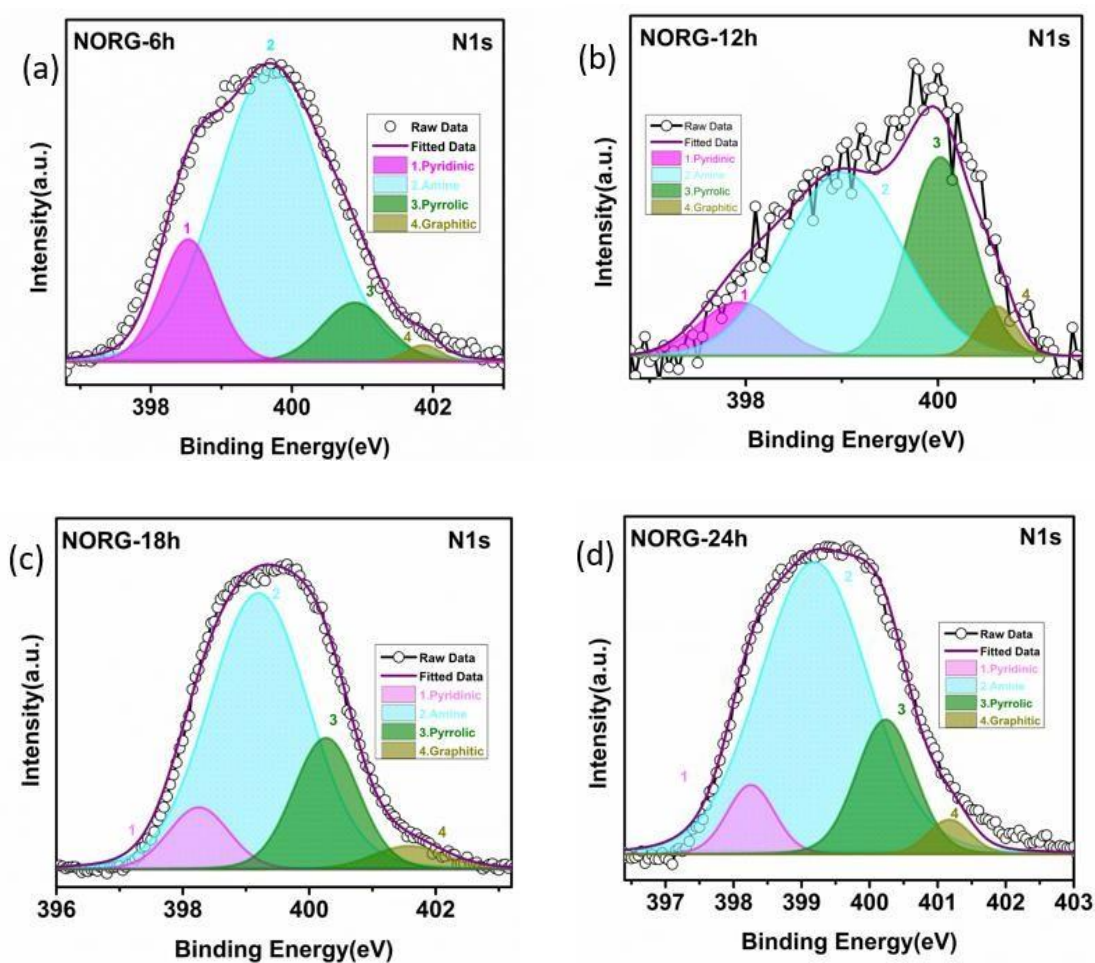


Fig 8.9. N1 s XPS spectrum of NORG-6h (a), NORG-12h (b), NORG-18h (c) & NORG-24h (d)

Groups	NORG-6h (%)	NORG-12h (%)	NORG-18h (%)	NORG-24h (%)
C=O	59.02	57.91	55.28	51.74
C-O	29.25	31.73	32.60	33.91
C-OH	8.63	8.29	9.10	9.52
O-C=O	3.09	2.07	2.91	4.81

Table 8.5. Percentages of different O1 s groups of NORG-6h, NORG-12h, NORG-18h & NORG-24h.

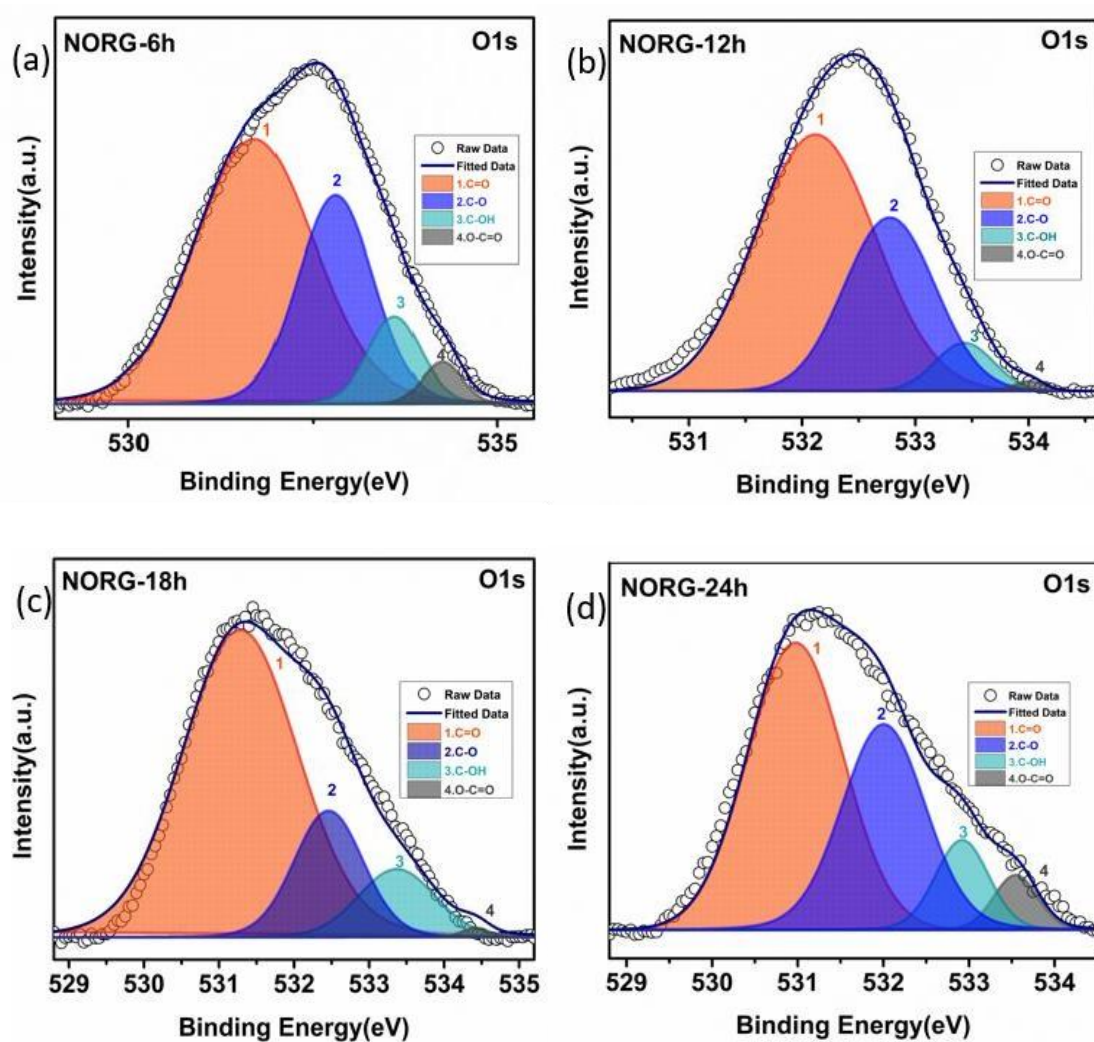


Fig 8.10. O1 s XPS spectrum of NORG-6h (a), NORG-12h (b), NORG-18h (c) & NORG-24h (d)

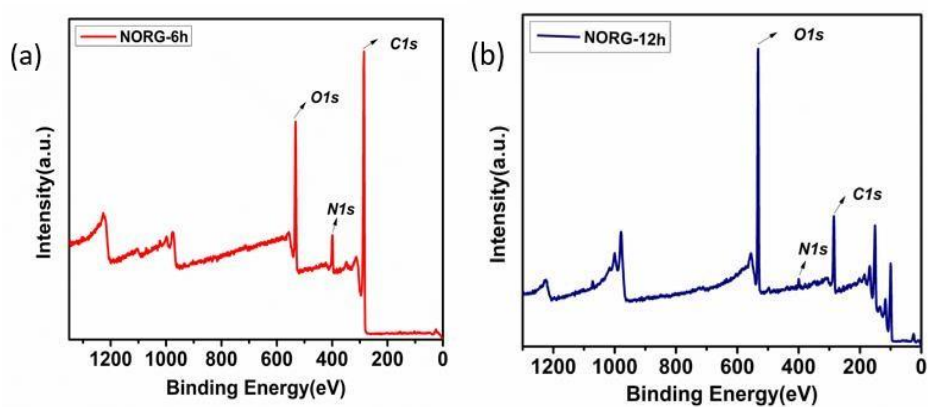


Fig. 8.11. XPS survey of NORG-6h (a) & NORG-12h (b)

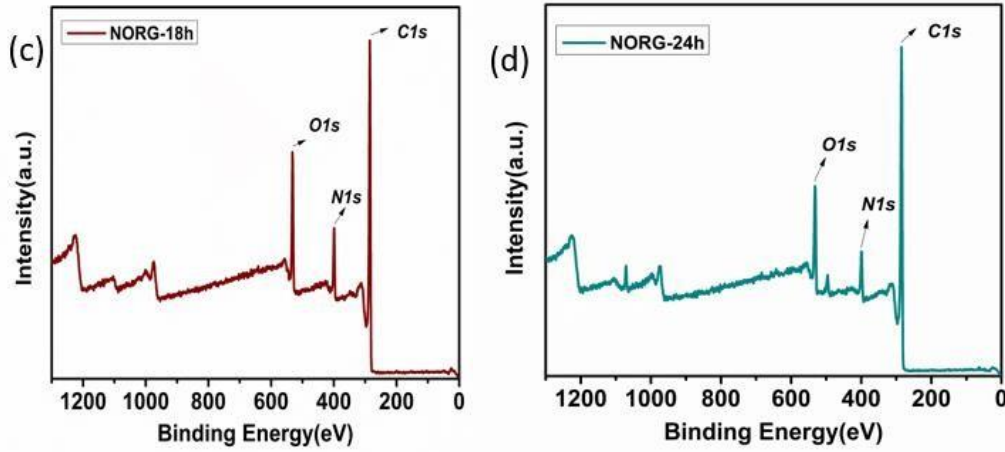


Fig. 8.11. XPS survey of NORG-18h (c) & NORG-24h (d)

➤ Raman Spectroscopy of rGO:

Raman spectroscopy provides two different peak spectrums corresponding of defect plane D and in-plane stretching vibration of sp^2 carbon, G band. D band has a useful significance to detect the defect state due to hetero-oxygen and nitrogen atoms are present as well as restoration of breathing mode in sp^2 hybridized hexagonal graphene ring. In NORG-6h sample, the peaks of D band and G band are 1340 cm^{-1} and 1571 cm^{-1} respectively. On the other hand in NORG-24h, the positions have been shifted of both D and G bands i.e., 1349 cm^{-1} and 1577 cm^{-1} respectively. The area of the D band has been broadened in NORG-24h with compared to NORG-6h, Whereas, shrinking in G band area can aslo been observed. This implies that with reduction defects in plane have been increased and restoration of sp^2 carbon has also been carried out. This confirms successful reduction of GO to NrGO.

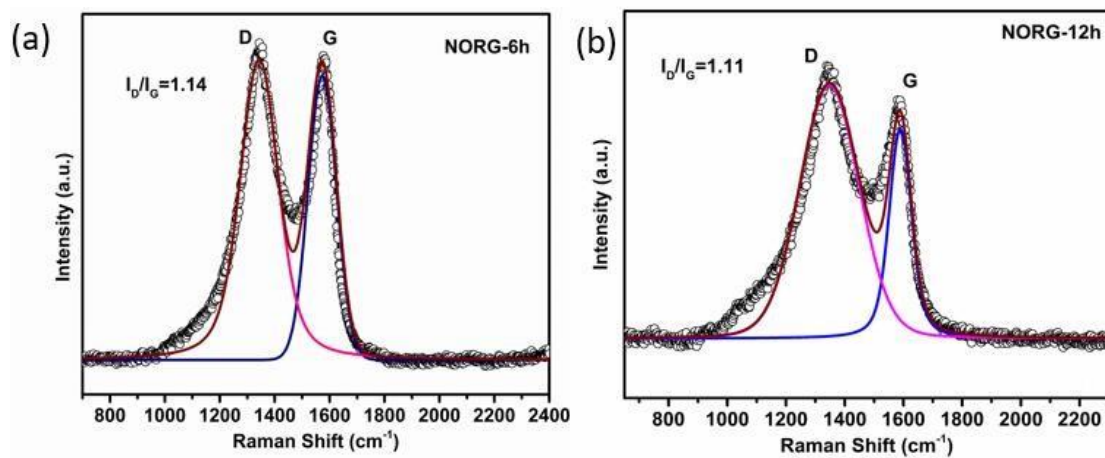


Fig 8.12. Raman Spectrum of NORG-6h (a) & NORG-12h (b)

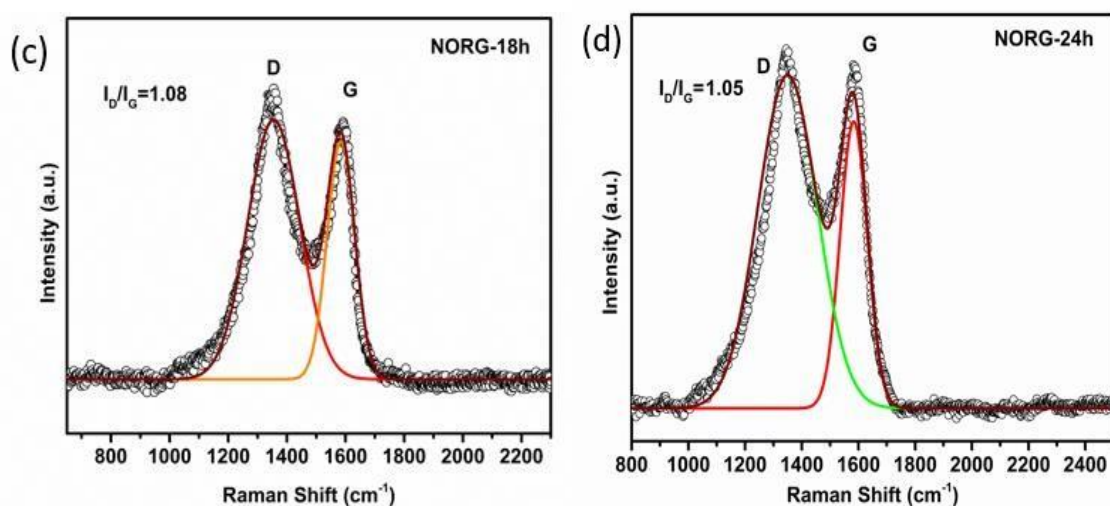


Fig 8.13. Raman Spectrum of NORG-18h (c) & NORG-24h (d)

Materials	D band position (cm ⁻¹)	G band position (cm ⁻¹)	I _D /I _G ratio
NORG-6h	1340	1571	1.14
NORG-12h	1347	1586	1.11
NORG-18h	1354	1581	1.08
NORG-24h	1349	1577	1.05

Table 8.6. D and G band peak positions and intensity ratio of different samples

From the above table, an interesting trend has been observed through out all the samples. The D band has been shifted and have maximum shift value of 1354 cm⁻¹ in NORG-18h sample and again slightly shifted in opposite in NORG-24h. On the other hand, G band has been shifted from NORG-6h and have maximum shift of 1581 cm⁻¹ in NORG-12h and again slightly shifted on the other side in NORG-24h. This phenomenon has attracted a huge interest and intensive work needs to be done in future. Though the intensity ratio (**I_D/I_G**) has followed a certain trend where it has been decreased from NORG-6h (1.14) to NORG-24h (1.04). This certain change in intensity ratio suggests increasing defect states in the samples. Thus, the Raman spectroscopy of NORG samples confirms successful reduction of GO to NrGO having good defect states.

References:

1. J. Hou, Y. Shao, M. W. Ellis, R.B. Moore, B. Yi, Graphene-based electrochemical energy conversion and storage: fuel cells, supercapacitors and lithium ion batteries, *Phys. Chem. Chem. Phys.* (13) (2011) 15384-15402.
2. Z. Peng, H. Yang, Synthesis and oxygen reduction electrocatalytic property of Pt-on-Pd bimetallic hetero nanostructures, *J. Am. Chem. Soc.* (131)(2009) 7542–7543.
3. J. D. Zhang, M. R. Vukmirovic, Y. Xu, M. Mavrikakis, R.R. Adzic, Controlling the catalytic activity of platinum-monolayer electrocatalysts for oxygen reduction with different substrates, *Angew. Chem., Int. Ed.* (44)(2005) 2170–2173.
4. G. Wu, K. L. More, C.M. Johnston, P. Zelenay, Polymer wrapping technique: an effective route to prepare Pt nanoflower/carbon nanotube hybrids and application in oxygen reduction *Science*, (332)(2011) 443–447. 4. W. Yang, Y. Wang, J. Li, X. Yang, Polymer wrapping technique: an effective route to prepare Pt nanoflower/carbon nanotube hybrids and application in oxygen reduction *Environ. Sci.*, (3)(2010) 144–149.
5. S. Wang, S. P. Jiang, X. Wang, Polyelectrolyte functionalized carbon nanotubes as a support for noble metal electrocatalysts and their activity for methanol oxidation *Energy Nanotechnology*, (19)(2008) 265601.
6. S. Wang, F. Yang, S. P. Jiang, S. Chen, X. Wang, Tuning the electrocatalytic activity of Pt nanoparticles on carbon nanotubes via surface functionalization, *Electrochem. Commun.* (12) (122010) 1646–1649.
7. S. Y. Wang, X. Wang, S.P. Jiang, PtRu nanoparticles supported on 1-aminopyrene functionalized multiwalled carbon nanotubes and their electrocatalytic activity for methanol oxidation, *Langmuir* (24)(2008) 10505–10512. 19
8. S. Y. Wang, N. Kristian, S. P. Jiang, X. Wang, Controlled synthesis of dendritic Au@ Pt core–shell nanomaterials for use as an effective fuel cell electrocatalyst, *Nanotechnology*, (20)(2009) 25605.
9. S. Wang, S.P. Jiang, T.J. White, X. Wang, Synthesis of Pt and Pd nanosheets on multiwalled carbon nanotubes as potential electrocatalysts of low temperature fuel cells, *Electrochim. Acta.* (55)(2010) 7652–7658.

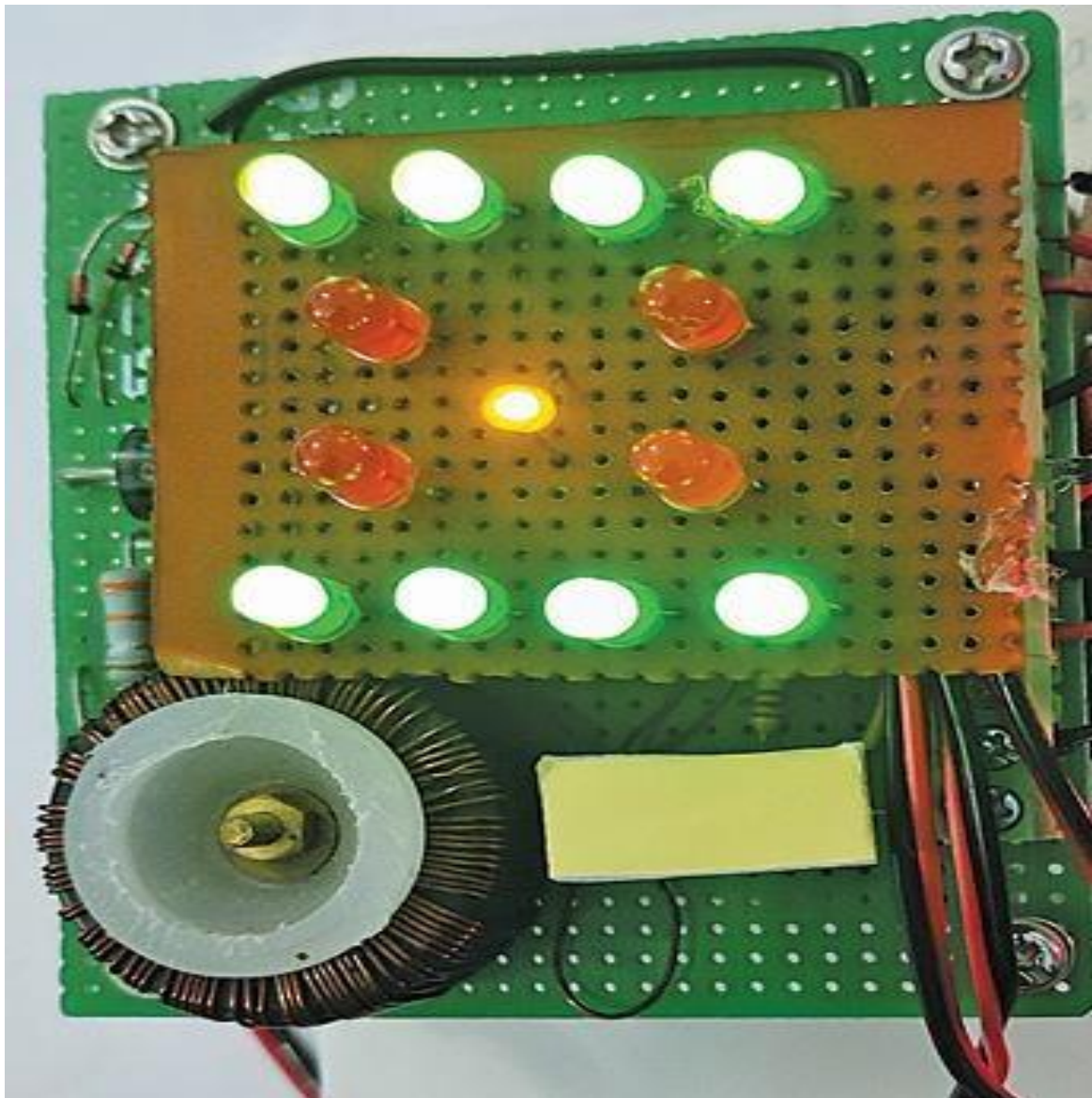
10. C. Goswami, K. K. Hazarika, P. Bharali, Transition metal oxide nanocatalysts for oxygen reduction reaction, *Materials Science for Energy Technologies*, 2018.
11. L. Li, J. He, Y. Wang, X. Lv, X. Gu, P. Dai, D. Liu, X. Zhao, Metal–organic frameworks: a promising platform for constructing non-noble electrocatalysts for the oxygen-reduction reaction *J. Mater. Chem. A* (7)(2019) 1964–1988.
12. S. J. Rowley Neale, J. M. Fearn, D. A. Brownson, G. C. Smith, X. Ji, C. E. Banks, molybdenum disulphide (2D-MoS₂) modified electrodes explored towards the oxygen reduction reaction, *Nanoscale* (8)(2016) 14767–14777.
13. C. Hu, Y. Zhou, R. Ma, Q. Liu, J. Wang, Reactive template synthesis of nitrogen-doped graphene-like carbon nanosheets derived from hydroxypropyl methylcellulose and dicyandiamide as efficient oxygen reduction electrocatalysts, *J. Power Sources* (345)(2017) 120–130.
14. W. Wei, Y. Tao, W. Lv, F. Y. Su, L. Ke, J. Li, D. W. Wang, B. Li, F. Kang, Q. H. Yang, Unusual high oxygen reduction performance in all-carbon electrocatalysts, *Sci, Rep* (4)(2014) 6289.
15. T. Chen, L. Dai, Carbon nanomaterials for high-performance supercapacitors, *Mater. Today* (16) (2013), 272–280.
16. A. K. Geim, K. S. Novoselov, The rise of graphene, *Nat. Mater.* (6) (2007) 183–191.
17. K. S. Novoselov, A. K. Geim, S. V. Morozov, D. Jiang, Y. Zhang, S. V. Dubonos, I. V. Grigorieva, A. A. Firsov, Electric field effect in atomically thin carbon films, *Science* (306)(2004) 666–669.
18. K. S. Kim, Y. Zhao, H. Jang, S. Y. Lee, J. M. Kim, K. S. Kim, J. H. Ahn, P. Kim, J. Y. Choi, B. H. Hong, Large-scale pattern growth of graphene films for stretchable transparent electrodes, *Nature* (457)(2009) 706–710.
19. K. V. Emtsev, A. Bostwick, K. Horn, J. Jobst, G. L. Kellogg, L. Ley, J. L. McChesney, T. Ohta, S. A. Reshanov, J. Röhrl, E. Rotenberg, Towards wafer-size graphene layers by atmospheric pressure graphitization of silicon carbide, *Nat. Mater.* (8) (2009) 203.
20. C. Berger, Z. Song, X. Li, X. Wu, N. Brown, C. Naud, D. Mayou, T. Li, J. Hass, A. N. Marchenkov, E. H. Conrad, Electronic confinement and coherence in patterned epitaxial graphene, *Science* 312 (2006) 1191–1196.

21. W. S. Hummers Jr, R. E. Offeman, Preparation of graphitic oxide, *J. Am. Chem. Soc.* (80) (1958) 1339.
22. S. Stankovich, D. A. Dikin, R. D. Piner, K. A. Kohlhaas, A. Kleinhammes, Y. Jia, Y. Wu, S. T. Nguyen, R. S. Ruoff, Synthesis of graphene-based nanosheets via chemical reduction of exfoliated graphite oxide, *Carbon* (45) (2007) 1558-1565.
23. S. Mao, K. Yu, S. Cui, Z. Bo, G. Lu, J. Chen, A new reducing agent to prepare singlelayer, high-quality reduced graphene oxide for device applications, *Nanoscale* (3) (2011) 2849–2853.
24. Z. Lei, L. Lu, X. S. Zhao, The electrocapacitive properties of graphene oxide reduced by urea, *Energy Environ. Sci.* (5) (2012) 6391–6399.
25. M. Jiang, J. L. Zhang, F. Qiao, R. Y. Zhang, L. B. Xing, J. Zhou, H. Cui, S. Zhuo, Selfassembled reduced graphene hydrogels by facile chemical reduction using acetaldehyde oxime for electrode materials in supercapacitors, *RSC Adv.* (6) (2016) 48276-48282. 21
26. C. A. Amarnath, C. E. Hong, N. H. Kim, B. C. Ku, T. Kuila, J. H. Lee, Efficient synthesis of graphene sheets using pyrrole as a reducing agent, *Carbon* (49) (2011) 3497–3502.

Chapter-9

Device performance

(Supercapacitor)



• Electrochemical Study:

In order to study the electrochemical properties and application of nitrogen doped reduced graphene oxide (N-rGO) in energy storage devices, three electrode cyclic voltammetry has been done in detail.

➤ Details of 3-electrode setup:

A three electrode cell was used for all electrochemical measurements for all electrochemical measurements for the as prepared supercapacitor electrodes of N-rGO. In the setup, N-rGO coated on Ni foam acted as working electrode, Ag/AgCl electrode was chosen to be as the reference electrode and platinum wire acted as the counter electrode [2]. 1M KOH solution was taken as the electrolyte. All measurements were carried out in room temperature without presence of any external gas. Cyclic Voltammetry (CV) was performed at different scan rates varying from 5 to 75 mV/s. Galvanostatic charge/discharge measurements were conducted at various current density such varied from 0.2 to 0.4 A/g and from 2 to 10 A/g to evaluate the specific capacitance, power density and energy density. A potential window in the range of -0.2 to 0 V was used in CV measurements [7].

➤ CV Performance of rGO coated Ni electrode:

CV performance and electrochemical measurements of an electrode depends upon three aspects, such as area under CV curve from plot, mass loading onto the electrode and the type of electrolyte. In this work, base electrolyte (KOH) has been used to study the nature of CV measurements. The active area under CV curve (total current) for each scan rate has been calculated from their plots for each sample electrode. Here, two types of capacitance such as gravimetric capacitance and areal capacitance have been calculated [3]. The formulae for calculating these two types of capacitance are:

$$\text{Gravimetric capacitance: } \frac{\text{Area under CV curve } (\int I dv)}{\text{Scan rate} \times \text{Voltage range} \times \text{mass loaded}}$$

$$\text{Areal capacitance: } \frac{\text{Area under CV curve } (\int I dv)}{\text{Applied voltage} \times \text{Scan rate} \times \text{active area of electrode}}$$

- **NORG-6h electrode performance and different capacitance:**

For NORG-6h electrode, the CV has been performed at different scan rates such as 10 mV/s, 20 mV/s, 40 mV/s, 50 mV/s, 75 mV/s and 100 mV/s. The mass loaded into the electrode is 0.0005 g and area of the electrode is 0.36 cm^2 .

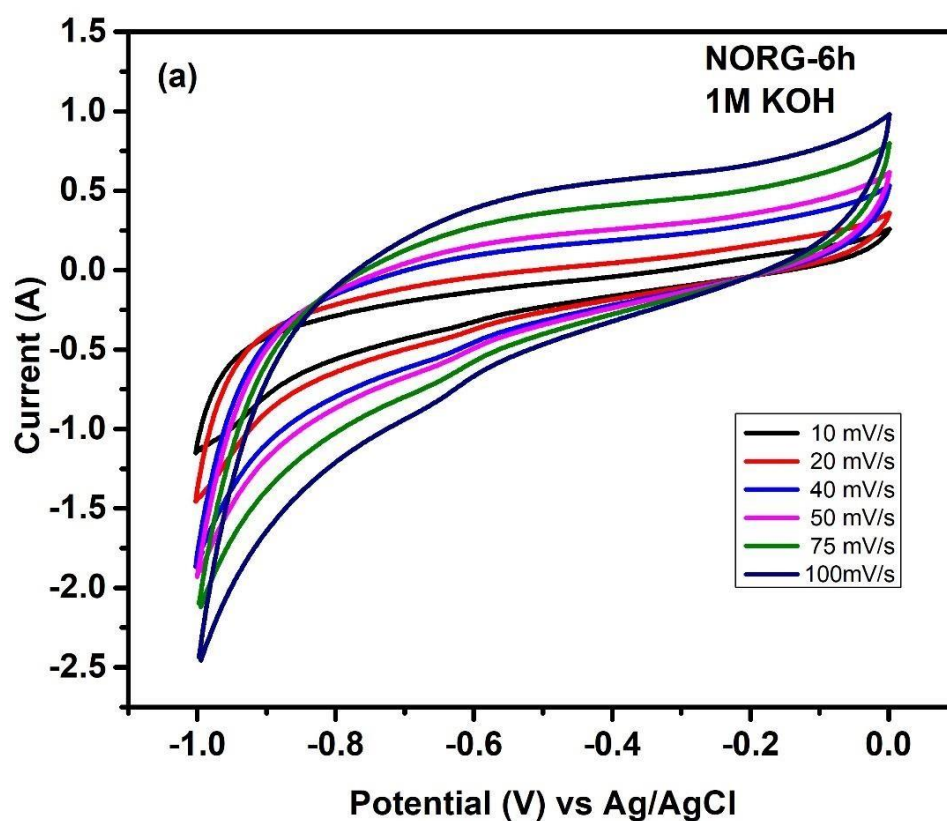


Fig 9.1. CV curve of NORG-6h at different scan rates.

Scan rate (mV/s)	10	20	40	50	75	100
Gravimetric Capacitance (F g^{-1})	13.28	10.55	8.12	7.53	6.53	6.10

Table 9.1. Details of scan rates and GC value of NORG-6h

Scan rate (mV/s)	10	20	40	50	75	100
Areal Capacitance (mF cm ⁻²)	18.45	14.65	11.28	10.46	9.07	8.47

Table 9.2. Details of scan rates and AC value of NORG-6h

From the above details of two types of capacitance, a certain trend has been observed. Both the capacitance has significantly decreased gradually with increase in scan rate.

➤ **NORG-12h electrode performance and different capacitance:**

For NORG-12h electrode, the CV has been performed at different scan rates such as 5 mV/s, 10 mV/s, 20 mV/s, 30 mV/s, 40 mV/s, 50 mV/s, 75 mV/s. The mass loaded into the electrode is 0.00005 g and area of the electrode is 0.36.

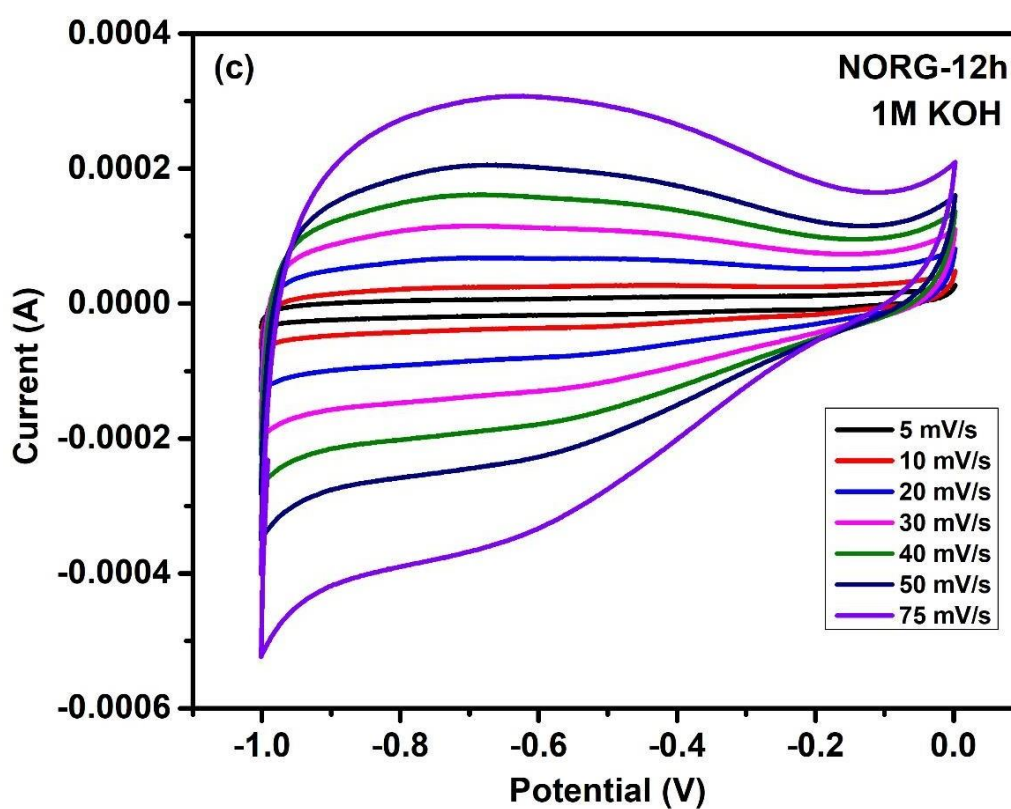


Fig 9.2. CV curve of NORG-12h at different scan rates.

Scan rate (mV/s)	Scan rate (mV/s)	5	10	20	30	40	50	75
Gravimetric Capacitance (F g ⁻¹)	Gravimetric Capacitance (F g ⁻¹)	132.66	130.65	129.57	127.69	120.11	105.26	89.23

Table 9.3. Details of scan rates and GC value of NORG-12h

Scan rate (mV/s)	5	10	20	30	40	50	75
Areal Capacitance (mF cm ⁻²)	20.17	19.86	18.02	17.73	16.68	14.62	12.39

Table 9.4. Details of scan rates and AC value of NORG-12h

These table is evident that with time the percentage of reduction has been increased and due to that, both of the capacitance has been increased simenteneously with respect to NORG-6h.

➤ **NORG-18h electrode performance and different capacitance:**

To determine gravimetric capacitance and areal capacitance of NORG-18h electrode CV has been carried out at 10 mV/s, 20 mV/s, 30 mV/s, 40 mV/s and 50 mV/s scan rates [11]. The mass

loaded into the electrode is 0.00005 g and area of the electrode is 0.36.

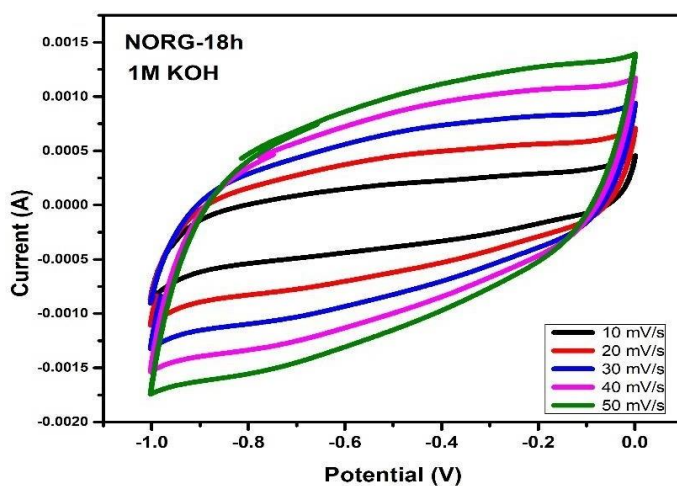


Fig 9.3. CV curve of NORG-18h at different scan rates.

Scan rate (mV/s)	10	20	30	40	50
Gravimetric Capacitance (F g ⁻¹)	988.40	899.09	833.54	760.86	706.58

Table 9.5. Details of scan rates and GC value of NORG-18h

Scan rate (mV/s)	10	20	30	40	50
Areal Capacitance (mF cm ⁻²)	137.27	124.87	115.77	105.67	98.13

Table 9.6. Details of scan rates and AC value of NORG-18h

Significantly the increase rate of capacitance has been jumped a lot from NORG-12h to NORG-18h. It has been increased almost 8 times.

➤ **NORG-24h electrode performance and different capacitance:**

As with increase in time of synthesis time, the capacitance has been increased till now for the other samples. Hence, to check proper capacitance of the sample NORG-24h, CV has been performed at large number of scan rates such as, 5 mV/s, 10 mV/s, 20 mV/s, 30 mV/s, 40 mV/s, 50 mV/s, 75 mV/s and 100 mV/s. 0.005 g mass had been loaded on the electrode and area of the electrode was 0.36 cm².

Scan rate (mV/s)	5	10	20	30	40	50	75	100
Gravimetric Capacitance (F g ⁻¹)	1113.4	1109.09	991.85	889.63	804.60	734.70	630.09	608.40

Table 9.7. Details of scan rates and GC value of NORG-24h

Scan rate (mV/s)	5	10	20	30	40	50	75	100
Areal Capacitance (mF cm ⁻²)	309.27	308.08	275.51	247.11	223.50	204.08	175.02	169.00

Table 9.8. Details of scan rates and AC value of NORG-24h

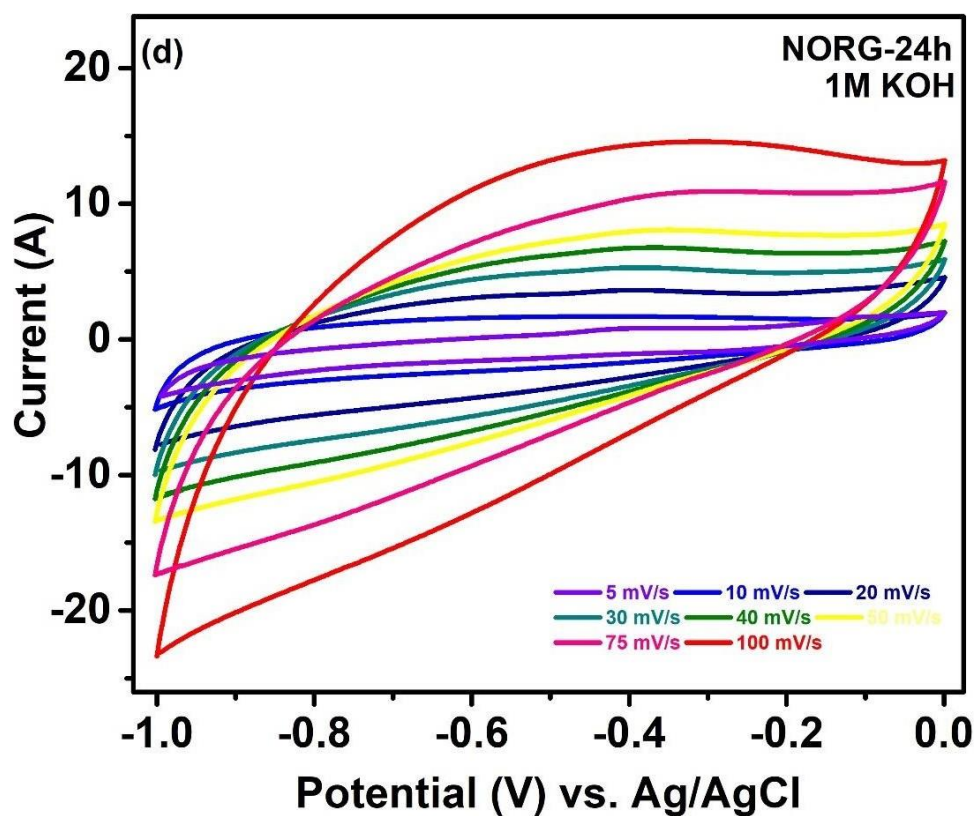


Fig 9.4. CV curves of NORG-24h at different scan rates.

From the above table and CV curve, the highest value of gravimetric capacitance and areal capacitance of NORG-24h are 1113.4 F g⁻¹ and 307.27 mF cm⁻² respectively. These are also the highest values of capacitance in this work. So, from the above discussion, it can be easily said that, with increase in synthesis time, the reduction has been increased which results better

performance in terms of CV and capacitance. From different characterizations of N-rGO it can be correlated that, porous nature of the material with time has been increased and highest in NORG-24h sample, thus increases the capacitance as well. Hence, in terms of capacitance of this material is hugely dependent upon the porosity of the samples.

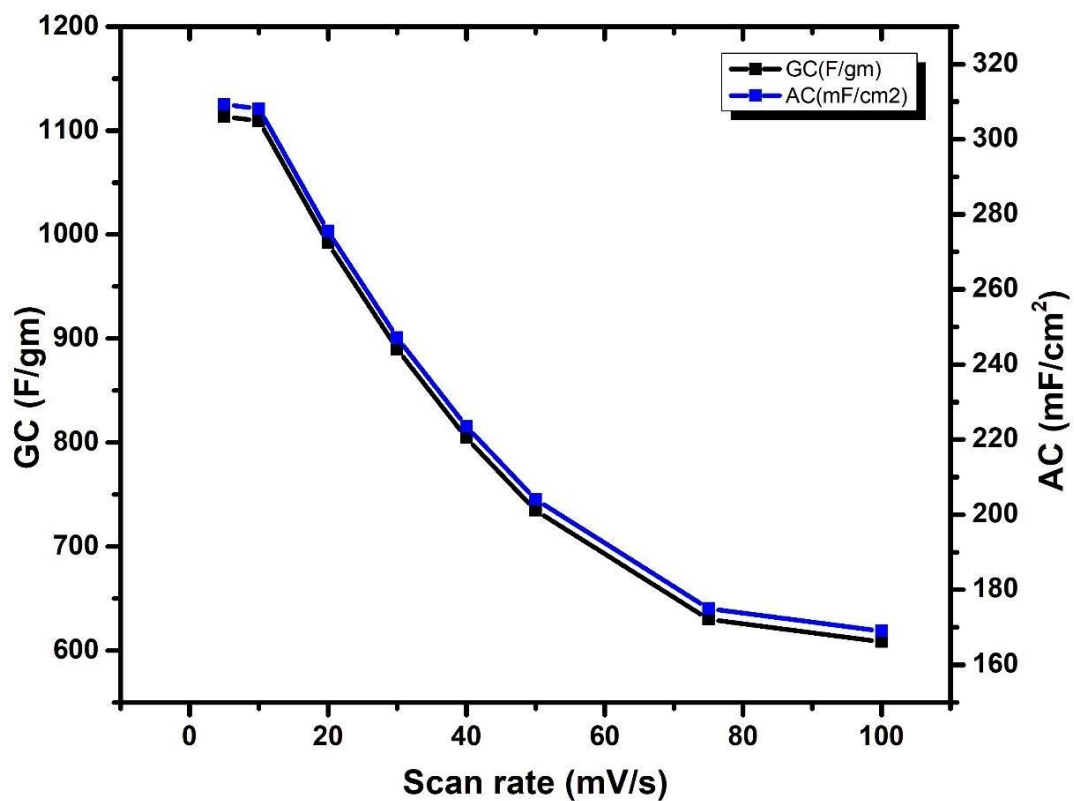


Fig.9.5. GC-AC comparison of NORG-24h electrode.

➤ Charge-Discharge Characteristics:

The charge-discharge characteristics for supercapacitor is very important to check their proper working efficiency. At the end of the day, a super capacitor would be judged over its fast charging time and slow discharging time. Apart from that, energy density and power density of the materials can be calculated experimentally from this curve as well. The charge-discharge measurements had been done at different current density for different samples here.

Energy density can be expressed as $E_s = \frac{1}{2} C_s (V)^2$

Power density can be expressed as $P_s = \frac{E}{t}$

Where, C_s is specific capacitance from charge-discharge plot, v is potential window, E_s is energy density, P_s is power density, V is applied potential window, and t is discharge time in that potential window.

➤ **Charge-Discharge curve of NORG-6h electrode:**

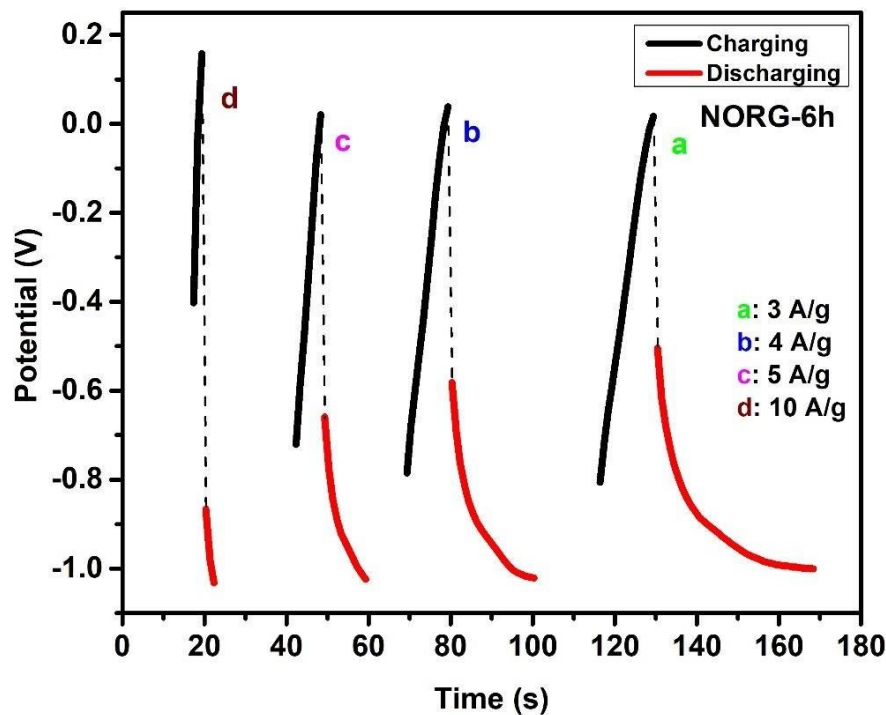


Fig9.6. C-D curve of NORG-6h

As we know, specific capacitance from C-D curve is $C_s = \frac{I \times t}{v}$, Where, I is current density, V is potential window and t is discharge time.

Current density (A g ⁻¹)	3	4	5	10
Specific Capacitance (F g ⁻¹)	97.37	70.90	48.33	22

Table 9.9. Details of Current densities and the respective specific capacitance of NORG-6h.

So, the highest energy density and power density of NORG-6h are $70.10 \text{ F g}^{-1} \text{ V}^2$ and $2880.11 \text{ F g}^{-1} \text{ V}^2 \text{ h}^{-1}$.

➤ **Charge-Discharge curve of NORG-24h electrode:**

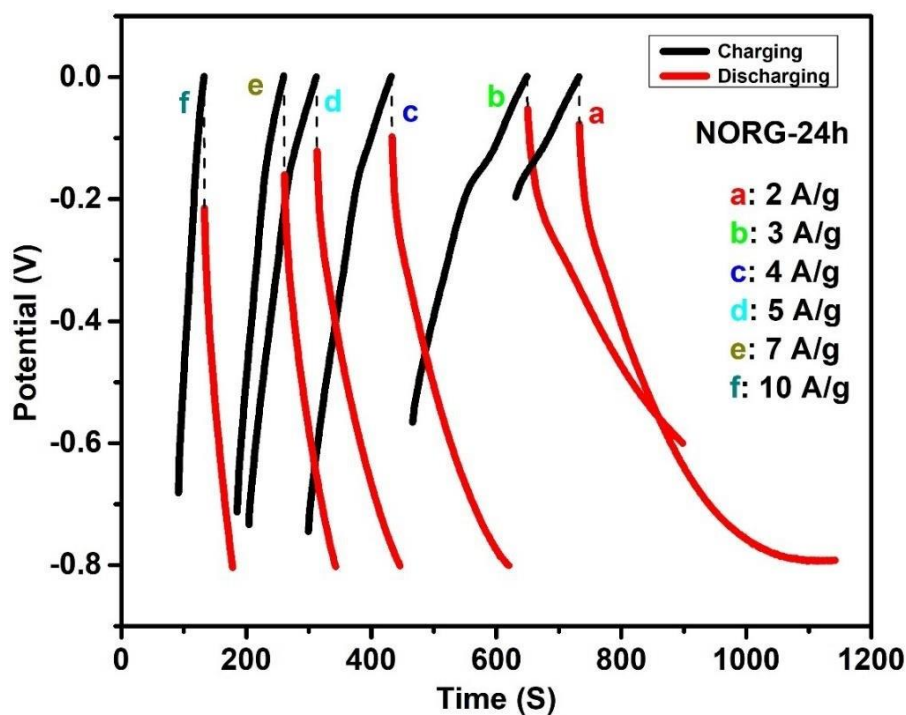


Fig9.6. C-D curve of NORG-24h

As we know, specific capacitance from C-D curve is $C_s = \frac{I \times t}{V}$, Where, I is current density, V is potential window and t is discharge time.

Current density (A g^{-1})	2	3	4	5	7	10
Specific Capacitance (F g^{-1})	1027.77	943.8	934.45	816.5	720.82	566.50

Table 9.10. Details of Current densities and the respective specific capacitance of NORG-24h.

So, the highest energy density and power density of NORG-6h are $328.88 \text{ F g}^{-1} \text{ V}^2$ and $6484.73 \text{ F g}^{-1} \text{ V}^2 \text{ h}^{-1}$. With compared to NORG-6h, the energy density and power density has been increased, which refers to the increasing supercapacitive nature with increasing reduction of GO to rGO.

➤ CV Performance of Coplanar interdigitated Supercapacitor:

As a device, the supercapacitor must possess a good power density and energy density with compared to electrolyte capacitors. Though, it's obvious that CV performance of single electrode would be better than a integrated device due to instrumental error, bulking of material (i.e., loosing some of nano particle properties) etc. In this part, the CV performance of the as prepared CI supercapacitor has been studied.

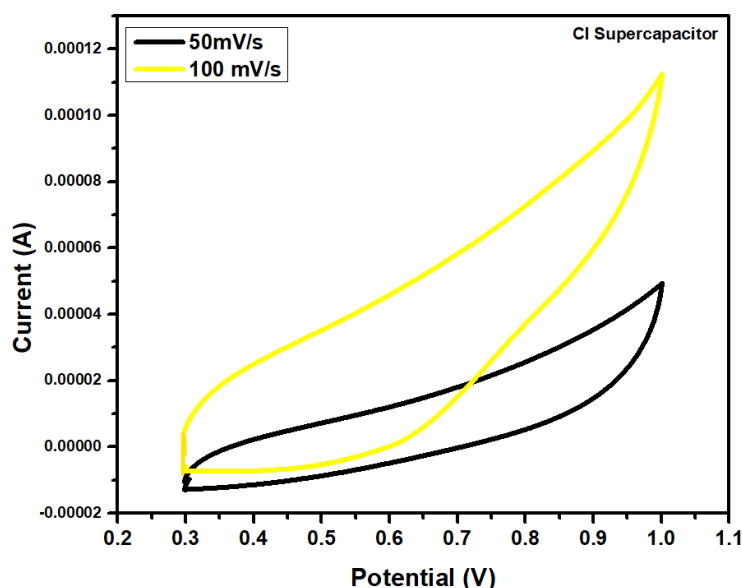


Fig9.7. CV curves for CI supercapacitor at different scan rates

Here from the graph we can see some distorted CV curves at 50 mV/s and 100 mV/s scan rates. It is because of instrumental error of fabrication and some impurities. The gravimetric capacitance and areal capacitance of the device has been found as 302.44 F g^{-1} and 79.84 mF cm^{-2} respectively at scan rate 50 mV/s. On the other hand, at 100 mV/s the GC value and AC values are 93.29 F g^{-1} and 57.23 mF cm^{-2} .

Chapter- 10

Device Performance

(Photodetector)



• I-V Analysis:

The n-n junction diode characteristics of the synthesized nanohybrids are examined in the dark condition, under room light, UV region and IR region at normal room temperature and are presented in Figure 10. This is a comparative study of the device under 4 different conditions. It is clearly observed that all the samples SiNWs, SiNWs/rGO demonstrate proper junction behavior of a practical diode. The diode follows the thermionic emission (TE) theory, according to which the current flowing through a forward biased junction can be determined by the following equation,

$$I = I_o \left[\exp\left(\frac{qV}{\eta kT}\right) - 1 \right]$$

where, I represent the net current flowing through the device, I_o represents the reverse saturation current, V stands for the applied voltage across the terminals of the diode, η represents the ideality factor, q denotes the absolute value of charge of an electron, k represents the Boltzmann's constant, and T gives the absolute temperature (K).

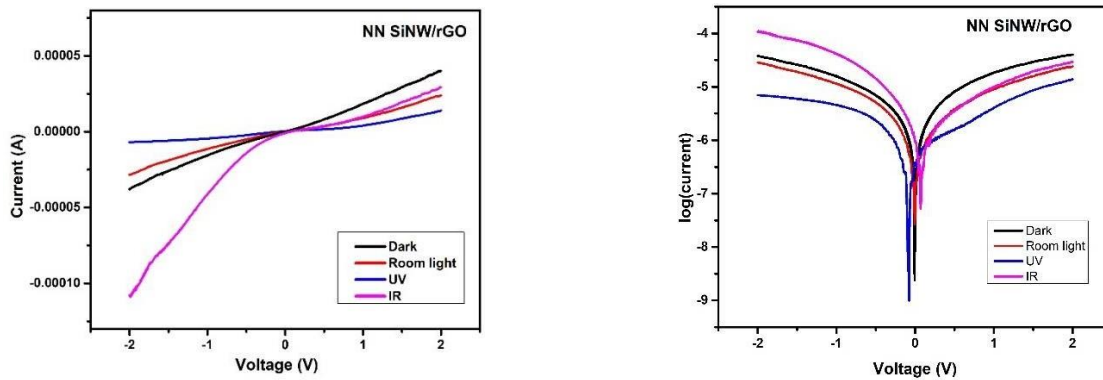


Fig.10.1. I-V characteristics of NN SiNW/rGO in dark condition, room light, UV and IR region.

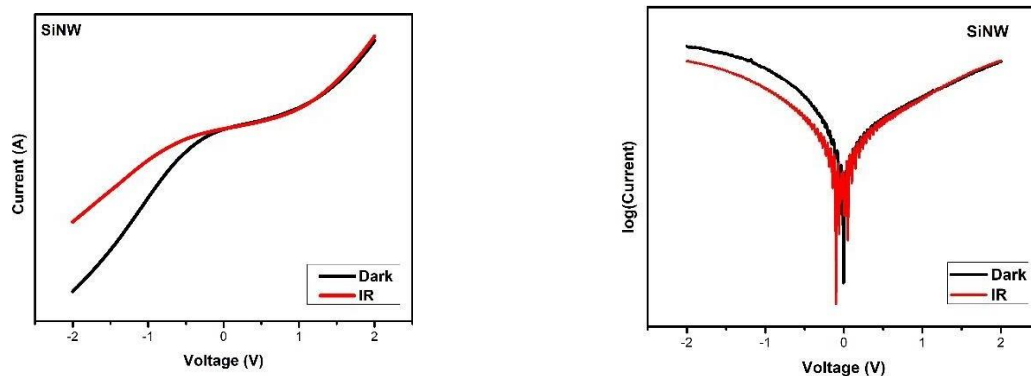


Fig.10.2. I-V characteristics of N type SiNW in dark condition and IR region.

From the above plots, it is observed that best I-V performance has been shown under IR region in reverse bias. In forward bias, the current is decreasing. However, with compared to bare SiNW the current is increased almost 100 times under IR region. Hence, the optoelectronics property of rGO can be confirmed. Even in dark condition as well, the device shows better performance than bare silicon nanowires.

- **ON-OFF Switching performance of NN SiNW/rGO device:**

ON-OFF switching is the most important characteristics of a photodetector for using as a sensor as well. Basically, this procedure involves the photo-response property of the as prepared device with respect to time. It is very important for a sensor to show a stable current-time ratio at a constant voltage under certain circumstances. The prepared device shows a great stable photo response or ON-OFF switching property under IV region with compared to bare silicon NW under same region of wavelength.

During this work, a mysterious phenomenon has been found of NN type SiNW/rGO photodetector that, it can produce current at 0 V as well. The reason behind this phenomenon is still under investigation, though it is suggested that due to some uncertain bond between Si and functional groups of rGO can cause extra charge carrier in this scenario. The on-off measurements have been carried out at 0V, -0.05V, -0.1V, -0.25V, -0.5V and -2.0V. From the

below figures, it can be observed that, the stability of the switching property has been increased towards 0V, though the amount of noise has been decreased towards -2.0V.

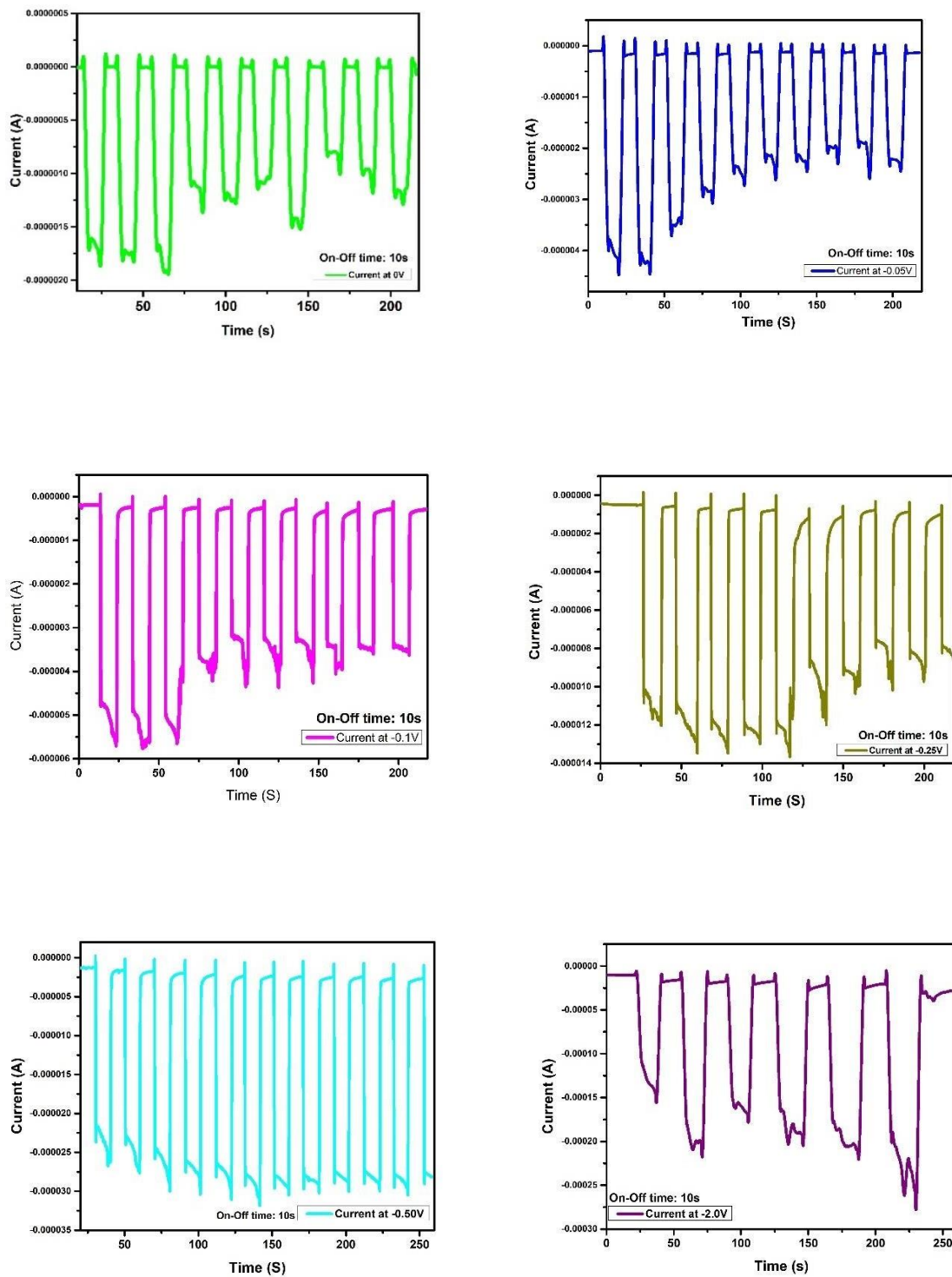


Fig10.3. ON-OFF switching plots of NN-SiNW/rGO device under IR region at 0V, -0.05V, -0.1V, -0.25V, -0.5V and -2.0V.

Reference:

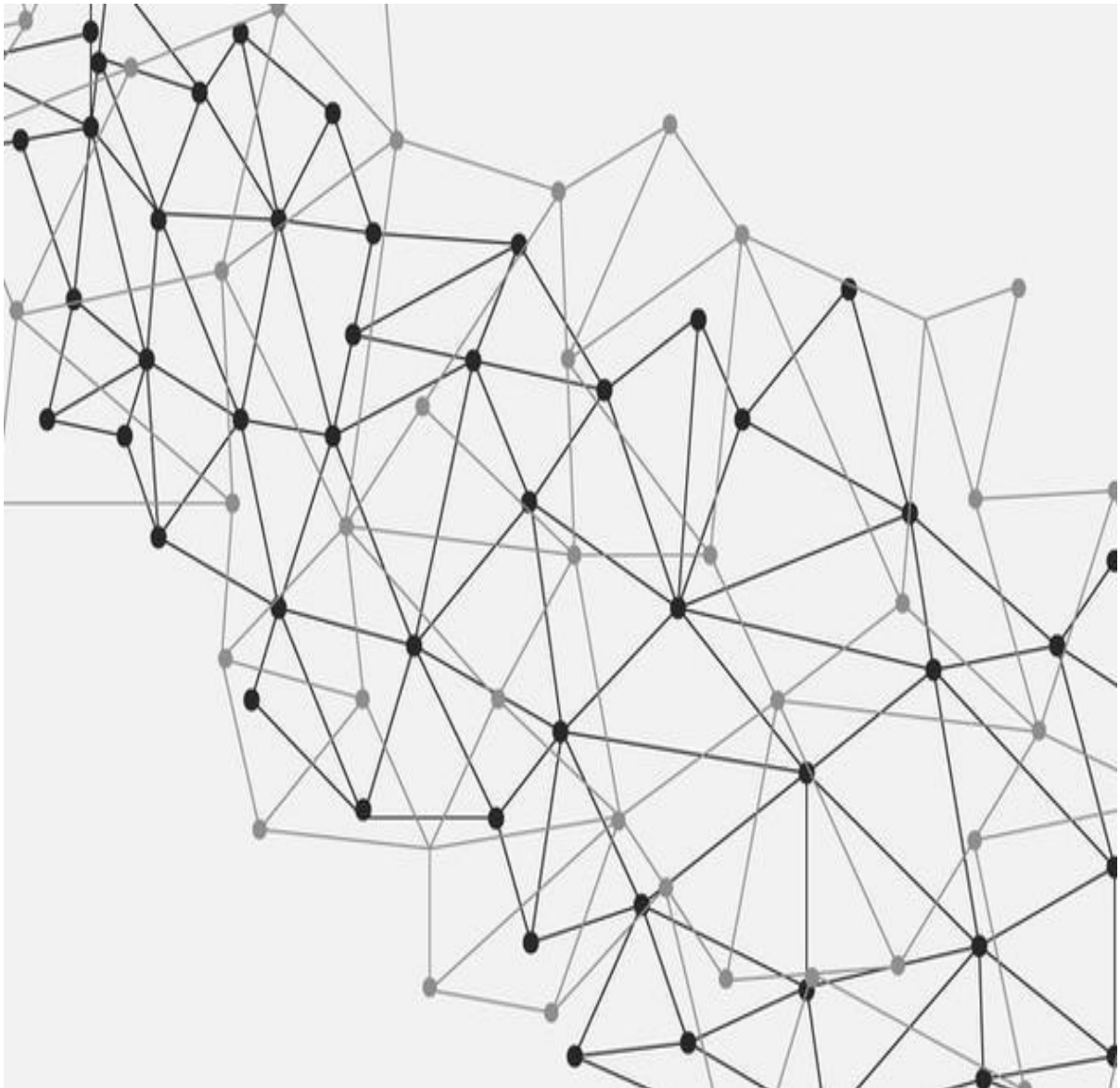
1. R. Roy, R. Thapa, S. Biswas, S. Saha, U. K. Ghorai, D. Sen, E. M. Kumar, G. S. Kumar, N. Mazumder, D. Roy, K. K. Chattopadhyay, Resonant energy transfer in a van der Waals stacked MoS₂-functionalized graphene quantum dot composite with ab initio validation, *Nanoscale* (10) (2018) 16822-16829.
2. J. Gao, F. Liu, Y. Liu, N. Ma, Z. Wang, X. Zhang, Environment-friendly method to produce graphene that employs vitamin C and amino acid, *Chem. Mater.* (22) (2010) 2213-2218.
3. J. Zhang, H. Yang, G. Shen, P. Cheng, J. Zhang, S. Guo, Reduction of graphene oxide via L-ascorbic acid, *Chem. Commun.* 46 (2010) 1112-1114.
4. G. Wang, J. Yang, J. Park, X. Gou, B. Wang, H. Liu, J. Yao, Facile synthesis and characterization of graphene nanosheets, *J. Phys. Chem. C* (112) (2008) 8192-8195.
5. J. Li, G. Xiao, C. Chen, R. Li, D. Yan, Superior dispersions of reduced graphene oxide synthesized by using gallic acid as a reductant and stabilizer, *J. Mater. Chem. A* (1) (2013) 1481-1487.
6. Z. J. Fan, W. Kai, J. Yan, T. Wei, L. J. Zhi, J. Feng, Y. M. Ren, L. P. Song, F. Wei, Facile synthesis of graphene nanosheets via Fe reduction of exfoliated graphite oxide, *ACS Nano* (5) (2010) 191-198.
33. R. S. Dey, S. Hajra, R. K. Sahu, C. R. Raj, M. K. Panigrahi, A rapid room temperature chemical route for the synthesis of graphene: metal-mediated reduction of graphene oxide, *Chem. Commun.* (48) (2012) 1787-1789.
7. N. A. Kumar, H. Nolan, N. McEvoy, E. Rezvani, R. L. Doyle, M. E. Lyons, G. S. Duesberg, Plasma-assisted simultaneous reduction and nitrogen doping of graphene oxide nanosheets, *J. Mater. Chem. A* (1) (2013) 4431-4435.
- 22
8. Y. Dong, Y. Deng, J. Zeng, H. Song, S. Liao, A high-performance composite ORR catalyst based on the synergy between binary transition metal nitride and nitrogen-doped reduced graphene oxide, *J. Mater. Chem. A* (5) (2017) 5829-5837.

9. D. Du, P. Li, J. Ouyang, Nitrogen-doped reduced graphene oxide prepared by simultaneous thermal reduction and nitrogen doping of graphene oxide in air and its application as an electrocatalyst, *ACS Appl. Mater. Interfaces* (7) (2015) 26952-26958.
10. S. Wang, D. Yu, L. Dai, D. W. Chang, J. B. Baek, Polyelectrolyte-functionalized graphene as metal-free electrocatalysts for oxygen reduction, *ACS nano* (5) (2011) 6202-6209.
11. L. Lai, J. R. Potts, D. Zhan, L. Wang, C. K. Poh, C. Tang, H. Gong, Z. Shen, J. Lin, R. S. Ruoff, Exploration of the active center structure of nitrogen-doped graphene-based catalysts for oxygen reduction reaction, *Energy Environ. Sci.*(5) (2012) 7936-7942.
12. D. Luo, G. Zhang, J. Liu, X. Sun, Evaluation criteria for reduced graphene oxide, *J. Phys. Chem. C* (115) (2011) 11327.
13. Y. Xu, H. Bai, G. Lu, C. Li, G. Shi, Flexible graphene films via the filtration of watersoluble noncovalent functionalized graphene sheets, *J. Am. Chem. Soc.*(130) (2008) 5856- 5857.
14. L. J. Cote, F. Kim, J. Huang, Langmuir–Blodgett assembly of graphite oxide single layers, *J. Am. Chem. Soc.*(131) (2009) 1043–1049.

Chapter-11

Conclusion & Future

Scope



• Conclusion:

In conclusion, porous nitrogen doped reduced graphene oxide (N-rGO) was synthesized using hydrothermal method. Before that, graphene oxide (GO) was prepared through modified Hummer's method. Confirmation of the crystallinity and phase has been carried out using XRD tool. Morphological analysis has been done through FESEM and HRTEM images which confirms the flake like structure and porous nature of reduced graphene oxide (rGO). From the spectrometric analysis, XPS has confirmed the amount of nitrogen doping and reduction of other functional groups of rGO. On the other hand, Raman spectroscopy evaluates the vibrational frequency of the material and validate the reduction process. From UV-vis, comparison of band gaps between silicon nanowire and rGO has been drawn which eventually helps to find the best sample to fabricate photodetector. From the cyclic voltammetric analysis, it can be confirmed that NORG-24h has the best gravimetric capacitance as well as areal capacitance of 1113.4 F g^{-1} and $309.27 \text{ mF cm}^{-2}$ respectively at 5 mV/s . To have industrial applicational perspective, coplanar interdigitated supercapacitor device has been fabricated which has gravimetric and areal capacitance of 302.44 F g^{-1} and 79.84 mF cm^{-2} respectively at a scan rate of 50 mV/s . As a photodetector material, N-rGO has been emerged as a promising aspect from this work. It has shown stable ON-OFF switching property in reverse bias under IR region. Maximum stability and less noise is attained at lower reverse bias such as -0.05 V and -0.25 V . This material exhibits current even at 0 V which is still under investigation. To draw a conclusion line to this work, it can be prominently and significantly told that, Nitrogen doped reduced graphene oxide is a very good nanomaterial which can be used in supercapacitor applications to attain promising energy density, power density and long cycles as well as it can be used as photodetector in IR region which implies as IR sensors also.

• Future Scope:

Nitrogen doped reduced graphene oxide (rGO) is a hub of green energy. It contains only carbon and other oxygen functional groups which are not harmful for environment. Due to this reasons, industrial supercapacitor preparation would be the foremost step in future. However, other 2D transitional materials such as MoS_2 , MoSe_3 will be used to make nanocomposite with rGO to attain much higher capacitance. On the other hand, the SiNW/rGO (NN type) device needs to be fabricated as an IR and temperature sensor. It will be done in clean room with proper

electronis setup. Once the final sensor will be fabricated, it is the main future focus to intregate the supercapacitor into the system to have a good sensor of huge sensing property and rapid charging facility.